

1. AGENCY USE ONLY (Leave blank)

2. REPORT DATE

May 95

3. REPORT TYPE AND DATES COVERED

4. TITLE AND SUBTITLE

2. TITLE AND SUBTITLE
Semiclassical - Quantum Correspondence & the
Onset of Chaos

5. FUNDING NUMBERS

6. AUTHOR(S)

Greg A. Finney

7. PERFORMING ORGANIZATION NAME(S) AND ADDRESS(ES)

AFIT Students Attending:

B. PERFORMING ORGANIZATION
REPORT NUMBER
AFIT/CI/CIA

9. SPONSORING/MONITORING AGENCY NAME(S) AND ADDRESS(ES)

DEPARTMENT OF THE AIR FORCE
AFIT/CI
2950 P STREET, BDLG 125
WRIGHT-PATTERSON AFB OH 45433-7765

10. SPONSORING/MONITORING AGENCY REPORT NUMBER	
---	--

11. SUPPLEMENTARY NOTES

12a. DISTRIBUTION / AVAILABILITY STATEMENT

Approved for Public Release IAW AFR 190-1
Distribution Unlimited
BRIAN D. GAUTHIER, MSgt, USAF
Chief Administration

12b. DISTRIBUTION CODE

DTIC
25 DISTRIBUTION CODE
S ELECTED D
JUN 1 9 1995
F

13. ABSTRACT (Maximum 200 words)

19950615 063

14. SUBJECT TERMS

15. NUMBER OF PAGES

130

16. PRICE CODE

17. SECURITY CLASSIFICATION OF REPORT

18. SECURITY CLASSIFICATION
OF THIS PAGE

19. SECURITY CLASSIFICATION
OF ABSTRACT

20. LIMITATION OF ABSTRACT

SEMICLASSICAL-QUANTUM CORRESPONDENCE
AND
THE ONSET OF CHAOS

Abstract of dissertation submitted in partial fulfillment
of the requirements for the degree of
Doctor of Philosophy

By

GREG A. FINNEY, B.S., M.S.
United States Air Force Academy, 1985
University of New Mexico, 1988

May 1995
University of Arkansas

Accession For	
NTIS	CRA&I <input checked="checked" type="checkbox"/>
DTIC	TAB <input type="checkbox"/>
Unannounced <input type="checkbox"/>	
Justification	
By	
Distribution /	
Availability Codes	
Dist	Avail and/or Special
A-1	

This abstract is approved by:

Dissertation Director:

A handwritten signature in dark ink, appearing to read "Julio Gea-Banacloche", written over a horizontal line.

Julio Gea-Banacloche

This dissertation explores the connection between two models for a two-level atom interacting with a single mode electromagnetic field. The first is a semiclassical model in which the field is treated classically and the atom is treated quantum mechanically, while the second is a full quantum model in which both the atom and the field are treated quantum mechanically (sometimes known in quantum optics and other fields as the spin-boson model). A unique pair of states, which remain factorizable for long times and are termed quasiclassical states, are derived from the semiclassical model. The quasiclassical states are found to match the evolution of the quantum model well for fields with the average photon number sufficiently large. These quasiclassical states are also derived from the eigenvalues and eigenvectors of the full quantum mechanical model alone.

The semiclassical system has been shown to exhibit chaos. We identify the causes of the transition to chaotic behavior in the semiclassical system in the vicinity of the quasiclassical orbits and examine the quantum system for signatures of that transition. Several authors have claimed to have found such signatures, but by using the quasiclassical states we show these supposed signatures are not unambiguously related to the appearance of chaos in the semiclassical model. The quasiclassical states also establish a basis for comparing results for calculations which use the rotating-wave approximation (RWA) with results from those which do not.

Finally, we extend the work by considering the effects of up to three atoms interacting with the quantum field. The result is that the system behaves more classically than for a single atom and some possible signatures of chaos are identified but cannot be established unequivocally.

SEMICLASSICAL-QUANTUM CORRESPONDENCE
AND
THE ONSET OF CHAOS

A dissertation submitted in partial fulfillment
of the requirements for the degree of
Doctor of Philosophy

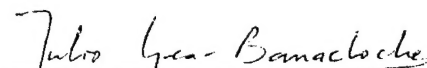
By

GREG A. FINNEY, B.S., M.S.
United States Air Force Academy, 1985
University of New Mexico, 1988

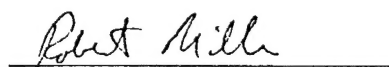
May 1995
University of Arkansas


This dissertation is approved for
recommendation to the
Graduate Council

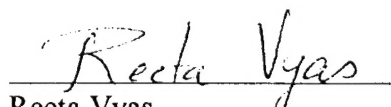
Dissertation Director:



Julio Gea-Banacloche

Dissertation Committee:


Robert Miller


William Oliver


Reeta Vyas


Min Xiao

ACKNOWLEDGMENTS

There are several individuals to whom I am deeply indebted for the completion of this work. My heartfelt gratitude goes to my advisor and friend, Julio Gea-Banacloche. Without his support, encouragement, and guidance, I could never have accomplished the task which was before me. He has taught me more about how to “do physics” than anyone with whom I have ever worked.

I am also grateful to the faculty of the University of Arkansas Department of Physics. In particular, I want to thank the department chairman, Rajendra Gupta, and the members of my committee. Their patience and flexibility enabled me to complete my degree in the three brief years the Air Force allotted.

However, one person has contributed more toward the successful completion of this work than any other: my wife. Martha, without your support I could never have even attempted this, much less succeeded. Thank you for the long days and the short nights, for the countless sacrifices, for your prayers, and for being the best mom our two boys could ever have. You are truly a wife of noble character.

Finally, I want to thank my Lord Jesus for leading me to this place and for surrounding me with people who helped me complete this task. I pray that I have been, and will continue to be, a success in His eyes.

Jeremiah 33:3 “Call to me, and I will answer you, and show you great and wonderful things you do not know.”

TABLE OF CONTENTS

	Page
ACKNOWLEDGMENTS	iii
LIST OF ILLUSTRATIONS.....	v
CHAPTER 1 REVIEW OF PREVIOUS WORK	1
1.1 Semiclassical Model—Prescribed field	2
1.2 Semiclassical Model—Dynamic field.....	3
1.3 Fully Quantum Mechanical System.....	5
1.4 Additional Work Reviewed.....	7
CHAPTER 2 ORIGINS OF CHAOS.....	10
2.1 Tests of Chaos.....	10
2.2 Development of Semiclassical Model	17
2.3 Chaos in the Semiclassical Model.....	28
CHAPTER 3 QUASICLASSICAL STATES AND THE QUANTUM MODEL.....	54
3.1 Development of Quasiclassical States.....	55
3.2 Evolution of the Field and of Arbitrary Initial States.....	65
3.3 Quasiclassical States From Eigenvectors of the Hamiltonian.....	77
CHAPTER 4 CHAOS AND THE QUANTUM MODEL	89
4.1 Impact of Semiclassical Chaos	89
4.2 Higher values of Angular Momentum.....	110
4.3 Conclusion.....	121
BIBLIOGRAPHY	123
APPENDIX A Matrices used in Perturbation Calculation.....	126
APPENDIX B A Note on Numerical Methods.....	129

LIST OF ILLUSTRATIONS

	Page
Figure 1. Shows the separation between initially close trajectories.....	11
Figure 2. Progression of estimated values of Lyapunov exponent.	13
Figure 3. Spectra for regular and chaotic trajectories.....	15
Figure 4. Poincaré section for two trajectories.	16
Figure 5. Variation of Floquet exponent $2\lambda_a$ with ε	22
Figure 6. A series of plots in the Bloch sphere.....	23
Figure 7. Variation of θ_+ with ε	26
Figure 8. FFT of $a_1(t)$ and $x(t)$	30
Figure 9. Variation in the location of the peak at $2\omega'-2\lambda_a$ with \bar{n}	32
Figure 10. Graph shows that two different harmonics shift with \bar{n} and merge.....	42
Figure 11. Euclidean distance between trajectories for different values of \bar{n}	43
Figure 12. Sequence of Lyapunov exponents starting near the plus branch.	44
Figure 13. Comparison of FFTs for chaotic and regular trajectories.....	45
Figure 14. Poincaré sections for trajectories starting from the plus branch.....	47
Figure 15. Euclidean separation and Lyapunov exponents near the minus branch.....	49
Figure 16. Comparison of FFTs starting near minus branch.....	52
Figure 17. Poincaré sections for minus branch.....	53
Figure 18. Comparison of Autler-Townes model with detuning and quantum model.....	57
Figure 19. Atomic state purity.....	59
Figure 20. Comparison of the semiclassical and fully quantized systems with the atom starting from the state $ a\rangle$	60
Figure 21. Q distribution showing splitting of field into two branches.....	61

Figure 22. Q distribution showing the plus branch field.	63
Figure 23. Interaction induced detuning along the plus branch vs. ε	64
Figure 24. Inversion as a function of time for a state which starts as a linear combination of $ \psi_+(0)\rangle$ and $ \psi_-(0)\rangle$ with equal weights.	69
Figure 25. Interference terms contributing to atomic inversion.	70
Figure 26. Q distribution for the plus and minus branches, showing when the revival occurs.....	71
Figure 27. Q distribution for an equally weighted linear combination of plus and minus branches	73
Figure 28. Comparison of population inversion vs. time for exact numerical results and small ε approximation.....	76
Figure 29. Photon number distribution for a displaced number state.	80
Figure 30. Eigenvalues from numerical diagonalization of Hamiltonian, zeroth order, and first order perturbation calculations.	81
Figure 31. Comparison of zeroth and first order eigenvectors.....	83
Figure 32. Floquet exponent from + state eigenvalues	87
Figure 33. Initial point for quasiclassical states calculated from eigenstates.....	88
Figure 34. Demonstration of collapse.....	92
Figure 35. Reversible evolution in non-RWA with field in a displaced number state.....	95
Figure 36. Plus branch trajectories for semiclassically regular and chaotic behavior.	100
Figure 37. Comparison of purity vs. time for plus branch.	101
Figure 38. Comparisons of spectra along plus branch for $\bar{n}=100$ and $\bar{n}=81$	102
Figure 39. Comparison of uncertainty product vs. time for plus branch.....	103
Figure 40. Comparison of minus branch trajectories.	106
Figure 41. Comparison of purity vs. time.	107
Figure 42. Comparisons of spectra of z along the minus branch	108

Figure 43. Comparison of uncertainty product vs. time for minus branch.....	109
Figure 44. Bloch sphere evolution for the $j=3/2$ model with $\varepsilon=0.141$ and $\bar{n}=96$	115
Figure 45. Bloch sphere evolution for $j=3/2$ model with $\varepsilon=1.0$	116
Figure 46. Bloch sphere evolution looking along $+y$ axis.	117
Figure 47. Comparison of $x(t)$ along the plus branch for $j=1/2$ and $j=3/2$	118
Figure 48. Purity vs. time along the plus and minus branches with $j=3/2$	119
Figure 49. Uncertainty product along the plus and minus branches for the $j=3/2$ model.	120

CHAPTER 1

REVIEW OF PREVIOUS WORK

The spin-boson system consists of a two-level system coupled to a harmonic oscillator. This system has been studied extensively because it is a relatively simple, closed interaction of two quantum objects and has many different physical manifestations. In this work we shall consider a two-level atom interacting with a quantized, single mode electromagnetic field,^{1,2} interacting via the dipole approximation. The Hamiltonian for this system takes the form

$$H = \hbar\omega a^\dagger a + \frac{1}{2}\hbar\omega_0 \sigma_z + \hbar g \sigma_x (a + a^\dagger), \quad (1.1)$$

where ω is the field frequency, ω_0 is the energy spacing of the two atomic levels, g is the coupling constant, a and a^\dagger are the boson annihilation and creation operators, and σ_x and σ_z are the Pauli spin operators. The first term represents the energy in the field, the second term the energy of the atom, and the third term is the interaction energy. However, other relevant physical forms include a two-level system such as an atom, electron, or exciton in a solid coupled to a phonon mode (see for example, Refs. 3 and 4); an ion in a trap, where the internal excitation of the ion forms a two-level system and the motion of the ion's center of mass is described by the oscillator;^{5,6} or a double well system under the influence of a periodic driving force.⁷ There are more realizations of the spin-boson system, but these few provide a demonstration of the broad application of the problem.

The purpose of this work is to study the relationship between the semiclassical and fully quantum mechanical versions of the problem. The semiclassical version, in which the field (oscillator) is treated as a classical system, was found to exhibit chaos in 1976.⁸ Since then, the spin-boson system has been studied by numerous authors in

an attempt to discover the relationship between classical chaos and “quantum chaos.” In what follows, the remainder of Chapter 1 will review the relevant work done by others, Chapter 2 will examine the origins of chaos in the semiclassical model, and Chapter 3 will develop and examine the quantum system using a special basis: the quasiclassical states. Finally, Chapter 4 will use the quasiclassical states to examine the impact of semiclassical chaos on the fully quantized system.

1.1 Semiclassical Model—Prescribed field

Autler and Townes⁹ studied the semiclassical version of Eq. 1.1 with a prescribed field. Equation 1.1 becomes for this case

$$H_{AT} = \frac{1}{2} \hbar \omega_0 \sigma_z + 2 \hbar g \sqrt{\bar{n}} \sigma_x \cos \omega t \quad (1.2)$$

where \bar{n} is the average photon number. Because this is a Hamiltonian periodic in time, Floquet’s theorem can be employed to find two solutions of the form

$$\begin{aligned} |\psi_+(t)\rangle &= \left(\sum_{k=-\infty}^{\infty} A_{2k} e^{i2k\omega t} |a\rangle - \sum_{l=-\infty}^{\infty} B_{2l+1} e^{i(2l+1)\omega t} |b\rangle \right) e^{-i\lambda_+ t} \\ |\psi_-(t)\rangle &= - \left(\sum_{l=-\infty}^{\infty} B_{2l+1} e^{-i(2l+1)\omega t} |a\rangle + \sum_{k=-\infty}^{\infty} A_{2k} e^{-i2k\omega t} |b\rangle \right) e^{i\lambda_- t} \end{aligned} \quad (1.3)$$

where $|a\rangle$ and $|b\rangle$ represent the upper and lower eigenstates of σ_z , respectively. This is the reverse of the notation used by Autler and Townes, but has been used to provide consistency with other publications¹⁰⁻¹². However, the A and B coefficients are unchanged (except for the trivial relabelling of indices k and l from including only even or odd integers to including all integers). The calculation of the Floquet characteristic exponent, λ_q , and the A and B coefficients is based upon infinite continued fractions and given in detail in Ref. 9. The two special solutions (1.3), which shall be referred to as the plus and minus branches henceforth, will appear repeatedly in this work. They are not identified specifically in Ref. 9 but come from Eq. 17 of Ref. 9 by setting

$A_0=0$ and $B_0=0$, respectively. (Incidentally, there is a sign error in that equation immediately preceding U_b .) For zero detuning, i.e. $\omega=\omega_0$, the characteristic exponent, λ_a , and the A and B coefficients all depend on a single parameter,

$$\varepsilon = \frac{g\sqrt{n}}{2\omega}. \quad (1.4)$$

This parameter is the ratio of the Rabi frequency, $2g\sqrt{n}$, to the nominal resonant frequency, ω_0 , and characterizes the importance of the counter-rotating (energy non-conserving) terms in the Hamiltonian (1.1).

Shirley also studied the semiclassical problem with a periodic prescribed field.¹³ He approached the problem using Floquet theory instead of continued fractions. He expanded the periodic Hamiltonian using complex exponentials and he solved the problem using matrix. The approach used here in Chap. 2 will be similar; however, we will go beyond his work by considering the effect of the atom reacting upon the field. Without the atomic reaction, chaos is impossible.

1.2 Semiclassical Model—Dynamic field

Although numerous authors have done work on this model, I will review in this section only those whose efforts have directly formed a basis for this work. The prescribed field model cannot admit chaotic solutions because it is exactly solvable, as seen above. Applying a different approximation, the rotating wave approximation (RWA), with a dynamic field cannot admit chaotic solutions either, because it, too, is exactly solvable. The RWA involves dropping the two terms from the interaction portion of the Hamiltonian (1.1) which do not conserve energy. Replacing σ_x with $(\sigma + \sigma^\dagger)$, where σ is the spin lowering operator, the excluded terms are σa and $\sigma^\dagger a^\dagger$. These terms correspond to changing the atom from the upper to the lower state while annihilating a photon and raising the atom from the lower to the upper state while

creating a photon, respectively. Neglect of these terms generally leads to only very small quantitative differences. However, Tavis and Cummings¹⁴ pointed out that for sufficiently strong fields the RWA breaks down.

The authors of Ref. 8, Belobrov, Zaslavskii, and Tartakovskii (BZT), were the first to identify chaos in the semiclassical version of Eq. 1.1. Expressed in terminology used here, they found, at resonance, the entire phase space was chaotic for $\varepsilon^2 \geq \bar{n}/32$, or $g \geq 0.35$. They found the extent of the chaotic region was narrow for small values of g and increased with increasing g . The chaotic region was identified by examining the time evolution of the trajectories as well as the Euclidean separation between initially close trajectories. They attributed the chaos to the perturbing effects of the terms excluded in the RWA. Later, a similar result was published by Milonni, Ackerhalt, and Galbraith (MAG) on a slightly different model using Lyapunov exponents and Fourier analysis to identify chaos.¹⁵ However, they focused on a different initial condition and a different part of the parameter space than we have. They considered an initially weak field with a large number of interacting atoms. For weak coupling (small g) these conditions give accurate results with the RWA. In order to obtain the strong fields needed to cause breakdown of the RWA given the initially weak fields, they required a large initial population inversion. The system then had enough energy to generate fields strong enough to cause breakdown of the RWA and chaos.

Fox and Eidson¹⁶ compared the results of MAG and BZT and identified the source of the difference in the models. The MAG model used an effective polarization density for the interaction between the atom and the field, while the BZT model used an effective current density. Fox and Eidson also showed the effective current density arises naturally by assuming factorization of the atom and field in the fully quantum mechanical model. Next, they demonstrated by a change of variables that the BZT

model in the RWA is equivalent to a classical spherical pendulum. In addition, the initial conditions used in the previous studies imply the pendulum is in near-separatrix motion, while adding the non-RWA terms is approximately equivalent to providing a periodic perturbation. Thus, the BZT model contains a periodically perturbed, near-separatrix pendulum, a universally accepted chaotic system.¹⁷ Moreover, the numerical results showed remarkable similarity between the pendulum motion and the MAG results, despite the differences in those systems.

Kujawski and Munz¹⁸ published a study of the frequencies which appear in the BZT model. Like the other authors, they considered initial conditions with weak fields and near full inversion. However, they found the frequencies appearing in the spectra were combinations of harmonics of two frequencies which they identified. They noted the values of these frequencies depended upon the strength of the field in the cavity, but they did not specifically identify the dependence.

1.3 Fully Quantum Mechanical System

Ultimately, most of the interest in the semiclassical model has been correlating the chaos observed with the evolution of the fully quantized system. There has been a great flurry of activity in the study of "quantum chaos," despite (or perhaps because of) the lack of a generally accepted definition. Because Schrodinger's Equation is a first-order, linear equation, chaos in the strictest sense is excluded. However, many classical systems have quantum mechanical counterparts, and it is the correspondence between these systems that forms the basis of "quantum chaos."

At least two distinct approaches have been used to investigate this area for the spin-boson system. First, some authors, such as Grigolini, *et al.*,¹⁹⁻²¹ have studied dynamic variables such as the purity or entropy and quantum uncertainty of the system. Their results were based on two general initial conditions, the atom in the

upper state and the field (i) in a coherent state with a small average photon number of $\bar{n}=5-10$ or (ii) in an eigenstate of the number operator with $n=10$. They found the evolution of the quantum system was marked by rapid growth in the field uncertainty and increase in the entropy of the atom-field system for parameters in which the semiclassical system was chaotic. They attributed these results to the effects of quantizing the dipole. Their work will be discussed in detail in Chap. 4.

Another approach that has been used extensively is examination of the eigenvalues of the full quantum Hamiltonian. For certain types of systems, such as a billiard ball in a stadium, the distribution of eigenvalues correlates closely with the chaotic or non-chaotic behavior of the classical version of the problem.²² For example, classically, a ball confined to a circular box (stadium) has a non-chaotic trajectory. However, if the stadium becomes an oval by inserting two short, straight parallel line segments, the trajectory becomes chaotic. Quantum mechanically, the circular stadium has many eigenvalues which are closely spaced together; the distribution of nearest neighbor spacings is described by a Poisson distribution. The eigenvalues of the oval stadium, meanwhile, exhibit level repulsion; the nearest neighbor spacing is described by a Wigner distribution.

Kuś examined the spectrum of the positive parity eigenvalues of Eq. 1.1.²³ He found the eigenvalues followed neither the Poisson nor Wigner distributions. Moreover, the eigenvalues followed a very regular spacing, even for large values of g where the system is non-integrable. Next, he measured the sensitivity of the spectrum to variation in parameters. Sensitivity to variation of parameters has been suggested as a characteristic feature of quantum chaos.²⁴ He found only the lowest lying eigenvalues displayed any sensitivity—most levels were quite insensitive to changes in ω_0 . He concluded from the spectrum the non-existence of “quantum chaos,” based upon the nature of the two-level system. His conclusion was supported by Graham

and Höhnerbach,²⁵ who reported, furthermore, that the nearest neighbor spacing distribution does, in general, approach the Wigner distribution for values of angular momentum larger than $j=1/2$ and, in particular, for $j=9/2$. The use of higher angular momentum corresponds to the interaction of the field with a larger number of atoms, so a more classical behavior is expected. Earlier, these authors presented an approximate expression for the eigenvalues developed by treating the ω_0 term in Eq. 1.1 as a perturbation.²⁶ The approximate expression gave accurate results in the region of most interest to this work, large n and g . However, when they applied their results to discuss the relationship between the behavior of the quantum system and the onset of semiclassical chaos,²⁷ their conclusions are questionable. The problem with their work will be covered in Chap. 4.

Although substantially more material could be included in a thorough review of this field, such a review is beyond the stated purpose here. Rather, I have included only the material which serves as the foundation of or for comparison with the main body of this work. However, the next section presents a number of additional articles which were examined during the course of this research.

1.4 Additional Work Reviewed

This section will very briefly describe some of the other work which has been done on relating the semiclassical and quantum versions of the spin-boson model. However, the papers included in this section did not make a vital contribution to the present effort. They are included here for the sake of completeness.

Cibils and coworkers published a series of articles comparing the results of the RWA and non-RWA models in the quantum and semiclassical domains.²⁸⁻³⁰ In Ref. 28 they obtain classical Hamiltonians which yield the semiclassical equations of motion for both the BZT⁸ and MAG¹⁵ systems. They then demonstrated that the MAG

system could not be obtained from a quantum Hamiltonian with spin $1/2$, but could for any larger value of spin. Next in Ref. 29 they use a phase approximation to study the system semiclassically and quantum mechanically. They use the phase approximation to show a back reaction of the atom upon the field is always present in a consistent treatment of the expansion in $1/\bar{n}$. Then they show that the eigenvalues using the phase approximation and the full quantum mechanical treatment yield similar level statistics (nearest neighbor distribution and Dyson-Mehta Δ_3 statistic) in the non-RWA, but not in the RWA. Reference 30 reports on their studies using the Husimi function. By scaling $\hbar=0.01$ they pushed the quantum system into the semiclassical domain. Then they examined the zeroes of the Husimi function, which form a type of Poincaré map (see Sec. 2.1 for an explanation of Poincaré sections) for the quantum system. They found the zeros of the Husimi function were regularly distributed when making the RWA and were somewhat scattered when not making the RWA.

Studies have also been done on the form of the ground state.^{31,32} The more recent of these references found good agreement between the exact ground state and a variational ground state based on the sum of two coherent states for intermediate values of the coupling, g , and the detuning, $\omega-\omega_0$. These authors continued their investigation by examining Poincaré sections of the field for both the semiclassical and quantum cases.³³ In the semiclassical case they used a procedure similar to the one used here in Chap. 2. For the quantum case, they turn to the Husimi density. They identify certain features shared by the semiclassical Poincaré section and quantum Husimi density. In particular, they find that islands of stability in the Poincaré section are visible in the Husimi density.

Steeb, *et al.* consider the closely related one-fermion, one-boson Hamiltonian.³⁴ When making the RWA approximation, they find the nearest neighbor spacings of the eigenvalues are distributed almost uniformly up to a maximum value. This contrasts

(as it should) with behavior associated with “quantum chaos,” for which the distribution of nearest neighbor spacings typically goes to zero. For the non-RWA the spacings form two groups, but still the distribution does not go to zero for zero spacing.

Following the work done in Refs. 23, 26, and 34, Schmutz considers an approximation to the eigenvalues of Eq. 1.1 in the high n limit.³⁵ Using the unitary transformation of Ref. 3, he reduces the spin-boson eigenvalue problem to a purely bosonic system. Then by extending the Hilbert space of the boson to negative n states he develops an asymptotic scaling law for the eigenvalues. This scaling law analytically estimates the eigenvalues for large n for any value of the detuning and coupling.

Finally, Refs. 7 and 36 discuss localization in a double well system with tunneling. They found it was possible to localize a particle in such a system by application of a periodic driving force. We were able to observe this localization in the semiclassical model in the chaotic portion of the parameter space.

CHAPTER 2

ORIGINS OF CHAOS

I have used several tools in exploring the presence of chaos in the semiclassical system. The first part of this chapter is devoted to describing the implementation of those tools. The second part of the chapter will apply those tools to explore the semiclassical model in the neighborhood of the periodic orbits obtained from Ref. 9.

2.1 Tests of Chaos

The widely accepted definition of chaos is a “sensitive dependence on initial conditions.” Sensitive dependence is demonstrated by an exponential separation of initially close phase-space trajectories. The most straightforward way to look for this behavior is by simply calculating the Euclidean distance between the points in phase space and plotting them on a semi-logarithmic scale. The Euclidean distance is defined to be

$$\Delta = \sqrt{\sum_{i=1}^n (x_i - x'_i)^2}, \quad (2.1)$$

where x and x' are the phase space coordinates and n is the dimension of the phase space. For example, consider the Hénon-Heiles system, which was thoroughly analyzed by Benettin, Galgani, and Strelcyn.³⁷ This is a classical chaotic system, containing mixed chaotic and non-chaotic regions for appropriately chosen parameters. Figure 1 shows the separation of two sets of trajectories, one from a regular region (a) and one from a chaotic region (b). The chaotic trajectories separate exponentially

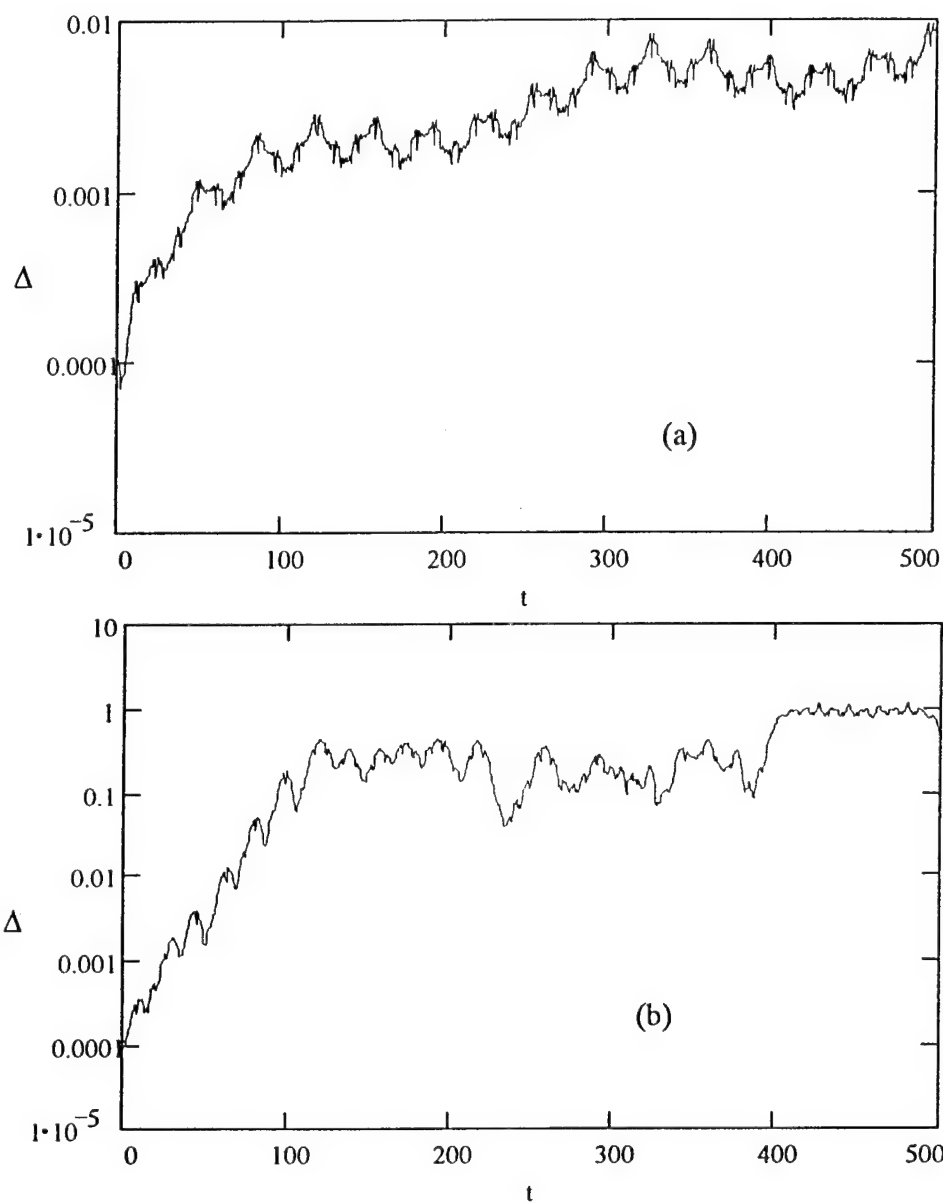
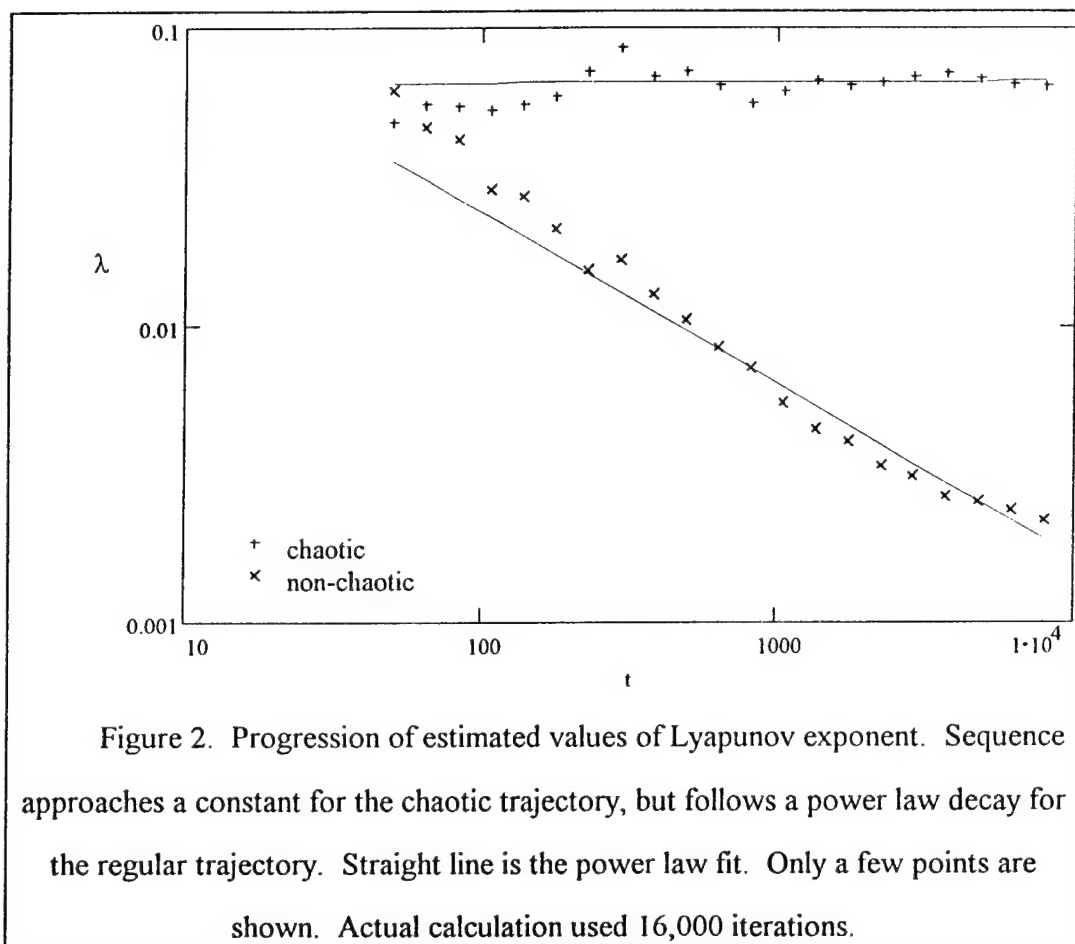


Figure 1. (a) Shows the separation between initially close trajectories from a non-chaotic portion of the phase space. (b) Shows the separation from a chaotic portion of the phase space. Note the difference in the vertical scale.

until the separation is approximately equal to unit distance, which is the approximate size of the available phase space for the chosen set of parameters (energy $E=0.13$, $q_2=-0.1$, $p_2=0$. Refer to Ref. 37 for definitions and details on the Hénon-Heiles system). Separation of the regular trajectories, however, is much slower and clearly not exponential. ($E=0.13$, $q_2=0.0$, $p_2=0.0$). In Sec. 2.2 we will see similar behavior in the semiclassical spin-boson model.

Closely related to the exponential growth in the Euclidean distance between trajectories is the concept of the Lyapunov exponent, λ , which gives the rate of exponential divergence of the trajectories in phase space. Because trajectories which are exponentially separating shortly reach the bounds of the available phase space for a space with finite volume, accurate calculation of λ requires periodically resetting the trajectories to a small separation. One can then accurately determine the average exponential separation rate. Reference 37 gives a detailed explanation of resetting the trajectories and how to determine λ . Most importantly, the process converges on λ only after many iterations. If $\lambda=0$, the sequence of calculated values decrease linearly on a log-log plot, i.e. they follow a power law decay. Again returning to the Hénon-Heiles system, Fig. 2 compares the calculation of λ in both ordered and chaotic regions, using the same initial conditions as Fig. 1.

Another common indication of chaos is in the frequency spectra of the dynamical variables in the problem. Regular spectra are characterized by a few, well separated peaks. Chaotic systems have noisy, broadband spectra. Using the same initial conditions, consider the fast-Fourier transform (FFT) of one coordinate, shown in Fig. 3. The first graph shows the spectrum for the regular trajectory. It shows a few fairly narrow peaks. On a linear plot, only half a dozen or so would be visible. The second, in marked contrast, shows a virtually continuous spectrum. Even on a linear graph, much of the structure would be visible. It is impossible to identify particular peaks as



in the first graph. In addition to examining the character of the spectrum, it can be useful to study the changes in the spectrum with changes in parameters or initial conditions. In the next section, we will see how numerical investigation of the spectrum led to an analytical result which helps to understand the origin of chaos in the vicinity of the periodic trajectories described by Eq. 1.3.

A third technique to identify chaos is by examining the Poincaré section. The Poincaré section is a stroboscopic plot of the trajectory. At periodic time intervals or when one of the coordinates takes on a particular value, two other coordinates (or other phase space variables) are plotted against each other. Reference 37 gives an example similar to Fig. 4a. In this figure, whenever the first coordinate, q_1 , is zero and the corresponding momentum, p_1 , is greater than zero a point is plotted on the graph. The same two trajectories were used in this figure, and form two distinct sets of points. One set is scattered throughout the phase space and results from the single chaotic trajectory, while the other set forms an oval and results from the non-chaotic trajectory.

The choice of variables for the Poincaré section is not unique; although some choices are less suitable than others. Figure 4b shows the result for a different section. Notice this section is not filled in as much, having less than 400 points for the same trajectory that produced over 1200 points in the oval in Fig. 4a. Thus, I used trial and error to develop the Poincaré sections used in Sec. 2.2, and found the results presented there to be satisfactory.

Three distinct tools for examining and quantifying chaos in a classical system have been presented: Euclidean separation of trajectories and the closely related Lyapunov exponent, spectral analysis, and Poincaré sections. Each of these will be used to first identify and then study chaos in the semiclassical version of the spin-boson model. First, though, I want to develop the equations of motion for the semiclassical model and relate these to the results of Autler and Townes.⁹

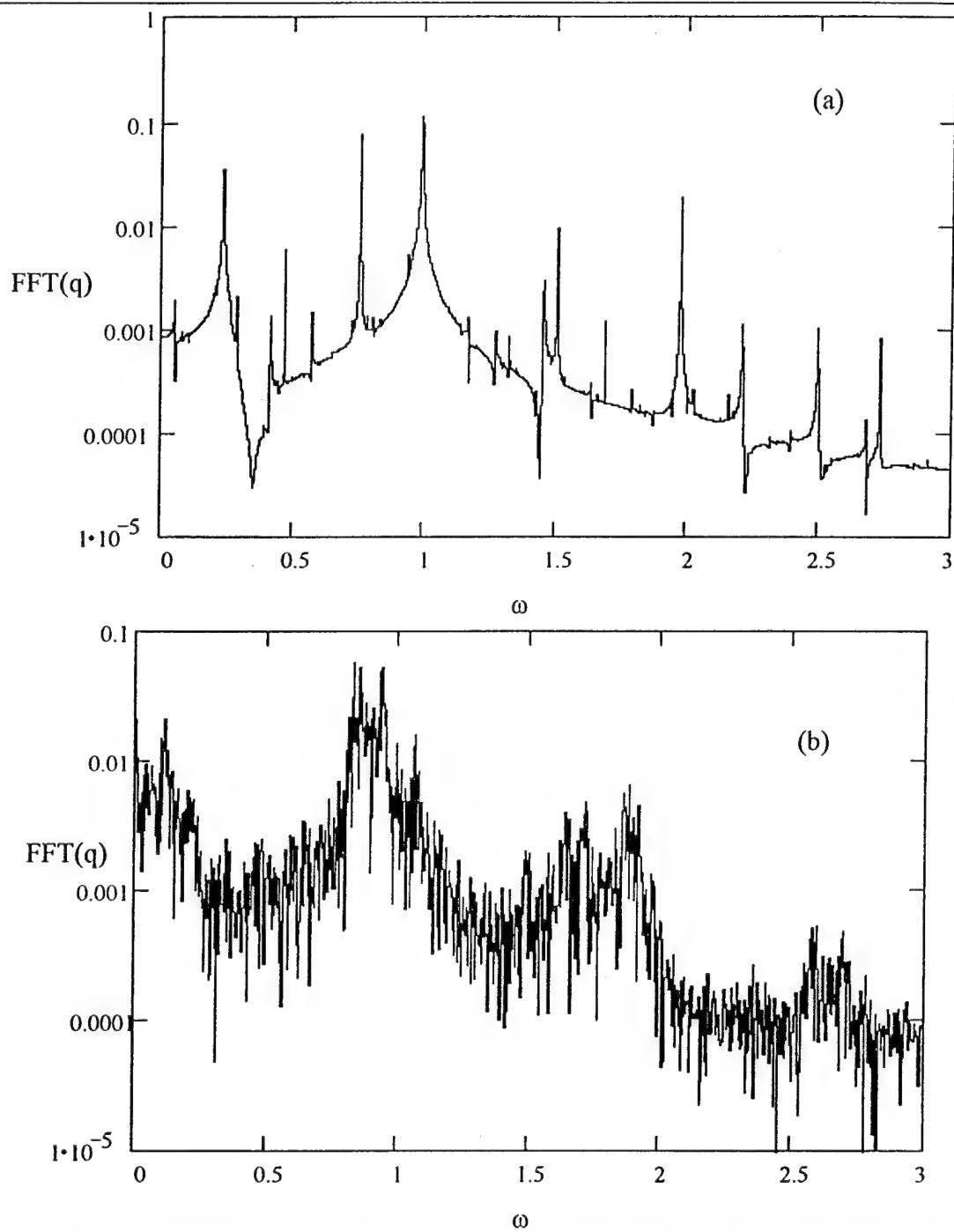
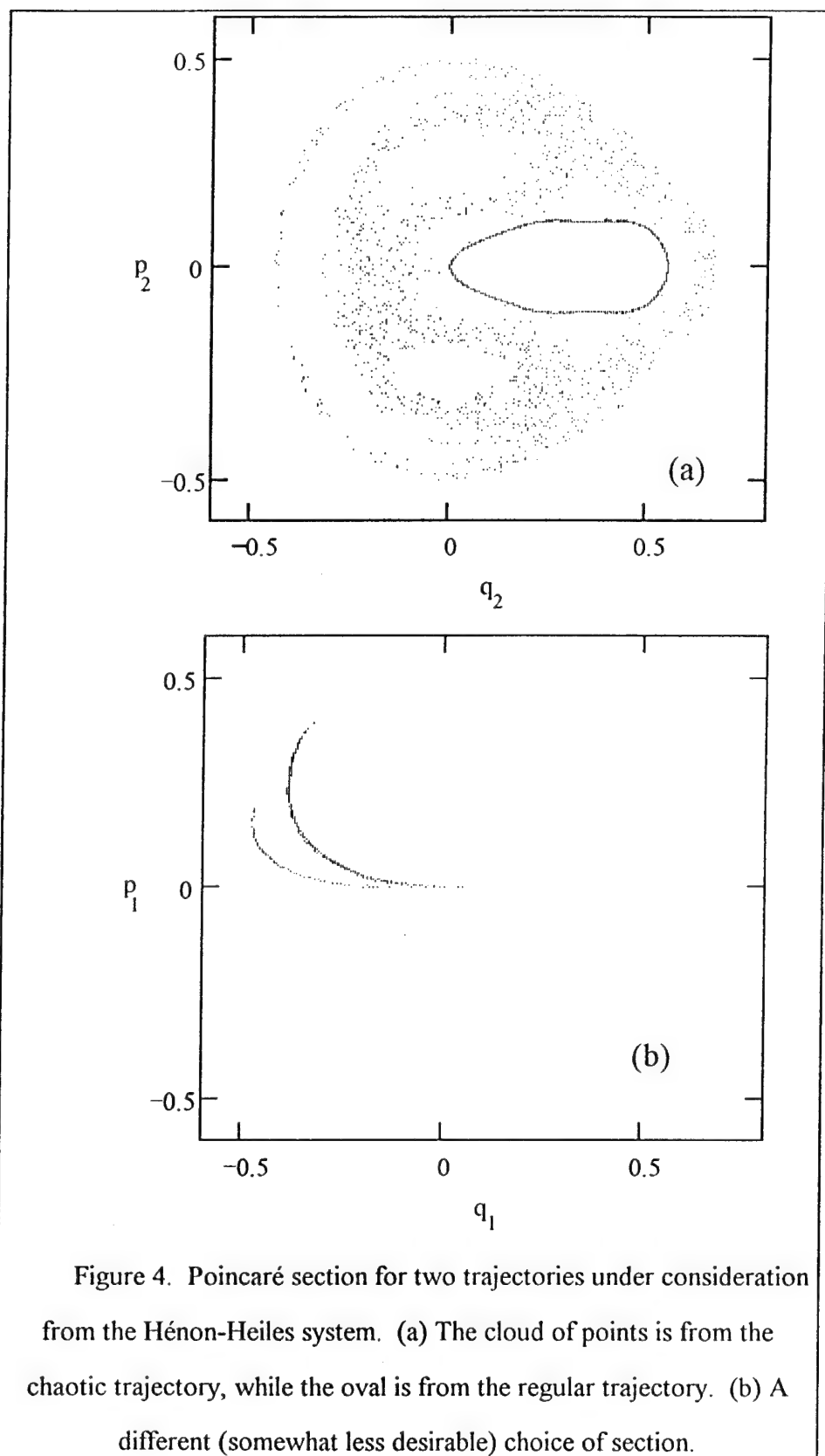


Figure 3. Spectra for (a) regular and (b) chaotic trajectories. Initial conditions are the same as for Fig. 1



2.2 Development of Semiclassical Model

Before endeavoring to develop the equations of motion, I will clarify the notation being used. The states of the two-level atom will be denoted as $|a\rangle$ and $|b\rangle$, $|a\rangle$ being the upper state. The energy difference between $|a\rangle$ and $|b\rangle$ is $\hbar\omega_0$. The electromagnetic field has frequency ω and except as otherwise noted will start in a coherent state $|\alpha\rangle$, with $\alpha = \sqrt{n}$.

As mentioned in Sec. 1.2, Ref. 16 provides a clear development of the semiclassical equations from the purely quantum system. Following the work done there, we begin with the Hamiltonian in Eq. 1.1 and Heisenberg's operator equations of motion:

$$\dot{\sigma}_x = \frac{1}{i\hbar} [\sigma_x, H] = -\omega_0 \sigma_y, \quad (2.2a)$$

$$\dot{\sigma}_y = \frac{1}{i\hbar} [\sigma_y, H] = \omega_0 \sigma_x - 2g\sigma_z(a + a^\dagger), \quad (2.2b)$$

$$\dot{\sigma}_z = \frac{1}{i\hbar} [\sigma_z, H] = 2g\sigma_y(a + a^\dagger), \quad (2.2c)$$

$$\dot{a} + \dot{a}^\dagger = \frac{1}{i\hbar} [a + a^\dagger, H] = -i\omega(a - a^\dagger), \quad (2.2d)$$

$$\dot{a} - \dot{a}^\dagger = \frac{1}{i\hbar} [a - a^\dagger, H] = -i\omega(a + a^\dagger) - 2ig\sigma_x. \quad (2.2e)$$

where the σ_i are the Pauli spin matrices. Now we make the definitions

$$x \equiv \langle \sigma_x \rangle, \quad (2.3a)$$

$$y \equiv \langle \sigma_y \rangle, \quad (2.3b)$$

$$z \equiv \langle \sigma_z \rangle, \quad (2.3c)$$

$$a_1 \equiv \frac{\langle a + a^\dagger \rangle}{2}, \quad (2.3d)$$

$$a_2 \equiv \frac{\langle a - a^\dagger \rangle}{2i}. \quad (2.3e)$$

In order to apply these definitions, we must take the expectation values of Eqs.

2.2. However, terms which contain products of operators must be treated approximately. In general, $\langle za \rangle \neq \langle z \rangle \langle a \rangle$. This relationship is an equality only for those states $|\Psi\rangle = |\psi\rangle \otimes |\Phi\rangle$, where $|\psi\rangle$ is the atomic part of the wavefunction and $|\Phi\rangle$ is the field part. Thus we are motivated to find “quasiclassical states,” quantum states which remain factorizable for a long period of time. Using work done with the RWA as a basis,¹⁰⁻¹² we expect to find such states for a single or a few atoms and average photon numbers in the realm of 10-100. Further details on finding the quasiclassical states will be deferred to Chapter 3; for now let us assume we can treat the states as factorizable and see what results can be obtained.

Upon replacing operators with their expectation values, Eqs. 2.2 become³⁸

$$\dot{x} = -\omega_0 y \quad (2.4a)$$

$$\dot{y} = \omega_0 x - 4gz a_1 \quad (2.4b)$$

$$\dot{z} = 4gy a_1 \quad (2.4c)$$

$$\dot{a}_1 = \omega a_2 \quad (2.4d)$$

$$\dot{a}_2 = -\omega a_1 - gx \quad (2.4e)$$

These five equations are the semiclassical equations of motion for the atom-field system. Scaling the system by $\omega_0 t \rightarrow t$, $\omega/\omega_0 \rightarrow \mu$, $4(g/\omega_0)a_1 \rightarrow a_1$, and $4(g/\omega_0)a_2 \rightarrow a_2$, and defining $\beta \equiv 4g^2 / (\omega\omega_0) = 16\varepsilon^2\mu / \bar{n}$, we obtain the system implemented for numerical computations:

$$\dot{x} = -y, \quad (2.5a)$$

$$\dot{y} = x - za_1, \quad (2.5b)$$

$$\dot{z} = ya_1, \quad (2.5c)$$

$$\dot{a}_1 = \mu a_2, \quad (2.5d)$$

$$\dot{a}_2 = -\mu a_1 - \frac{\beta}{\mu} x. \quad (2.5e)$$

This system is the same as used in Ref. 18, except for the sign of the field, which was chosen to match Refs. 10-12. Having derived this for the general case, in what follows we shall only consider the resonant case, $\mu=1$, unless otherwise noted. In these systems, the three components x , y , and z form the atomic Bloch vector,^{11,39} which has a constant unit length. In addition, energy is conserved, which has the form

$$\frac{\langle H \rangle}{\hbar \omega_0} = \frac{z}{2} + \mu(a_1^2 + a_2^2 + 1) + \frac{2g}{\omega_0} x a_1 \quad (2.6)$$

referring to (2.4) or

$$E = \beta(z + x a_1) + \frac{\mu^2}{2}(a_1^2 + a_2^2) \quad (2.7)$$

referring to (2.5).

It is straightforward to generalize this to interactions with larger numbers of atoms in order to obtain a more classical system. First, replace the σ_i with the corresponding angular momentum operators J_i in the Hamiltonian (1.1) and in Eq. 2.2. Let the angular momentum quantum number $j = N/2$, where N is the number of atoms interacting. Next, change the definition of x , y , and z to be the expectation of the corresponding angular momentum operation divided by j . Equations 2.4a-d are then unchanged and Eq. 2.4e is

$$\dot{a}_2 = -\omega a_1 - 4gxj. \quad (2.8)$$

By scaling $g \rightarrow g/\sqrt{2j}$, $a_1 \rightarrow a_1\sqrt{2j}$, and $a_2 \rightarrow a_2\sqrt{2j}$, Eqs. 2.4 are restored. Thus, in the semiclassical version of the problem, the equations are unchanged by suitable scaling in going to a larger number of atoms. Interestingly, since $\bar{n} = \langle a^\dagger a \rangle$, $\bar{n} \rightarrow \bar{n}2j$ and $\varepsilon (= g\sqrt{\bar{n}}/2\omega)$ remains unchanged. Quantum mechanically, of course, there

remains a tremendous difference. For clarity, I will defer further discussion of values of j larger than $1/2$ until Chap. 4.

In addition to being useful for numerical calculations, Eq. 2.5 is conceptually helpful. Noting that β scales like $1/\bar{n}$ for fixed ε , one can easily see how the reaction of the atom on the field is diminished with increasing \bar{n} . Furthermore, the scaling makes the magnitude of the field dependent only upon ε . In Eq. 2.4, $\alpha_1 = \sqrt{\bar{n}}$ at $t=0$. This becomes, in Eq. 2.5, $\alpha_1 = 8\varepsilon$. Increasing \bar{n} with ε fixed makes the system behave more like the system with the prescribed field, since the magnitude of the field does not change while the reaction decreases as $1/\bar{n}$. Therefore comparison to the work in Ref. 9 becomes particularly straightforward, since the system (2.5) reduces to that one for fixed ε and $\bar{n} \rightarrow \infty$. As mentioned earlier, we expect to require photon numbers somewhat greater than $\bar{n}=10$ in order to have states which remain factorizable and provide a reasonable comparison between the quantum and semiclassical models.

The evolution described by Eq. 1.3 is clearly non-chaotic. Each branch evolves quasiperiodically. How does this quasiperiodic behavior in the limit $\bar{n} \rightarrow \infty$ become chaotic as \bar{n} decreases? The simplest manner to compare the evolution of Eq. 1.3 with the numerical integration of Eq. 2.5 is to express the expectation values of σ_i when taken over the branches $|\psi_+\rangle$ and $|\psi_-\rangle$. In order to arrive at a general expression, consider a linear superposition of the plus and minus branches $|\psi\rangle = C_+|\psi_+\rangle + C_-|\psi_-\rangle$. Since this state should be normalized, it is convenient to write C_+ and C_- as $\cos(\gamma/2)$ and $\sin(\gamma/2)$, respectively. Then taking expectation values gives:

$$\begin{aligned}
 x = & \cos \gamma \sum_{n=0}^{\infty} \sum_{k=-\infty}^{\infty} 2(A_{2k}B_{2k+2n+1} + A_{2k}B_{2k-2n-1}) \cos((2n+1)\alpha t) \\
 & - \sin \gamma \sum_{n'=-\infty}^{\infty} \sum_{k=-\infty}^{\infty} (A_{2k}A_{2n'-2k} + B_{2k+1}B_{2n'-2k-1}) \cos(2n'\alpha t - 2\lambda_a t)
 \end{aligned} \tag{2.9a}$$

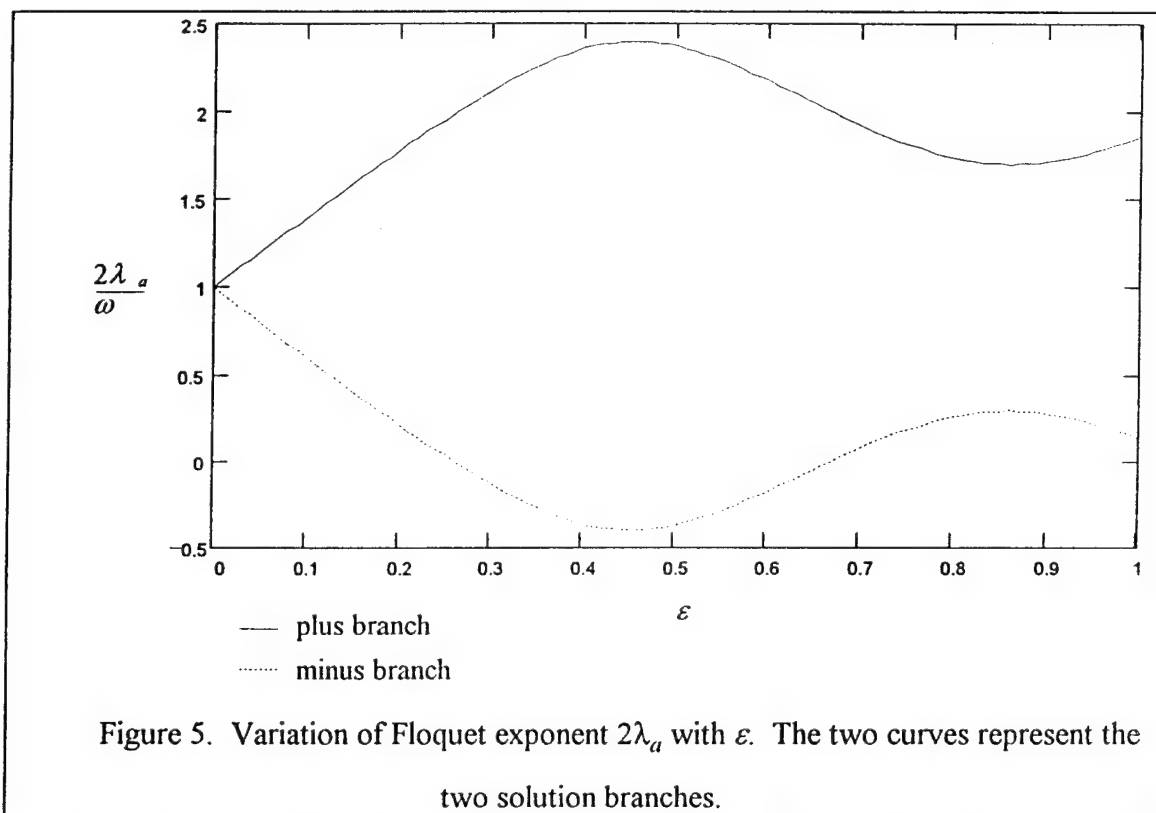
$$y = \cos \gamma \sum_{n=0}^{\infty} \sum_{k=-\infty}^{\infty} 2(A_{2k} B_{2k+2n+1} + A_{2k} B_{2k-2n-1})(2n+1)\omega \sin((2n+1)\omega t) \\ - \sin \gamma \sum_{n'=-\infty}^{\infty} \sum_{k=-\infty}^{\infty} (A_{2k} A_{2n'-2k} + B_{2k+1} B_{2n'-2k-1})(2n'\omega - 2\lambda_a) \sin(2n'\omega t - 2\lambda_a t) \quad (2.9b)$$

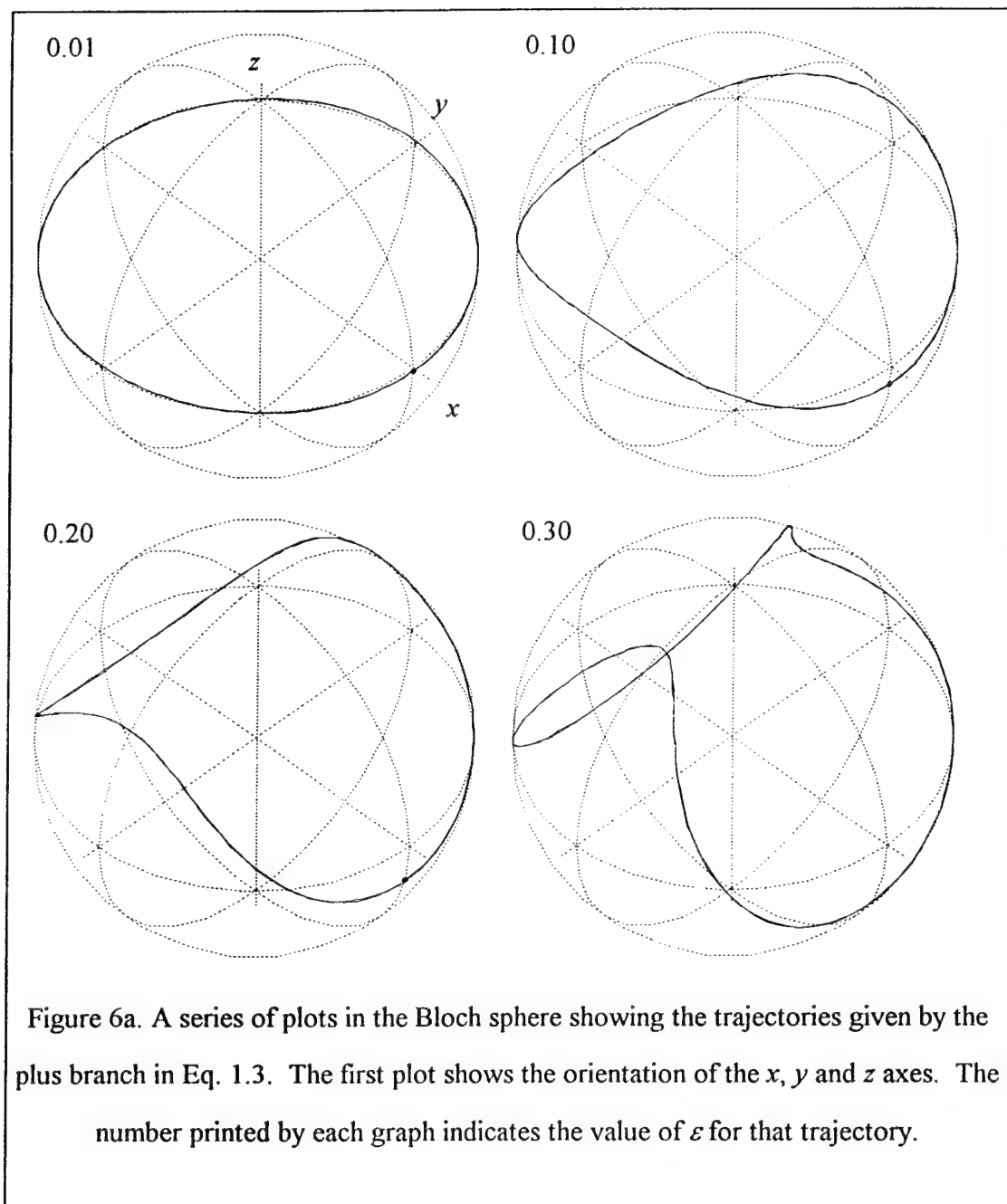
$$z = \cos \gamma \left(\sum_{k=-\infty}^{\infty} (A_{2k}^2 - B_{2k+1}^2) + 2 \sum_{n=1}^{\infty} \sum_{k=-\infty}^{\infty} (A_{2k} A_{2k+2n} - B_{2k+1} B_{2k+1+2n}) \cos 2n\omega t \right) \\ - \sin \gamma \sum_{n'=-\infty}^{\infty} \sum_{k=-\infty}^{\infty} 2 A_{2k} B_{2n'+1-2k} \cos((2n'+1)\omega t - 2\lambda_a t) \quad (2.9c)$$

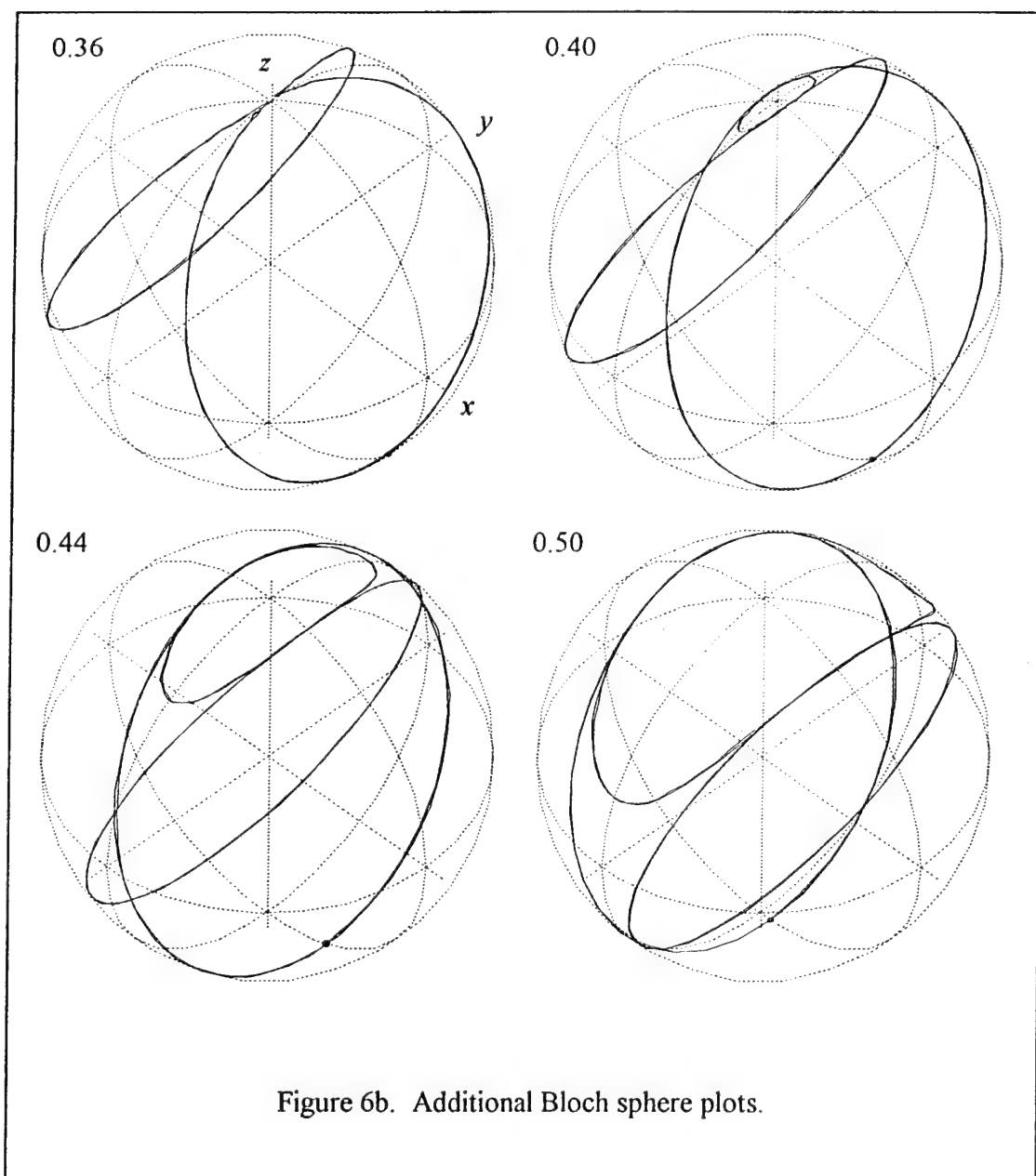
When $\gamma=0$ or π the trajectories are periodic, corresponding to the plus and minus, respectively branches. Since λ_a/ω is generally not a rational number, almost all other trajectories are quasiperiodic. Using the methods of Ref. 9, we can plot $2\lambda_a$ vs. ε , as in Fig. 5 below.

Autler and Townes mention the problems associated with multiple solutions for the characteristic exponent, and we emphasize it as well. Examining Eq. 1.3 one can readily observe that if λ_a is a Floquet exponent, $2n\omega + \lambda_a$ is also a Floquet exponent. This requires simply factoring out $e^{i2n\omega}$ from within the summation while relabelling the indices k and l . This process can be repeated, giving an infinite number of solutions, none of which are physically distinct. However, replacing λ_a with $-\lambda_a$ results in swapping the plus and minus branches. (This result does not come directly from Eq. 1.3 because the A 's and B 's depend on λ_a ; the existence of a second set of solutions is discussed in Ref. 9.) The new solution is now physically distinct. Alternatively, the two branches can be considered as representing two solutions with positive and negative Floquet exponents.

Before proceeding further, consider the appearance of these solutions in terms of the Bloch sphere. Figure 6 shows a sequence of plus branch trajectories for different







values of ε . The number printed by each sphere displays the value of ε for that trajectory. For small values of ε the trajectories remain in near-equatorial orbits—the atom experiences little inversion. However, increasing ε increases the inversion, so that for $\varepsilon=0.368$ the trajectory actually passes through the upper atomic state. For the choice of field phase given in Eq. 1.2, the initial point in all of these plots is in the x - z plane, with $x>0$, as shown by the small dot. For $\varepsilon > 0.515$, however, the initial point has $x < 0$, and for even larger ε it switches back again, but always with $z < 0$. The minus branch trajectories are obtained by reflection through the origin, but are otherwise identical.

The evolution of the full semiclassical system given by Eq. 2.5 yields very similar trajectories for sufficiently large \bar{n} , using for the initial condition the point given by Eq. 1.3 at $t=0$. It is convenient to define the starting point in terms of the spherical angles in the Bloch sphere. In that case, we can write

$$|\psi_+(0)\rangle = \cos\frac{\theta_+}{2}|a\rangle + \sin\frac{\theta_+}{2}|b\rangle \quad (2.10a)$$

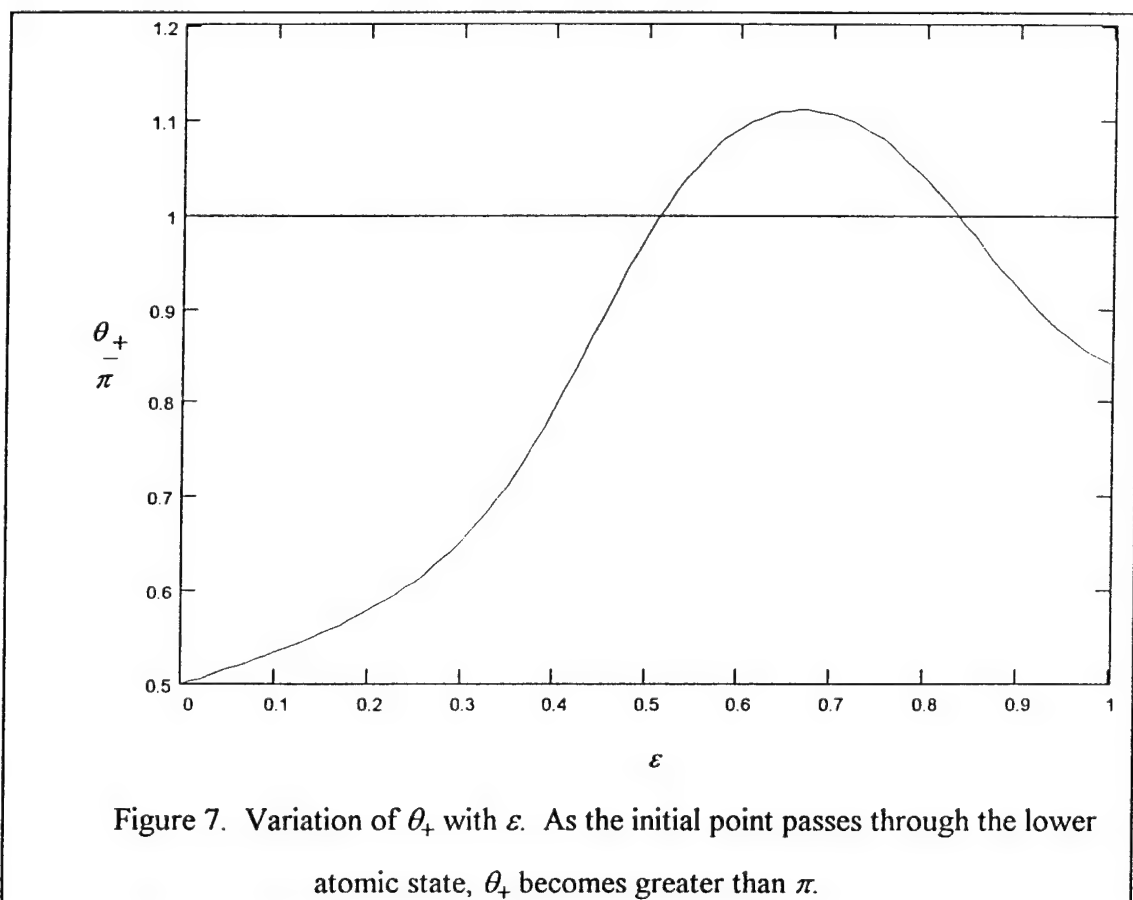
$$|\psi_-(0)\rangle = \sin\frac{\theta_+}{2}|a\rangle - \cos\frac{\theta_+}{2}|b\rangle \quad (2.10b)$$

where θ_+ is the polar angle (colatitude) measured from the positive z axis.

Comparison with Eq. 1.3 yields

$$\cos\frac{\theta_+}{2} = \sum_{k=-\infty}^{\infty} A_{2k}. \quad (2.11)$$

A plot of θ_+ versus ε is shown in Fig. 7. As the initial point passes through the lower atomic state, θ_+ becomes greater than π . The initial point passes through the lower atomic state twice, once at $\varepsilon = 0.515$ and again at $\varepsilon = 0.831$. The orthogonal state is located at the opposite end of the diameter, and so it passes through the upper atomic state at the same values.



Differences between Autler-Townes trajectories and the semiclassical evolution do exist, although they can be made arbitrarily small given sufficiently large \bar{n} . The first effect, noticeable even for small ε , is an interaction-induced detuning. Rather than oscillating at the frequency ω_0 , the trajectory oscillates at ω' , which is slightly different. By writing $x(t)$ as

$$x(t) = \sum_{n=0}^{\infty} x_n \cos(2n+1)\omega't \quad (2.12)$$

and the field as

$$a_1(t) = a_1(0) \cos \omega't \quad (2.13)$$

(with $a_1(0) = 8\varepsilon$) then inserting into Eq 2.5d,e the interaction induced detuning becomes

$$\omega' - \omega \approx \frac{gx_0}{2\sqrt{\bar{n}}} = \frac{\varepsilon x_0}{\bar{n}} \omega \quad (2.14)$$

by matching terms with the same time dependence. One can see clearly from this relationship that the detuning vanishes for large \bar{n} , as it should. Equation 2.14 also shows the detuning will be much smaller than ω since $\varepsilon \lesssim 1$ and $x_0 \leq 1$, while $\bar{n} > 10$. Of course, the precise value of x_0 depends on the detuning used to calculate it. To obtain even better agreement between the Autler-Townes and semiclassical models, this procedure can be iterated—finding x_0 assuming no detuning, then using the detuning given by that x_0 to calculate a new x_0 . Because the detuning is small, this process converges after no more than two iterations for $\varepsilon \lesssim 1$.

The detuning found in this manner gives excellent agreement with the detuning found by numerically integrating Eq. 2.5. The detuning of the numerical results can be found most easily by converting the field expectation values into a complex phasor $\alpha = a_1 + ia_2$. The phasor rotates approximately as $e^{-i\omega't}$. Multiplying α by $e^{i\omega t}$ cancels all but the detuning, which can then be determined by fitting the remaining phase drift to a straight line.

The detunings for the two branches are approximately equal in magnitude and opposite in sign. This is obvious from Eq. 2.9a, by setting $\gamma = \pi$ to obtain the minus branch. Clearly x_0 for the minus branch is opposite in sign and equal in magnitude to x_0 for the plus branch if we neglect the detuning in Eq. 2.9a. Furthermore, since the detuning is small, the effect it will have on x_0 when included will be small as well.

2.3 Chaos in the Semiclassical Model

We have seen the semiclassical model has periodic trajectories which are near the Autler-Townes solutions. In this section we will see these trajectories are stable for sufficiently large \bar{n} , but become unstable as \bar{n} decreases, resulting in chaos. For some values of ε , the plus branch requires a larger value of \bar{n} to remain stable than the minus branch requires. For other values of ε , the minus branch is the first to become unstable as \bar{n} decreases. The signature of the instability in the trajectory is found in the spectra: As \bar{n} changes, the location of the peaks shift from the values predicted by the Autler-Townes solutions, the peaks merge, and complex, chaotic spectra result. First we will examine the spectra resulting from numerically integrating Eq. 2.5. Then we will attempt to understand the numerical results analytically. By linearizing the system around the Autler-Townes solutions (2.9), we can develop an approximate expression for the frequency shifts and understand why one branch becomes unstable before the other.

Now consider trajectories which are near, but not precisely on the plus and minus branches. Figure 8 shows the FFT of the field for $\bar{n} = 1024$ and $\varepsilon = 1$ with $\gamma = .1\pi$. In addition to the prominent peak at $\omega = 1.00$ (recall time has been scaled by ω_0 in all numerical calculations), additional peaks at $\omega = 0.13, 1.87, 2.13$ and 3.00 are visible. These peaks approximately correspond to $2\omega - 2\lambda_a$, $2\lambda_a$, $4\omega - 2\lambda_a$, and 3ω , respectively. Of course, in the Autler-Townes model, the only frequency appearing is ω . The lower

part of the graph shows the equivalent result for x . Although the spectrum is much more complicated, most of the frequencies correspond to those just listed, and which do appear in the Autler-Townes model (see Eq. 2.9). However, the pair of peaks bracketing $\omega=1$ and the four peaks bracketing $\omega=3$ (two above and two below) do not arise from the Autler-Townes model. These represent higher harmonics and are another effect of the atom reacting on the field. Table 1 lists the frequency of each peak from Figure 8b and gives the combination of ω' and $2\lambda_a$, needed to produce it.

If we consider ω' and $2\lambda_a$ each as fundamental frequencies, a parity for each harmonic can be calculated by summing the factors multiplying these fundamentals. Notice the parity in Table 1—the total parity is odd. Even harmonics of ω' are linked with odd harmonics of $2\lambda_a$ and vice versa. A spectrum of $z(t)$ shows the same type of behavior, but with only even parity components. The parity relationship is a natural consequence of the structure of Eqs. 2.5 and 2.9. The prescribed field contains only odd parities, so the prescribed-field solution (Eq. 2.9) for x and y contains odd parities, while z has even parities. When the atom is allowed to react on the field (Eq. 2.5), the parity structure may (or may not) be preserved. As long as no new frequency components are introduced by another mechanism, the structure will be preserved. However, if frequencies of the “wrong” parity are introduced by some means into one variable, the system (2.5) will allow those frequencies to spread to other variables. We will see shortly this is the route to chaos from the neighborhood of the Autler-Townes trajectories.

The obvious question arises: How can frequencies of the “wrong” parity get introduced? They are the result of a shift in various frequency components due to the reaction of the atom upon the field. Using the harmonics given in Table 1 we obtain agreement to four decimal places between the calculated harmonic frequencies and the location of peaks from the FFT. However, to get that agreement, we must use the fundamental frequencies ω' and $2\lambda_a$ from the FFT, not the Autler-Townes model. The

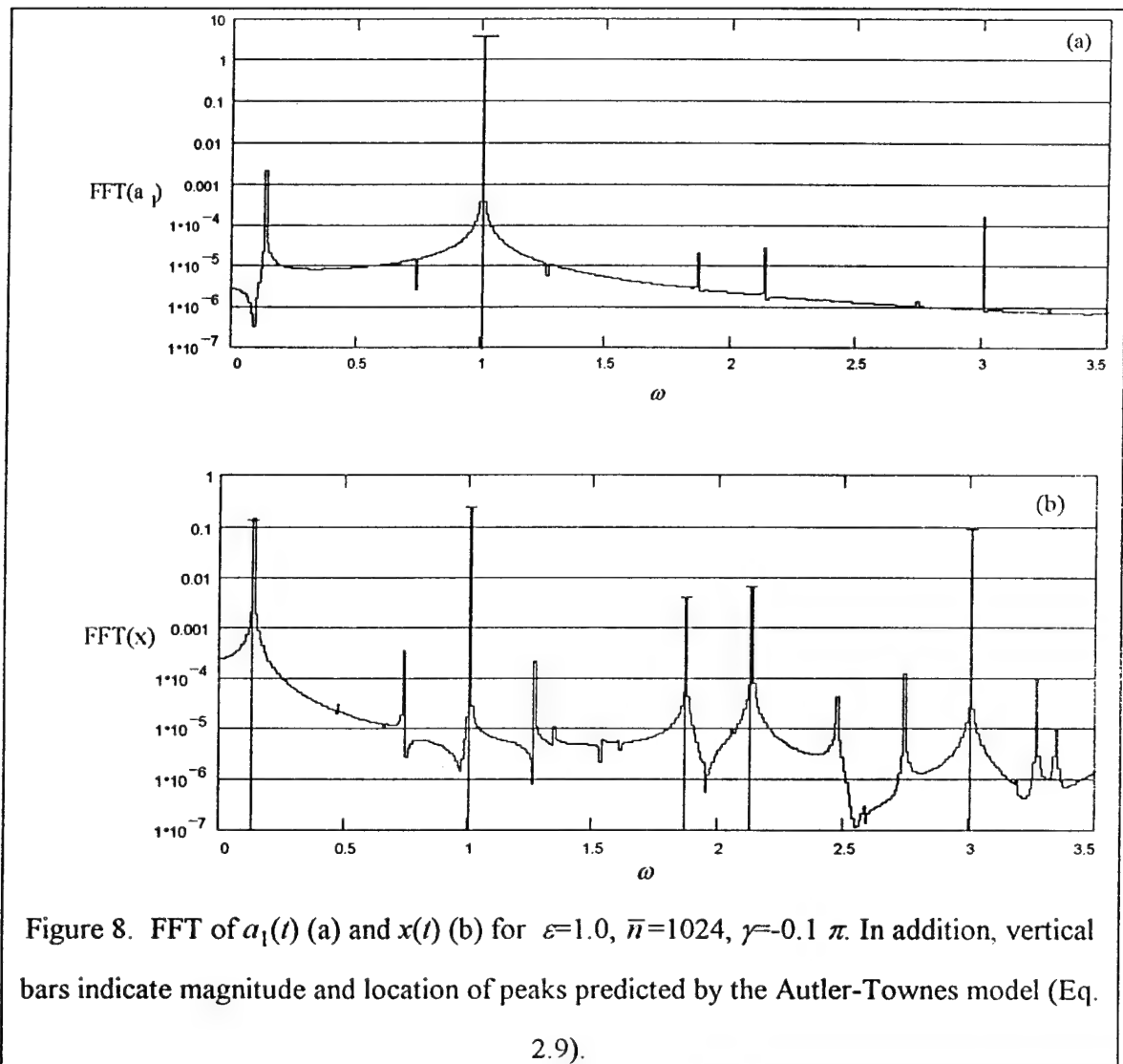
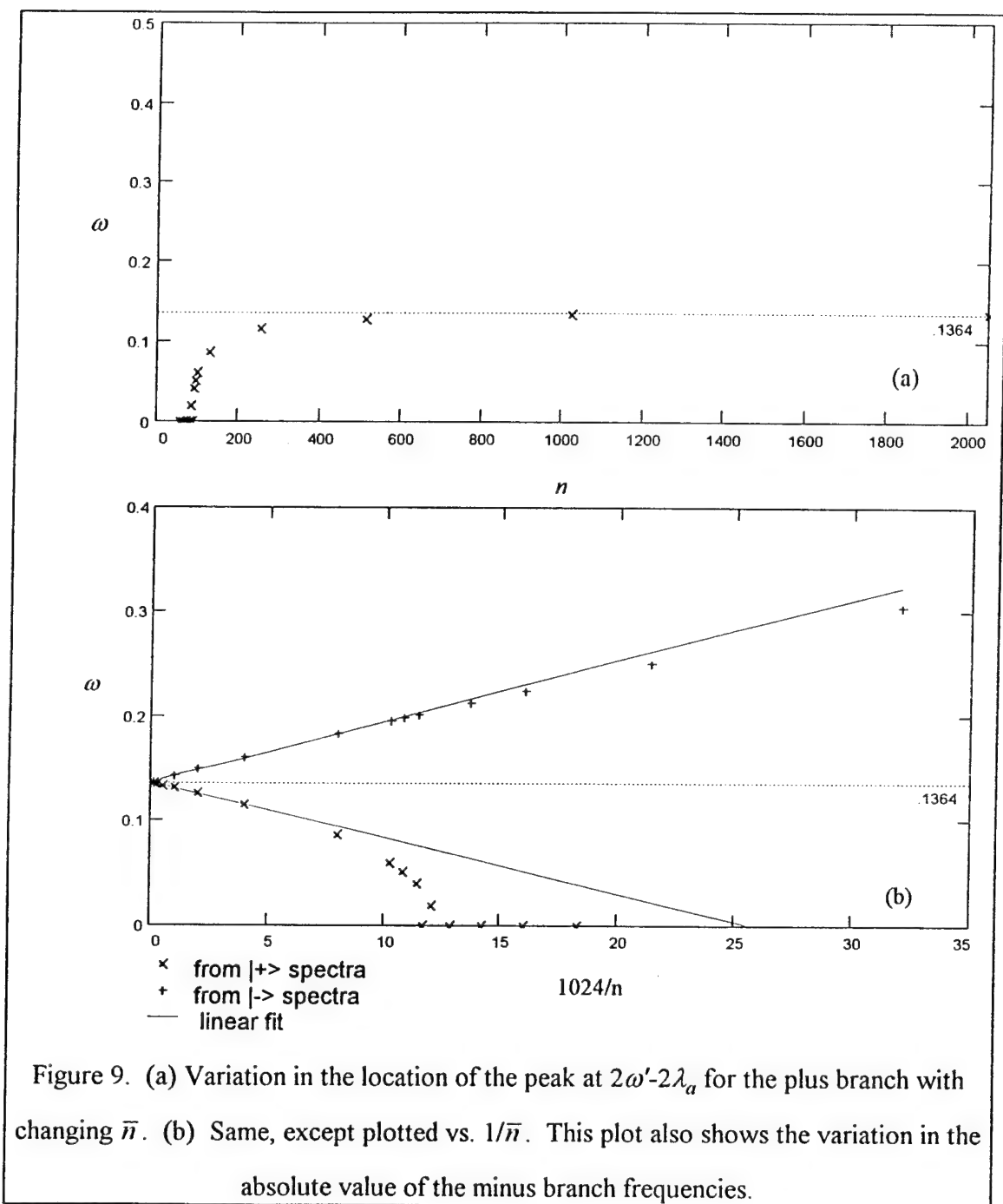


Figure 8. FFT of $\alpha_1(t)$ (a) and $x(t)$ (b) for $\epsilon=1.0$, $\bar{n}=1024$, $\gamma=-0.1 \pi$. In addition, vertical bars indicate magnitude and location of peaks predicted by the Autler-Townes model (Eq. 2.9).

Frequency	Harmonic	Parity
0.1316	$2\omega'-2\lambda_a$	2-1=1
0.4739	$7\omega'-8\lambda_a$	7-4=3
.7372	$3\omega'-4\lambda_a$	3-2=1
1.00045	ω'	1
1.2637	$5\omega'-4\lambda_a$	5-2=3
1.3427	$8\omega'-10\lambda_a$	8-5=3
1.86926	$2\lambda_a$	1
2.1325	$4\omega'-2\lambda_a$	4-1=3
2.4748	$5\omega'-8\lambda_a$	5-4=1
2.7381	$\omega'-4\lambda_a$	1-2=-1
3.0014	$3\omega'$	3
3.2646	$7\omega'-4\lambda_a$	7-2=5
3.3436	$6\omega'-10\lambda_a$	6-5=1

Table 1. List of frequencies found in FFT of $x(t)$ from numerical integration of Eq. 2.5, corresponding harmonics, and parity.



Autler-Townes model predicts the frequencies should be $\omega' = 1.00047\omega$ (using Eq. 2.14) and $2\lambda_a = 1.86360\omega$. Including the detuning has no effect on the calculated value of $2\lambda_a$. Thus, while the Autler-Townes model predicts the detuned ω' frequency to within 0.002%, it does not account for the $2\lambda_a$ discrepancy of 0.3%. One is tempted to attempt a procedure similar to the one which led to Eq. 2.14 to find a detuning for $2\lambda_a$. Unfortunately, such a simple procedure does not work. The difference is in the nature of $2\lambda_a$. It arises as an eigenvalue in the solution of a Floquet eigenvalue problem, and so it involves all the frequency components which appear in the problem, not just one.

Let us examine the behavior of these frequencies with changing \bar{n} . Figure 9a shows the variation in the frequency of the $2\omega' - 2\lambda_a$ harmonic as \bar{n} is varied and shows no obvious pattern. However, plotting the same frequencies versus $1/\bar{n}$, as in Fig. 9b, shows a distinctly linear dependence for sufficiently large \bar{n} . The frequencies from the minus branch require a brief explanation. In terms of the components of the Bloch sphere, all frequencies appear inside of cosine functions (see Eq. 2.9) and so the sign of the frequencies is unimportant. However, Eq. 1.3 shows the actual frequencies of the plus and minus branches are of opposite sign. In order to compare the two branches, the absolute values of the frequencies have been used. Furthermore, because the frequencies come from taking FFTs of real-valued time series, only the positive frequencies are significant. Later we will see that the actual sign of the frequencies is important, but for now we are primarily interested in the magnitudes.

The fit to the plus branch intersects the ω axis at 0.1365 while the fit to the minus branch intersects at $\omega = 0.1372$. Both provide good agreement with the Autler-Townes model prediction of $2 - 1.8636 = 0.1364$. The difference is attributed to the uncertainty in the locations of the peaks in the FFT and in fitting a straight line to the locations of the peaks.

In order to find the correction to $2\lambda_a$ then, let us return to the original eigenvalue problem and search for a linear dependence upon $1/\bar{n}$. First we must express the system (2.4) as an eigenvalue problem. Let us consider first the Autler-Townes model with no atomic reaction on the field. The reaction comes from the term gx in Eq. 2.4e. Deleting that term, we can write $a_1 = \sqrt{\bar{n}} \cos\omega t$, and along with Eqs. 2.4a-c, we obtain a system of linear equations with periodic coefficients. According to Floquet's theorem, there are three solutions (since there are three dimensions) of the form

$$x = e^{i\nu t} \sum_{n=-\infty}^{\infty} x_n e^{in\omega t}, \quad (2.15)$$

where ν is one of three distinct Floquet characteristic exponents. In addition, y and z can be written in the same form. Substituting these forms into Eq. 2.4a-c, we obtain an eigenvalue problem which can be truncated and solved numerically. In doing so, we obtain three values of $\nu = \{0, 2\lambda_a, -2\lambda_a\}$. The solution $\nu=0$ gives the periodic solution of Eq. 2.9 ($\gamma=0, \pi$). The other two solutions must be combined with appropriate choice of signs to obtain real solutions which correspond to Eq. 2.9 with $\gamma = \pm\pi/2$. Although in the Hilbert space of the atomic system (i.e. in terms of $|a\rangle$ and $|b\rangle$) the plus and minus branches represent orthogonal states, in the Bloch sphere they differ only by a minus sign, so they are not independent solutions of the eigenvalue problem derived from Eq. 2.4.

Now to obtain the correction to $2\lambda_a$ we must treat the atomic reaction term as a perturbation. To do so, we shall include the two field equations in our eigensystem. However, the system is then no longer a linear system. If we restrict our interest to trajectories near one of the branches, we can write $x = x^{AT} + \delta x$, where δx will be small, and so on for y, z, a_1 and a_2 . Then substituting into Eq. 2.5 we obtain

$$\dot{x}^{AT} + \delta\dot{x} = -y^{AT} - \delta y \quad (2.16a)$$

$$\dot{y}^{AT} + \delta\dot{y} = x^{AT} - z^{AT} a_1^{AT} + \delta x - z^{AT} \delta a_1 - a_1^{AT} \delta z \quad (2.16b)$$

$$\dot{z}^{AT} + \delta\dot{z} = y^{AT} a_1^{AT} + y^{AT} \delta a_1 + a_1^{AT} \delta y \quad (2.16c)$$

$$\dot{a}_2^{AT} + \delta\dot{a}_2 = -a_1^{AT} - \beta x^{AT} - \delta a_1 - \beta \delta x \quad (2.16d)$$

$$\dot{a}_1^{AT} + \delta\dot{a}_1 = a_2^{AT} + \delta a_2. \quad (2.16e)$$

In Eq 2.16a-c, the terms which involve only the unperturbed solutions cancel, since those are the unperturbed Autler-Townes equations. The field equations must be handled more carefully. Writing Eqs. 2.16d-e as a single second order differential equation, we get

$$\ddot{a}_1^{AT} + \delta\ddot{a}_1 + a_1^{AT} + \delta a_1 = -\beta(x^{AT} + \delta x). \quad (2.17)$$

From here we substitute $a_1^{AT} = 8\varepsilon \cos \mu t$, where $\mu = \omega'/\omega_0$. Then using the expression for ω' given by Eq. 2.14, Eq. 2.17 then becomes

$$\delta\ddot{a}_1 + \delta a_1 = -\beta \delta x - \beta(x^{AT} - x_0 \cos \mu t). \quad (2.18)$$

The term in parentheses in Eq. 2.18 is a small correction to an already small quantity, but cannot be *a priori* ignored. However, numerical integration of the system with and without that term showed negligible differences for \bar{n} in the linear range of Fig. 9. Therefore, the term will be dropped and we obtain the linearized semiclassical system:

$$\delta\dot{x} = -\delta y \quad (2.19a)$$

$$\delta\dot{y} = \delta x - a_1^{AT} \delta z - z^{AT} \delta a_1 \quad (2.19b)$$

$$\delta\dot{z} = a_1^{AT} \delta y + y^{AT} \delta a_1 \quad (2.19c)$$

$$\delta\dot{a}_2 = -\delta a_1 - \beta \delta x \quad (2.19d)$$

$$\delta\dot{a}_1 = \delta a_2 \quad (2.19e)$$

While this system appears almost identical to the original semiclassical model, all the coefficients are now periodic because we have expanded about the unperturbed trajectory. Furthermore, the system can be expanded as a sum of complex

exponentials, such as $\delta x = e^{i\nu t} \sum_{n=-\infty}^{\infty} \delta x_n e^{in\mu t}$. Then the equations of motion can be

written in two parts: the unperturbed part (which does not involve β or $\delta\alpha$) and the perturbation (which does involve β or $\delta\alpha$). We obtain, in matrix form, with $\mu = \omega'/\omega_0$

$$\sum_{n=-\infty}^{\infty} i\nu \begin{pmatrix} \delta a_{1n} \\ \delta a_{2n} \\ \delta x_n \\ \delta y_n \\ \delta z_n \end{pmatrix} e^{i(\nu+n\mu)t} = \sum_{n=-\infty}^{\infty} \begin{pmatrix} -in\mu & 1 & 0 & 0 & 0 \\ -1 & -in\mu & 0 & 0 & 0 \\ 0 & 0 & -in\mu & -1 & 0 \\ 0 & 0 & 1 & -in\mu & -8\varepsilon \cos \mu t \\ 0 & 0 & 0 & 8\varepsilon \cos \mu t & -in\mu \end{pmatrix} \begin{pmatrix} \delta a_{1n} \\ \delta a_{2n} \\ \delta x_n \\ \delta y_n \\ \delta z_n \end{pmatrix} e^{i(\nu+n\mu)t} \\ + \sum_{n=-\infty}^{\infty} \begin{pmatrix} 0 & 0 & 0 & 0 & 0 \\ 0 & 0 & -\beta & 0 & 0 \\ 0 & 0 & 0 & 0 & 0 \\ -z^{AT} & 0 & 0 & 0 & 0 \\ y^{AT} & 0 & 0 & 0 & 0 \end{pmatrix} \begin{pmatrix} \delta a_{1n} \\ \delta a_{2n} \\ \delta x_n \\ \delta y_n \\ \delta z_n \end{pmatrix} e^{i(\nu+n\mu)t} \quad (2.20)$$

Replacing $\cos \mu t$, z^{AT} and y^{AT} with their expansions in complex exponentials allows Eq. 2.20 to be written as an eigenvalue problem, $\nu \mathbf{x} = (\mathbf{A} + \mathbf{B}) \mathbf{x}$. The actual forms of \mathbf{A} and \mathbf{B} are too large ($5 \times \infty \times 5 \times \infty$) to be included here, but truncated forms are included in Appendix A. The first matrix, \mathbf{A} , is the unperturbed part, which is satisfied by the Autler-Townes solution. A specific value of \bar{n} must be selected in order to calculate the detuning. Using $\varepsilon = 1.0$ and $\bar{n} = 1024$, the unperturbed eigenvalues when expanding about the plus branch are

$$\nu = \left\{ \begin{array}{ccc} -1.1378 & -0.1374 & 0.8631 \\ -1.0009 & -4.7 \cdot 10^{-4} & 1 \\ \dots -1.0005 & 0 & 1.0005 \dots \\ -1 & 4.7 \cdot 10^{-4} & 1.0009 \\ -0.8631 & 0.1374 & 0.8631 \end{array} \right\} \quad (2.21)$$

The eigenvalues come in sets of five, with each set separated in frequency by μ . The eigenvector for the eigenvalue $\nu = 0$ corresponds to the periodic trajectory given by Eq. 2.9 with $\gamma = 0, \pi$, as discussed above. Likewise, the eigenvalues $\nu = \pm 2\lambda_a$ ($= \pm 0.1374$) have already been discussed. Note, however, that the eigenvalue obtained by following the convention of Autler and Townes (see Fig. 1 of Ref. 9 and the discussion

which immediately follows it) yields $2\lambda_a/\omega=1.8636=2\mu-\nu$. Again, care must be taken to avoid problems from having multiple, physically equivalent solutions. The field components of both of these eigenvectors are all zero.

The new eigenvalues, $\nu=\pm(\mu-1)$, are simply the interaction-induced detuning, δ . The corresponding eigenvectors give the periodic field oscillations. Like the solutions using $\pm 2\lambda_a$, the periodic field solutions must be obtained from linear combinations of the eigenvectors in order to obtain real solutions. Since the eigenvectors are particularly simple for these eigenvalues, consider how the real solutions are formed. The $\delta\alpha_1$ part of the eigenvector for the positive detuning eigenvalue, $\nu=(\mu-1)$ can be expressed as

$$\begin{aligned}\delta\alpha_1 &= \sum_n \delta\alpha_{1,n} e^{i(n\mu+\nu)t} = \sum_n \delta\alpha_{1,n} e^{i((n+1)\mu-1)t} \\ &= \frac{1}{\sqrt{2}} \sum_n \delta_{-1,n} e^{i((n+1)\mu-1)t} = \frac{1}{\sqrt{2}} e^{-it}\end{aligned}\quad (2.22)$$

where $\delta_{-1,n}$ is the Kronecker delta. If $\nu=m\mu-1$, then Eq. 2.22 can be generalized to

$$\delta\alpha_1 = \frac{1}{\sqrt{2}} \sum_n \delta_{-m,n} e^{i(n\mu+(m\mu-1))t} = \frac{1}{\sqrt{2}} e^{-it} \quad (2.23)$$

Similarly, the $\delta\alpha_2$ part of the eigenvector has an $i/\sqrt{2}$ in the same frequency component. In the same manner, the negative detuning eigenvalue yields

$$\begin{aligned}\delta\alpha_1 &= \frac{1}{\sqrt{2}} \sum_n \delta_{-m,n} e^{i(n\mu+(m\mu+1))t} = \frac{1}{\sqrt{2}} e^{it} \\ \delta\alpha_2 &= \frac{-i}{\sqrt{2}} \sum_n \delta_{-m,n} e^{i(n\mu+(m\mu+1))t} = \frac{-i}{\sqrt{2}} e^{it}\end{aligned}\quad (2.24)$$

Therefore, the real-valued $\delta\alpha_1(t)$ is formed by the sum of the eigenvectors, while $\delta\alpha_2(t)$ is formed by the difference.

The change in the Floquet exponent due to the perturbation (i.e., the reaction of the atom on the field, described by the second matrix, **B**) can be found using standard perturbation techniques. Because of the parity considerations discussed at length earlier in this section, first order perturbation theory yields no change in $2\lambda_a$. The

expression for the first order change in an eigenvalue is

$$w_n^{(1)} = \langle \psi_n^{(0)} | W' | \psi_n^{(0)} \rangle \quad (2.25)$$

where W' is the perturbation and $|\psi_n^{(0)}\rangle$ are the unperturbed eigenvectors. The perturbation matrix elements connect the field and atomic portions of the eigenvectors. However, no eigenvector has non-zero components in both the field and the atomic portions. Therefore, the first order perturbation is zero for all the eigenvalues.

Care must be taken in using second order perturbation theory because the perturbation is non-Hermitian. The appropriate expression for the second order correction to the n th eigenvalue w_n is

$$w_n^{(2)} = \sum_{m \neq n} \frac{\langle \psi_n^{(0)} | W' | \psi_m^{(0)} \rangle \langle \psi_m^{(0)} | W' | \psi_n^{(0)} \rangle}{w_n^{(0)} - w_m^{(0)}}. \quad (2.26)$$

We are interested in the perturbation to the eigenvalues $\nu = \pm 2\lambda_a$ (which are equivalent to the eigenvalues $\nu = \mp 0.1374$). Since these correspond to atomic eigenvectors, based on the discussion in the preceding paragraph the only eigenvectors which will contribute to the sum are the field eigenvectors. Let the unperturbed atomic eigenvector $|\psi^{(0)}\rangle$ correspond to the eigenvalue $\nu (= -0.1374)$. Let the field eigenvalues be denoted by $\alpha_{m\pm} = m\mu \pm \delta$ with the corresponding eigenvector denoted by $|\Phi_{m\pm}^{(0)}\rangle$. Having defined these quantities, Eq. 2.26 becomes

$$\Delta \nu_n^{(2)} = \sum_{\substack{m \\ \pm}} \frac{\langle \psi_+^{(0)} | \mathbf{B} | \Phi_{m\pm}^{(0)} \rangle \langle \Phi_{m\pm}^{(0)} | \mathbf{B} | \psi_+^{(0)} \rangle}{\nu - \alpha_{m\pm}}, \quad (2.27)$$

where the \pm indicates summation over m first with the upper sign and then with the lower sign. Further simplification is achieved by noting that the only non-zero part of $\mathbf{B}|\Phi_{m\pm}^{(0)}\rangle$ which survives is the $\delta\alpha_1$ portion, while only the $\delta\alpha_2$ portion of $\langle\Phi_{m\pm}^{(0)}|\mathbf{B}$ survives. The non-zero component from eigenvector $|\Phi_{m\pm}^{(0)}\rangle$ is $-(m\pm 1)$, as discussed above. In order to find the matrix elements of \mathbf{B} , first express Eq. 2.9 in terms of

complex exponentials. Then let $x_n, y_n,$ and z_n be the coefficients of $e^{in\omega t}$ with $\gamma=0$ and $x'_n, y'_n,$ and z'_n be the coefficients of $e^{i(n\omega-2\lambda_a)t}$ with $\gamma=\pi/2$. Then the matrix elements of **B** are given by $x_n, y_n,$ and z_n . The components of $|\psi_+^{(0)}\rangle$ can be obtained either from the eigenvector corresponding to ν or from $x'_n, y'_n,$ and z'_n after they have been normalized to unity. Equation 2.27 can be expressed as

$$\Delta \nu_n^{(2)} = \beta \sum_{\substack{m \\ \pm}} \frac{\pm \left[\sum_n (y_n'^* z_{n\pm 1+m} - z_n'^* y_{n\pm 1+m}) \right] (-ix'_{\mp 1-m})}{\nu - m\mu \mp \delta}. \quad (2.28)$$

Finally, the summation in the numerator of Eq. 2.28 is exactly equal to $-ix'_{\mp 1-m}$. Thus the second order perturbation can be written in the fairly simple form

$$\Delta \nu_n^{(2)} = \beta \sum_{\substack{m \\ \pm}} \frac{\pm (x'_{\mp 1-m})^2}{\nu - m\mu \mp \delta}. \quad (2.29)$$

Fortuitously, even for values as large as $\varepsilon=1$, only a single term from each sum over m is significant, $m=+1$ from the summation over the upper signs and $m=-1$ from the summation over the lower signs. This simplification leads to the final result

$$\Delta \nu^{(2)} = \frac{2\Delta \lambda_a^{(2)}}{\omega_0} = \beta \frac{x_0'^2}{1 - \left(2\mu - \frac{2\lambda_a^{(0)}}{\omega_0}\right)^2} = \frac{16\varepsilon^2 x_0'^2}{1 - \left(2\mu - \frac{2\lambda_a^{(0)}}{\omega_0}\right)^2} \frac{1}{\bar{n}} \quad (2.30)$$

where x'_0 is the component of the eigenvector which oscillates at the frequency $2\omega' - 2\lambda_a$. Thus we obtain the desired $1/\bar{n}$ dependence for the variation of $2\lambda_a$. For $\varepsilon=1$, Eq. 2.30 evaluates to approximately $6.9/\bar{n}$. This value is in reasonable agreement to a linear least squares fit to the values of $2\lambda_a$, which yields a slope of approximately 6.3.

Examining the perturbation to the other eigenvalue, $-2\lambda_a$ or $\nu=+0.1374$, we find only one difference. The summation over n in Eq 2.28 yields $ix'_{\mp 1-m}$, so there is an overall difference in sign. The perturbed eigenvalues still have the same magnitude as

the perturbed $+2\lambda_a$ eigenvalue, but are opposite in sign. Thus, linearizing in the vicinity of the plus branch yields eigenvalues which tend toward zero with increasing $1/\bar{n}$.

We can now repeat the entire process which led to Eq. 2.28-2.30, but perturbing about the minus branch. The final result of this procedure is a difference in sign for the perturbation. Therefore, linearizing in the vicinity of the minus branch yields eigenvalues which increase in absolute value, i.e., tend away from zero with increasing $1/\bar{n}$.

Reaction of the atom upon the field causes several other effects which can be explored in the same manner. These include generation of extra frequency components in the field, alteration of the magnitudes of the frequency components, and so forth. Several of these have been explored and met with results similar to those above. Therefore, they need not be discussed further.

We are now prepared to return to the question of chaos in the semiclassical system. As the Floquet exponent changes, it can intersect with other frequencies in the system. For the plus branch, the peaks merge near $\bar{n}=90$, as shown in Fig. 10. As the peaks merge, the system becomes chaotic. The "wrong" parity frequency components result from the merging of the different frequency components. Components which previously had no means of interaction can now interact and the result, literally, is chaos.

Figure 11 compares the Euclidean separation of nearby trajectories for $\bar{n}=85$ and $\bar{n}=95$. For $\bar{n}=95$, the trajectory is clearly non-chaotic—the trajectories actually become closer together with time, then return to their original separation. On the semi-logarithmic scale, there are no linear regions indicating exponential growth. Conversely, the $\bar{n}=85$ trajectory exhibits behavior indicating it is on the verge of becoming chaotic. The separation exhibits exponential growth for approximately 1.5 decades before decreasing. Although the growth does not remain exponential for

long, the initial separation is definitely exponential and thus satisfies the definition of chaos. In fact, a fit to the linear portion of the graph gives an exponent 0.042.

However, we can consider the other indicators of chaos as well. Figure 12 shows the sequence of estimated Lyapunov exponents. Like the Euclidean distance, we see regions of exponential growth punctuated by exponential decay. In order to attempt to understand this phenomenon, the time series of x is plotted on the same graph. The time series shows the regions of exponential growth occur when the trajectory is close to the Autler-Townes solution. As the trajectory deviates, as evidenced by the increase in the average value of the oscillations, the growth is damped, only to return as the trajectory returns to the vicinity of the Autler-Townes solution. For this reason we claim the frequency shift from the Autler-Townes solution is related to chaos in the following way: The Autler-Townes trajectory is a periodic trajectory which becomes unstable as a result of these shifts in the frequency. Another indication of chaos is the qualitative change in the spectrum given by the FFT of the time series, as shown in Fig. 13. Observe the contrast between the spectrum for $\bar{n}=95$ and $\bar{n}=85$. Like the spectrum shown earlier for $\bar{n}=1024$, the spectrum for $\bar{n}=95$ consists of a few well separated peaks which can be identified with various harmonics of ω' and $2\lambda_a$. The spectrum for $\bar{n}=85$, on the other hand, shows many more peaks, including peaks of the "wrong" parity, as discussed earlier. Like the Euclidean separation, the FFT does not show the system to be strongly chaotic. However, it does show a qualitative change has occurred and the transition to chaotic behavior is underway.

Finally, consider the Poincaré section. For $\bar{n}=95$, the Poincaré section is a very small oval, as seen in Fig. 14a. The scatter in the points is due to the limited precision in interpolating to find the locations of the zeroes of $x(t)$. Notice how small an area in

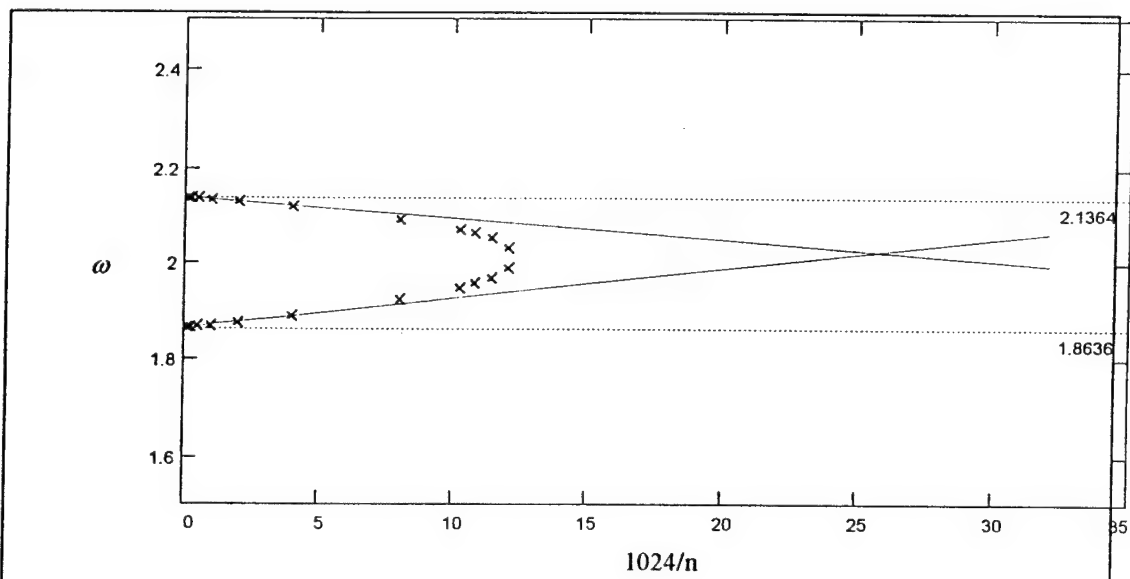


Figure 10. Graph shows that two different harmonics ($4\omega'-2\lambda_a$ and $2\lambda_a$) shift with decreasing \bar{n} and merge. As they merge, the system becomes chaotic. The straight lines indicate a linear fit to the large \bar{n} region.

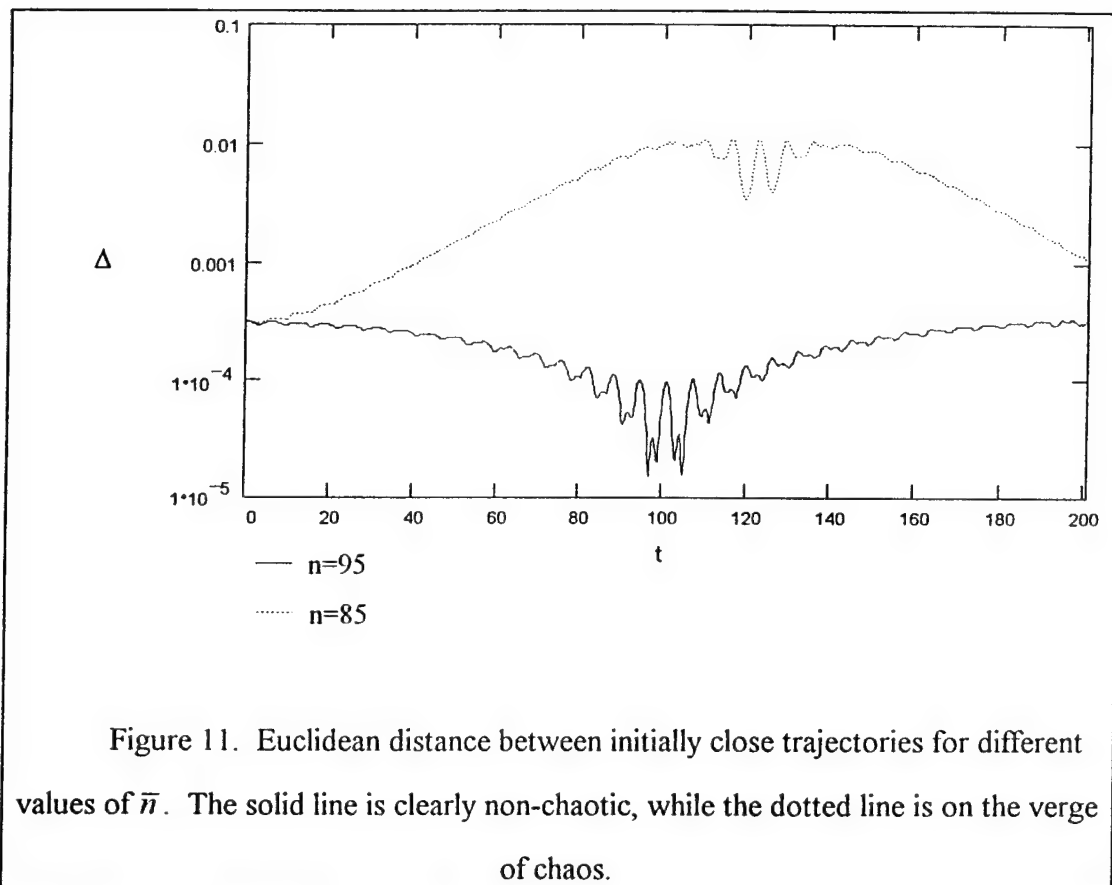


Figure 11. Euclidean distance between initially close trajectories for different values of \bar{n} . The solid line is clearly non-chaotic, while the dotted line is on the verge of chaos.

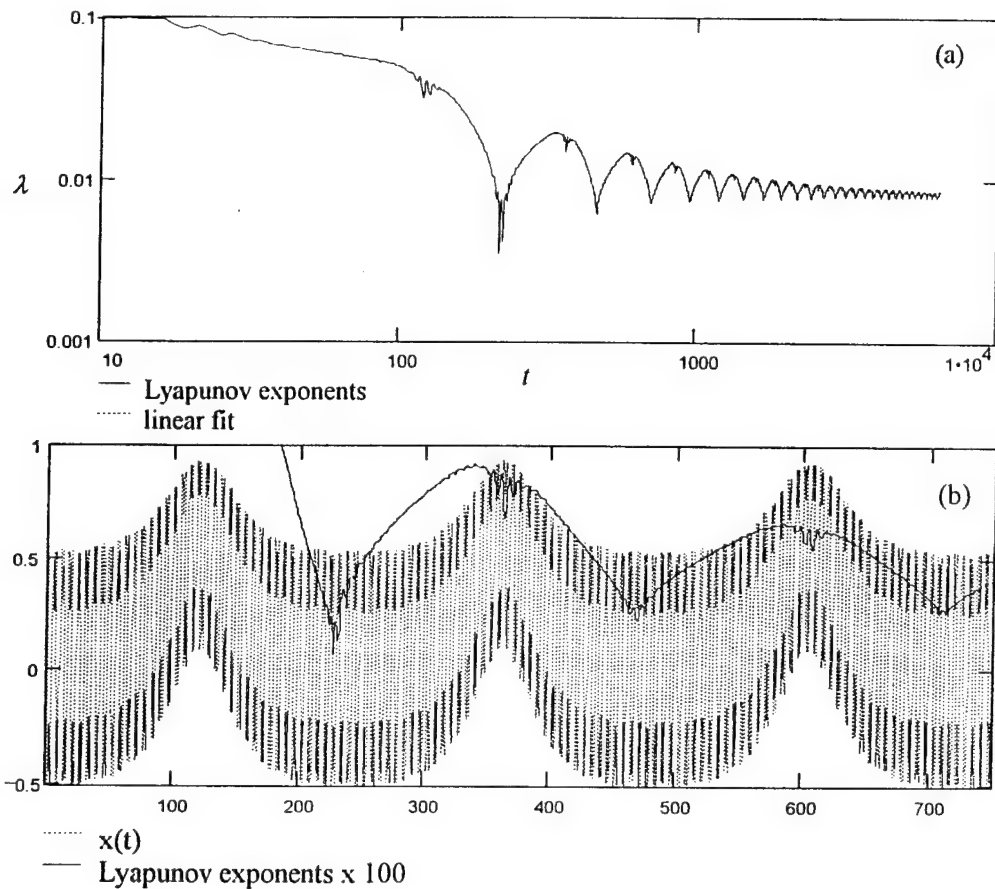


Figure 12. Sequence of Lyapunov exponents for $\varepsilon=1$, $\bar{n}=85$, starting near the plus branch. (a) Dotted lines bracket possible values for the Lyapunov exponent; the dashed line indicates a linear fit. (b) Overlay of $x(t)$ with Lyapunov exponent, showing exponential growth in separation occurs when the trajectory is near Autler-Townes solution (i.e. where oscillations are symmetric about $x=0$).

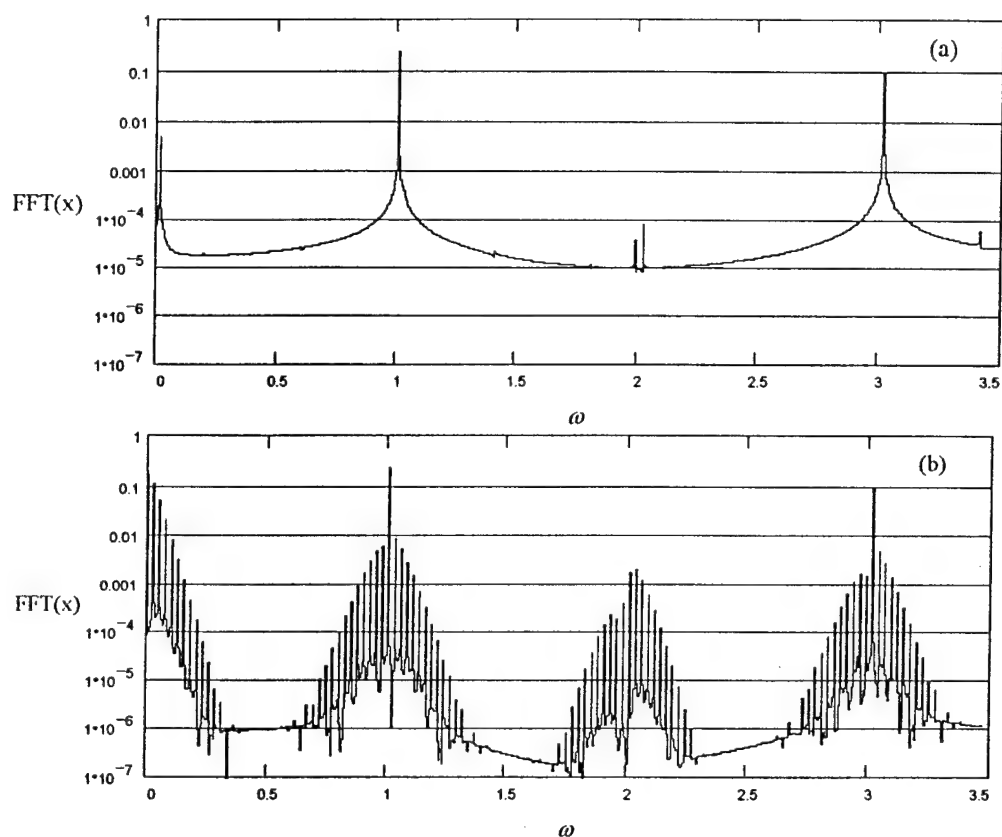


Figure 13. Comparison of FFTs for two trajectories. Both have $\varepsilon = 1$ and start near the Autler Townes plus branch. (a) The trajectory is non-chaotic, with $\bar{n} = 95$.
(b) The trajectory is marginally chaotic, with $\bar{n} = 85$.

the phase space is enclosed. However, Fig. 14b-d shows that as \bar{n} decreases the area enclosed by the Poincaré section increases in size and complexity.

All three tests for chaos show a qualitative change as \bar{n} decreases from 95 to 85. This transition is marked by the merging of two frequency components which results in the system becoming chaotic. The frequency shifts can be traced to an interaction predicted by second-order perturbation theory. Of course, a single instance would not be sufficient to establish a cause and effect relationship, so let us now consider the transition to chaotic behavior for the minus branch with the same value of ε . The magnitude of the slope of the minus branch line in Fig. 9b is approximately 6.5, in reasonable agreement with the value given by Eq. 2.30. There are no frequency components appearing in Eq. 2.9 which are slightly larger than $2\omega' - 2\lambda_a$. However, we do observe in the spectrum of x a harmonic at $-(3\omega' - 4\lambda_a) = 0.7272$. These two peaks merge near $\bar{n} = 32$, and the transition to chaos is much stronger. Using the same tests for chaos, let us examine this transition. First, the Euclidean separation and Lyapunov exponent are shown in Fig. 15. Just as for the plus branch, we observe a change in the behavior of the system as \bar{n} drops from 35 to 30. The Euclidean separation shows an exponential growth, which in this case does not entirely decay before the next growth cycle occurs. An exponential fit yields an exponent of approximately 0.050. The separation between non-chaotic trajectories, while growing, is not exponential. This is very similar to the behavior seen in the Hénon-Heiles system in Sect. 2.1. The Lyapunov exponent for the chaotic trajectory converges to approximately 0.015. The rapidity with which the Lyapunov exponent converges shows the more robust nature of the chaos in this portion (smaller \bar{n}) of the parameter space.

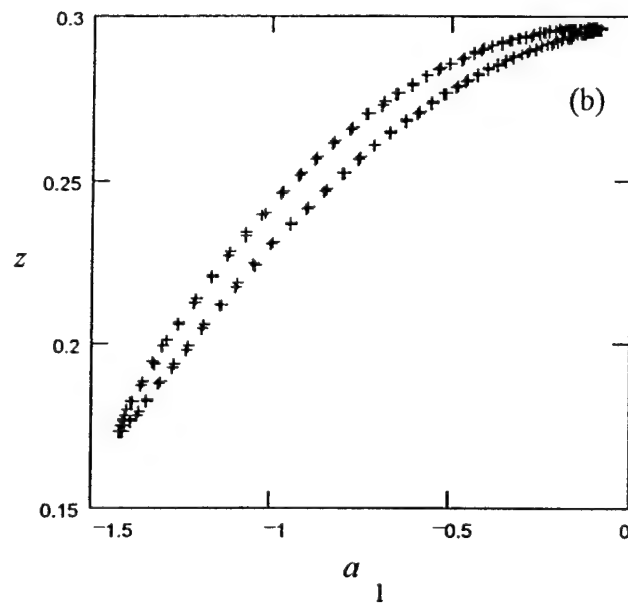
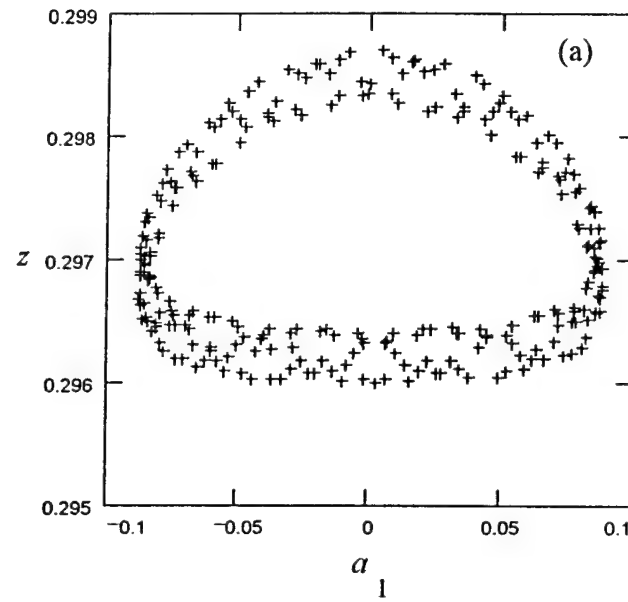


Figure 14. Poincaré sections for trajectories with $\varepsilon=1$, starting from the Autler-Townes plus branch. (a) $\bar{n}=95$ (b) $\bar{n}=93$

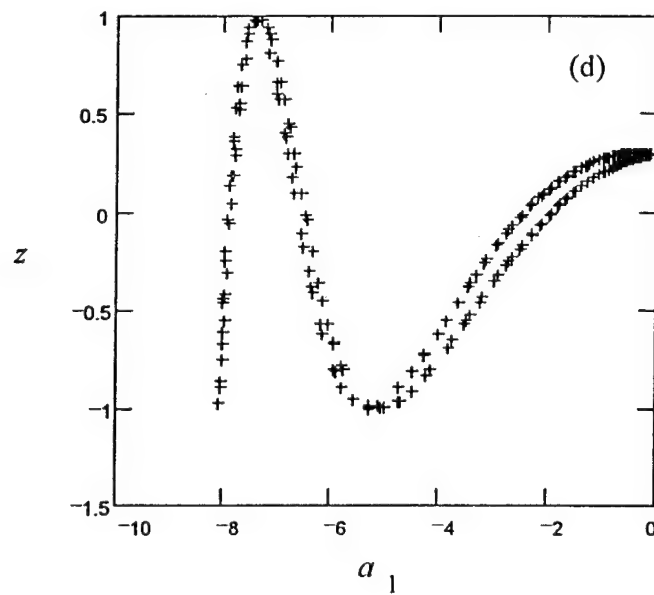
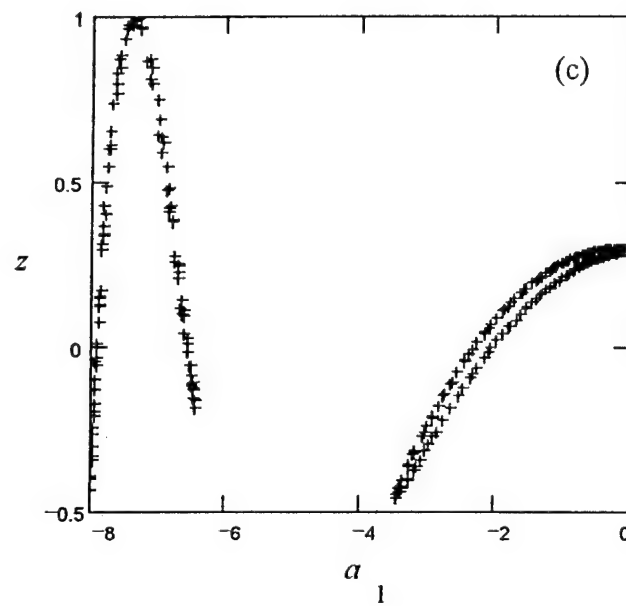


Figure 14. (c) $\bar{n}=90$. (d) $\bar{n}=85$.

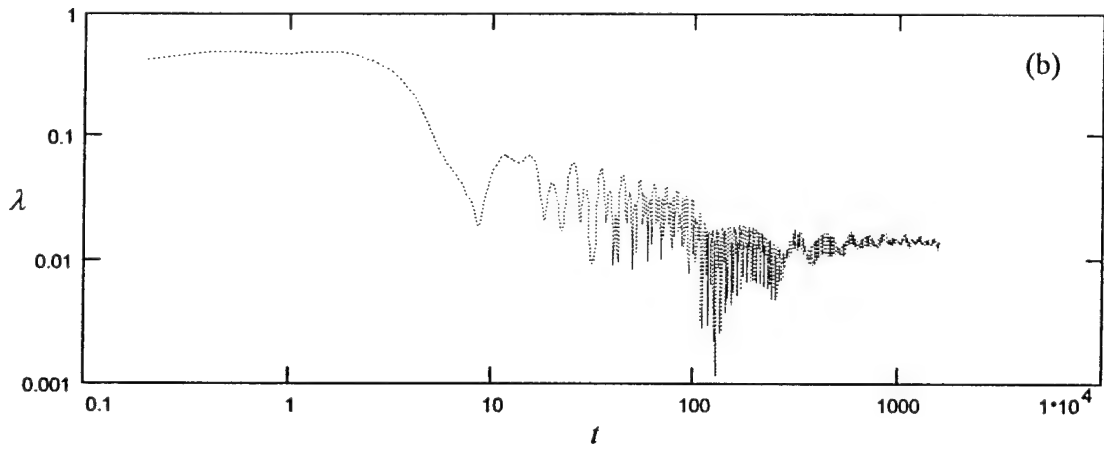
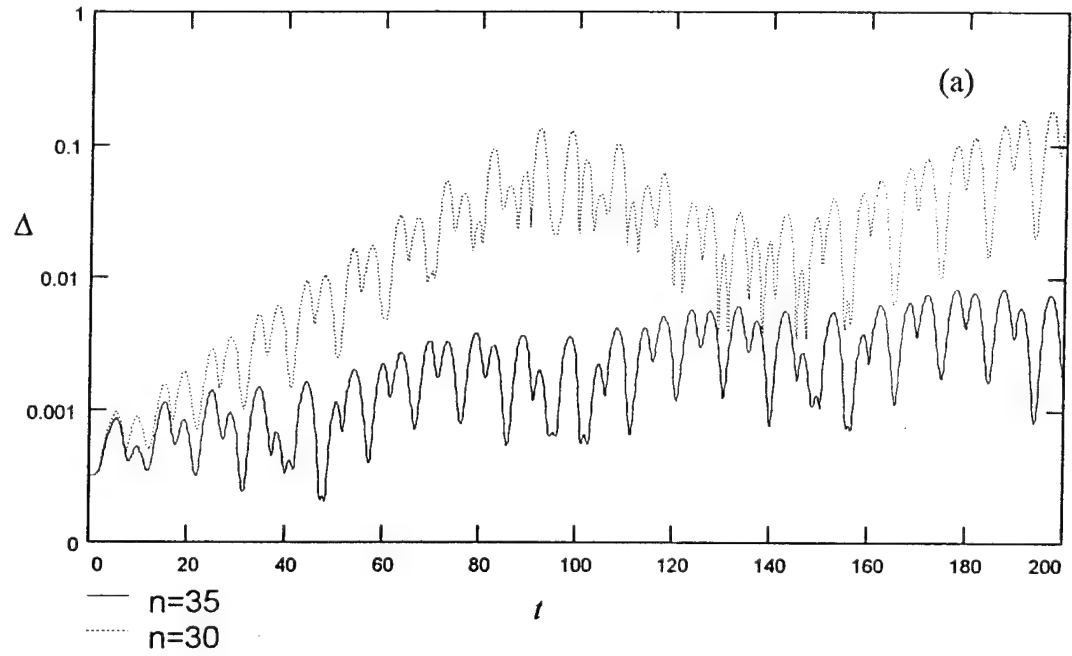


Figure 15. Euclidean separation and Lyapunov exponents for $\epsilon=1.0$, starting near the minus branch. (a) Euclidean separation of initially close trajectories for $\bar{n}=30$ (chaotic) and $\bar{n}=35$ (non-chaotic). (b) Lyapunov exponent sequence for $\bar{n}=30$ converges to $\lambda=0.015$.

The difference in the FFTs for $\bar{n}=30$ and $\bar{n}=32$ also demonstrates the change from regular to chaotic behavior. The two peaks at $\omega=0.304$ and $\omega=0.378$ are the two harmonics which merge ($3\omega'-4\lambda$ and $2\omega'-2\lambda_a$) as discussed above. They have shifted significantly from their $\bar{n} = \infty$ values of $\omega=0.7272$ and $\omega=0.1364$. As with the plus branch, the shift departs from linearity shortly before the peaks merge. As they do, the frequency components become broadband regions instead of individual peaks, demonstrated by Fig. 16. Incidentally, the “wrong” parity frequency components do not become significant, probably because the harmonics did not merge in the vicinity of the frequency components which were absent. Finally, we observe the change in the Poincaré section in Fig. 17. In this instance, the break from regular to chaotic behavior can be observed with increasing time. For $\bar{n} \cong 30.2$, the transition occurs near $t \cong 621$. Before this time, all the points in the Poincaré section fall along the curve formed by the + marks. Afterwards, the points are more scattered, falling generally in the same region as for the plus branch.

The reader should notice an important difference exists between the transition to chaos in the plus and minus branches. Namely, in the minus branch, one of the merging harmonics does not exist in the Autler-Townes model. This harmonic, like the other higher harmonics of $2\lambda_a$ in Table 1, result from the term which was discarded in Eq. 2.17. The relatively low value of \bar{n} suggests that the Autler-Townes model is of relatively little relevance; the success of the approach here is not so much the prediction of chaos, but rather the prediction that chaos occurs sooner for the plus branch than for the minus branch.

Our analytical approach has three important limitations. First, the Autler-Townes trajectory is not identical to the periodic trajectory in the semiclassical model. It is close to the periodic trajectory, but the starting points are not exactly the same, especially for smaller \bar{n} . Second, perturbation theory gives only the lowest order correction in $1/\bar{n}$, i.e., the slope of the $1/\bar{n}$ plot. Third, we have neglected an

inhomogeneous term which generates harmonics which this approach is unable to account for. Nonetheless, these results do demonstrate the transition to chaos occurs by reducing \bar{n} from $\bar{n}=\infty$, where the semiclassical model is identical to the Autler-Townes model, to $\bar{n}<100$, where chaos begins to emerge. Furthermore, we are able to attain a qualitative understanding of why one branch becomes unstable before the other. Before moving ahead to examine the relationship between chaos as it has been observed here and the effects on the full quantum model, we must examine the relationship between the semiclassical model and the quantum model in the non-chaotic region of parameter space.

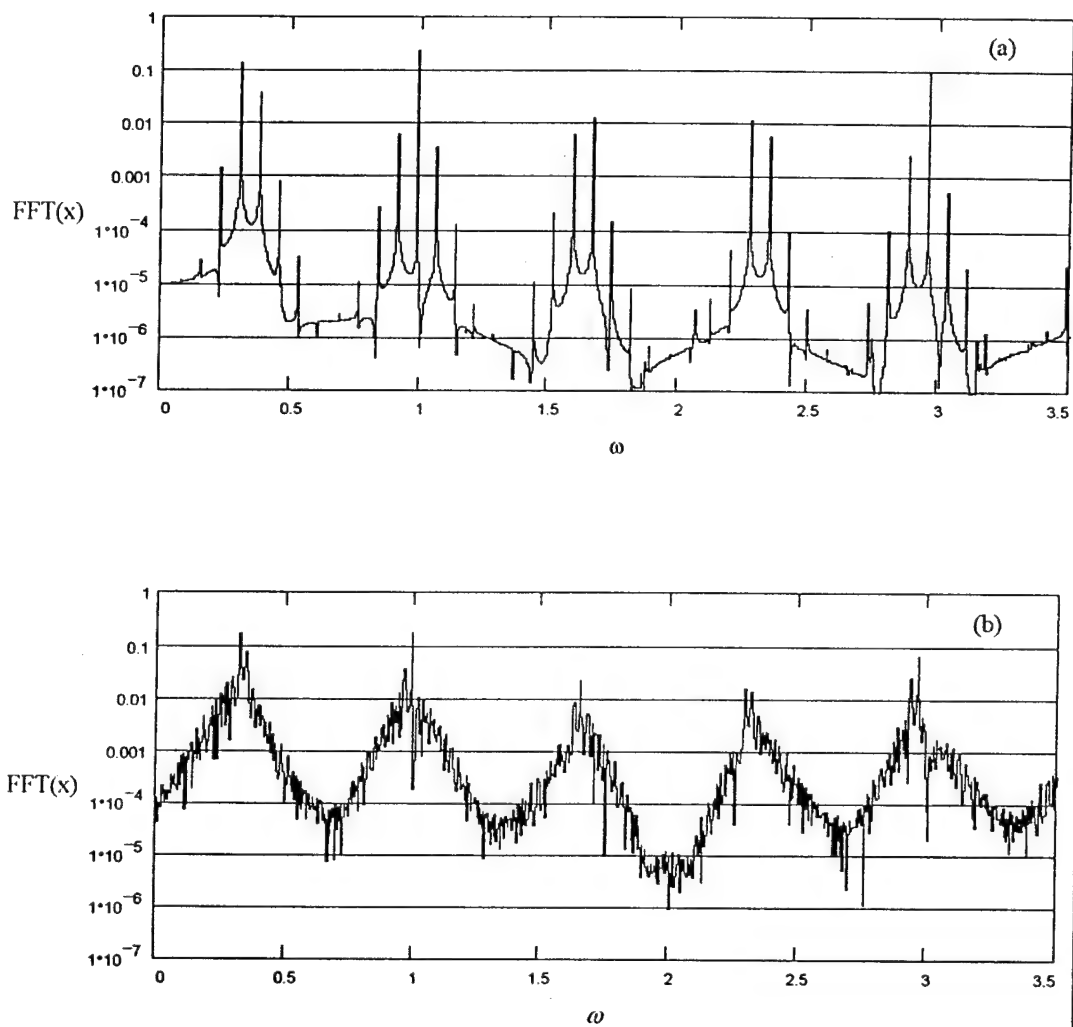


Figure 16. Comparison of FFTs for $\varepsilon=1.0$, starting near minus branch with (a) $\bar{n}=35$ (non-chaotic) and (b) $\bar{n}=30$ (chaotic).

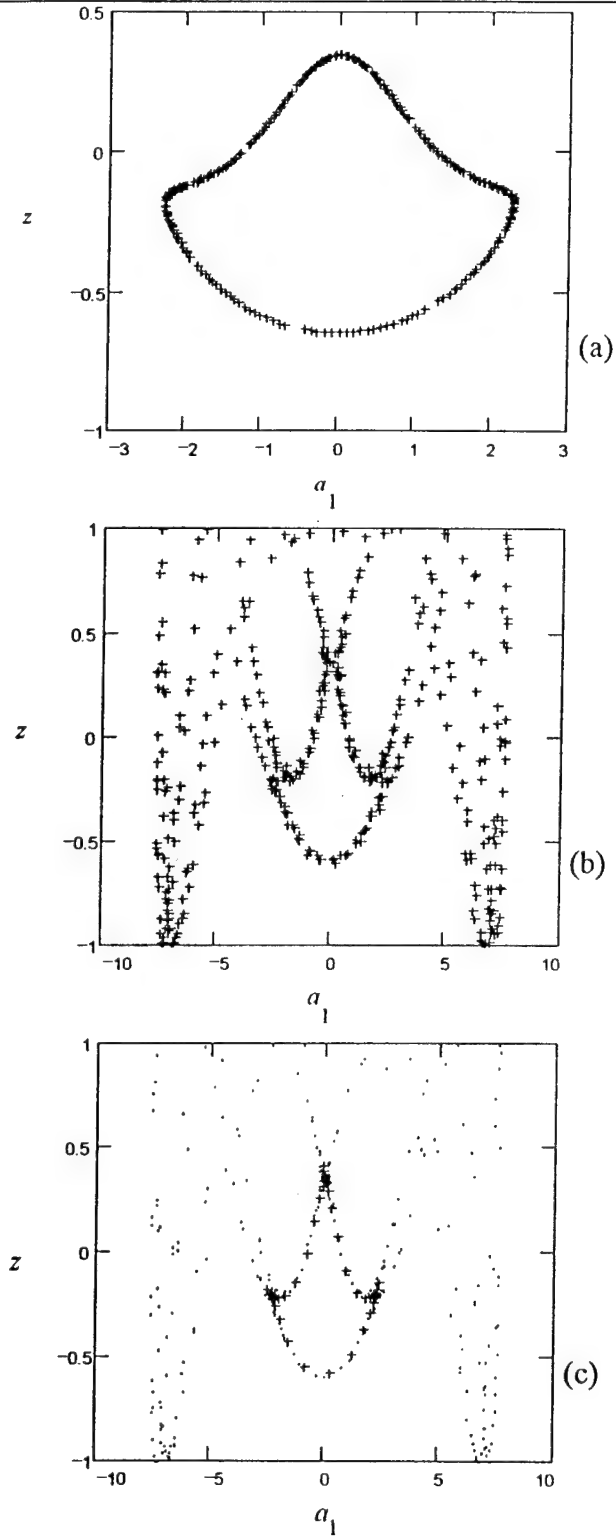


Figure 17. Poincaré sections for minus branch. (a) $\bar{n}=30$. (b) $\bar{n}=32$. (c) Shows transition from near regular orbit with $t < 621$ (+), to unstable orbit with $t > 621$ (-) for $\bar{n}=30.2$.

CHAPTER 3

QUASICLASSICAL STATES AND THE QUANTUM MODEL

In Chapter 2 we pointed out that for a semiclassical treatment to be valid, the atomic and field portions of the wave function must factorize. Assuming that they factorize and then treating the expectation values of the field variables as dynamical variables makes the approximation *semiclassical*. States which actually do remain approximately factorizable have been termed *quasiclassical*. A quasiclassical state will have a relatively well defined field amplitude and phase. If Δn is the uncertainty in the photon number of the state and $\Delta\phi$ is the uncertainty in the field phase, then we require $\Delta n/\bar{n} \ll 1$ and $\Delta\phi \ll 1$. These conditions can be satisfied by coherent states with sufficiently large \bar{n} and squeezed states in which the squeezing is not too large. In this work we will consider only initial conditions which involve coherent states. However, the fact that the approximation remains good for a range of times, even though the field does not remain in a coherent state after $t=0$, demonstrates the broader applicability of the technique.

In Sec. 1 of this chapter we will first give a general development of quasiclassical states and show how the plus and minus branches of the Autler-Townes solutions relate to the quasiclassical states. In Section 2 we will examine the evolution of the field and show how the plus and minus branches may be used to obtain the evolution for arbitrary initial states. Section 3 will give an alternate development using just the eigenstates of the quantum model.

3.1 Development of Quasiclassical States

Let a quantum harmonic oscillator interact with an atomic system. If the oscillator is sufficiently energetic, the atom cannot strongly influence the total energy of the oscillator. As mentioned in Chapter 2, we desire to find states such that

$$|\Psi(0)\rangle = |\psi(0)\rangle \otimes |\alpha\rangle \rightarrow |\Psi(t)\rangle \cong |\psi(t)\rangle \otimes |\Phi(t)\rangle, \quad (3.1)$$

(where $|\Psi(t)\rangle$ is the total wavefunction, $|\psi(t)\rangle$ is the atomic part and $|\Phi(t)\rangle$ is the field part) for times $t > 0$. The atomic system, which could be a two- or three-level system or even a few such systems, has a state space of dimension N . There can then be no more than N quasiclassical trajectories, as follows: Given N quasiclassical trajectories, any other initial condition can be written as a linear combination of the N linearly independent (though perhaps not orthogonal) trajectories. The new initial condition will evolve according to the linear combination of N wavefunctions of the form (3.1). This linear combination will not be generally factorizable.

Classically, if two interacting systems, such as the atom and the field, exchange little energy, we expect the smaller system to have little effect on the larger system. But quantum mechanically the systems can interact in a manner which need not involve substantial energy exchange, through entanglement. By becoming entangled, the smaller system can exert significant influence on the larger system by, for example, causing the larger system to evolve into Schrödinger cat states. By avoiding entanglement (i.e. remaining pure or factorizable), quasiclassical states avoid this quantum mechanical phenomenon and thus the oscillator will be least affected. We expect the oscillations to be approximately constant, but we will allow for a slight modification of the frequency ω to ω' (as we observed in Chap. 2). In order for the system to remain factorizable, we will require that at the end of each period of the oscillator, the atomic system must return to very near its initial state, up to an overall

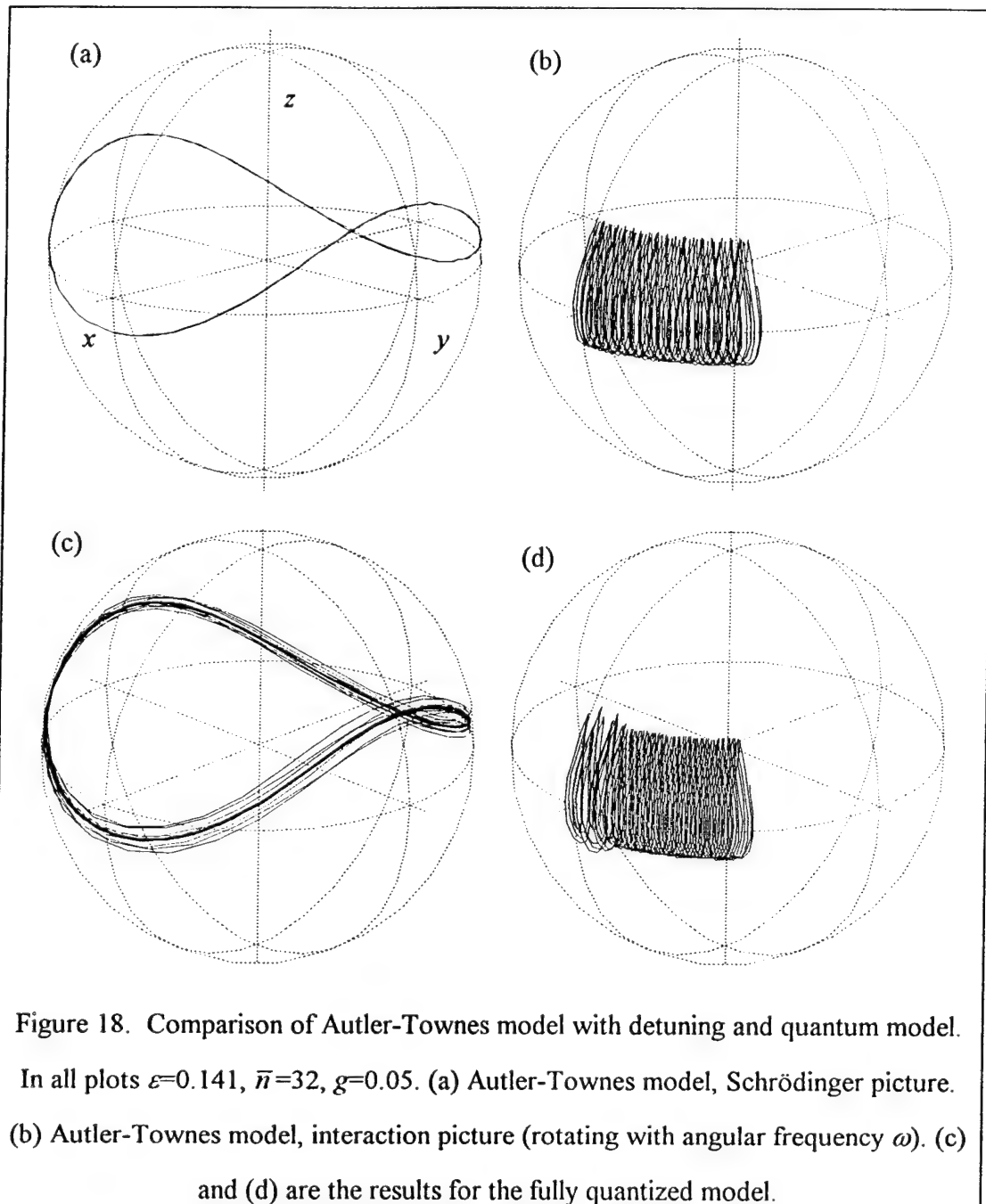
phase factor. To put it another way,

$$|\psi_c(t = 2\pi/\omega')\rangle \cong e^{i\phi_c(2\pi/\omega')} |\psi_c(0)\rangle. \quad (3.2)$$

Taking the form of Eq. 3.2 along with the assumption the oscillator is not significantly disturbed leads naturally to the application of Floquet's theorem to find the quasiclassical states. Making the approximation that the oscillator is unaffected (other than the shift in frequency) leads to the prescribed field Hamiltonian

$$H = \frac{1}{2} \hbar \omega_0 \sigma_z + 2 \hbar g \sqrt{\bar{n}} \sigma_x \cos \omega' t, \quad (3.3)$$

which is the Autler-Townes Hamiltonian introduced in Sect 1.1. Now the connection between the Autler-Townes states and the quasiclassical states is clear: the quasiclassical states must have Floquet-like behavior, while the Autler-Townes states exactly solve a Floquet Hamiltonian. A comparison between the Autler-Townes trajectories for $\bar{n}=32, \epsilon=0.141$ ($g=0.05$) and the numerical integration of the fully quantized system is shown in Fig. 18. The atom starts on the Autler-Townes plus branch, while in this figure and elsewhere unless noted otherwise, the fully quantized field starts in a coherent state with $\alpha = \sqrt{\bar{n}}$. The interaction picture, in which the axis system of the Bloch sphere rotates at the frequency ω_0 , is useful for small ϵ to observe the interaction-induced detuning. The azimuth angle traversed by a particular point along the teardrop-shaped trajectory gives the total drift $(\omega' - \omega)t$. For large ϵ , the trajectories become complicated (recall Fig. 6) and the interaction picture is not particularly useful. In this case, though, the interaction picture demonstrates the similarity of the detuned Autler-Townes model and the fully quantized model, particularly once the quantum model settles down. The total time shown is approximately $t=200$ (in units with ω scaled to 1) or about 32 cycles. The first 5 cycles or so show some differences between the models, but after that time they are virtually identical. The agreement is remarkable, considering the difference in computations required: the quantum model requires integration of nearly

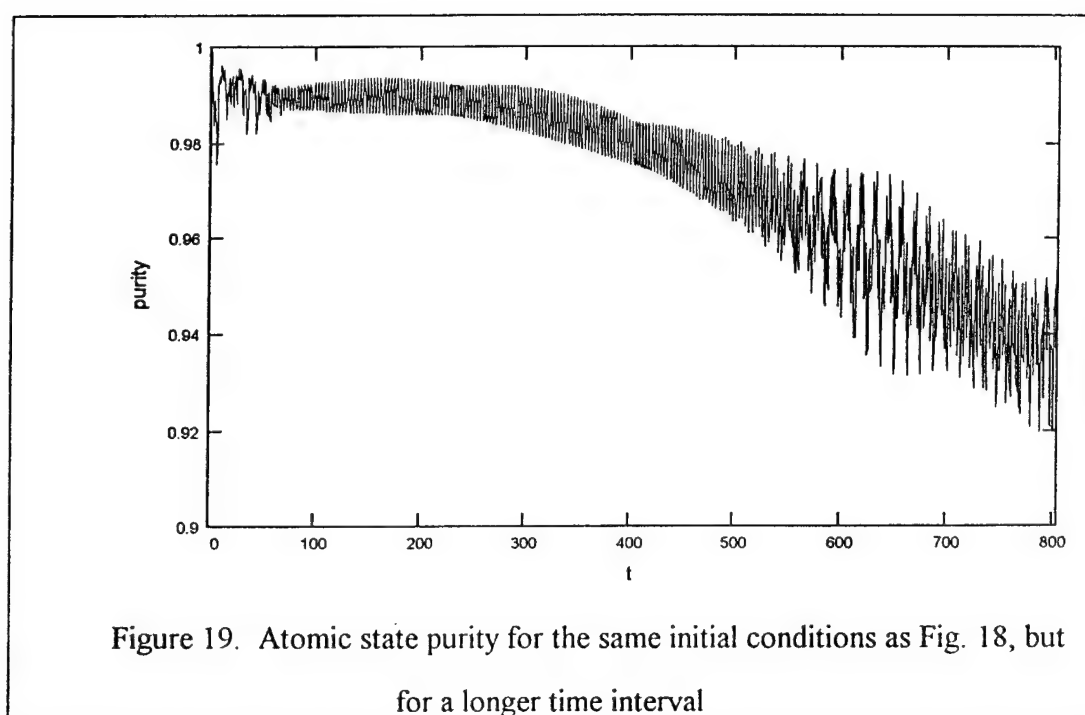


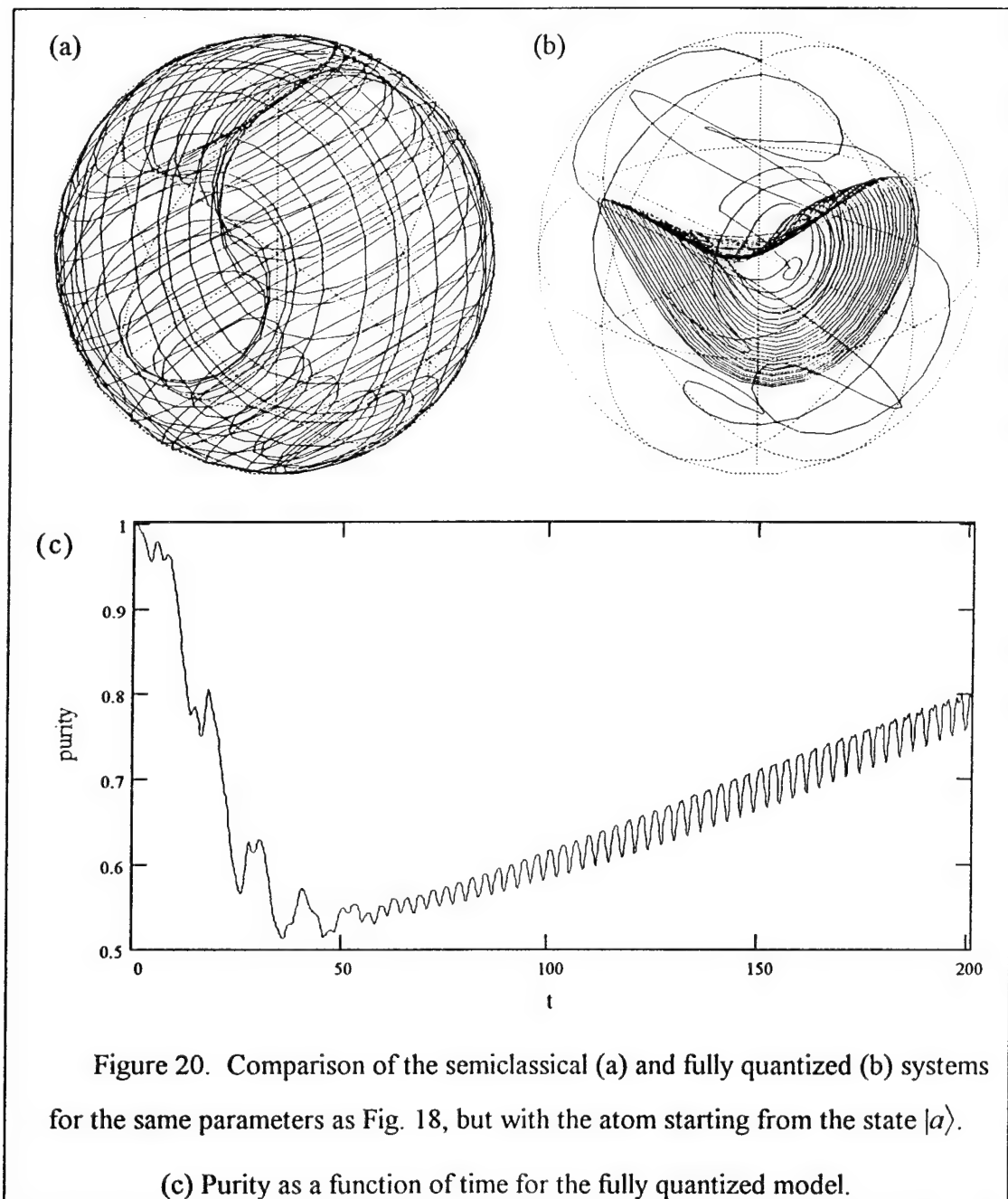
250 equations, while the Autler-Townes results can be obtained by numerically integrating 3 equations or using the closed form expression given by Eq. 2.9, together with the A 's and B 's from Ref. 9. Agreement improves with larger \bar{n} , where the quantum model requires even more effort (roughly $4 \cdot (\bar{n} + 5\sqrt{\bar{n}})$ equations).

The factorization into an atomic part and a field part holds for a fairly long time, as shown by the atomic state purity in Fig. 19. The purity is measured by the $\text{Tr}(\rho_{\text{at}}^2)$, where $\rho_{\text{at}} = \text{Tr}_{\text{field}}(\rho)$ and ρ is the density operator. A purity of 1 indicates a pure state, while the minimum purity for a two level system is 0.5 and indicates a maximally entangled system. In Fig. 19 the purity remains above 0.98 until about $t=400$. This time is about twice the time shown in Fig. 18. To fully appreciate the value of the quasiclassical states, consider the trajectories generated by starting in the state $|\alpha\rangle$ instead of $|\psi_+\rangle$. Figure 20a,b shows the Schrödinger picture evolution of the semiclassical system (2.5) and the fully quantized system for the same parameters as in Fig. 18, but with the atom initially in the upper state. The difference in the two trajectories is immediately obvious as the well-known “collapse” of the wavefunction occurs.^{26,38,40-42} The collapse is even more apparent in Fig. 20c, where the purity rapidly drops off. The approximation of factorization, therefore, is seen to dramatically fail for states which are not near the quasiclassical states. The collapse of a general state is a result of the field splitting into two parts,^{43,44} one associated with the plus branch and one associated with the minus branch. Figure 21 shows the quasiprobability Q distribution at the beginning and end of the trajectories shown in Fig. 20. The Q distribution is defined as

$$Q(\alpha) = \langle \alpha | \rho_{\text{field}} | \alpha \rangle \quad (3.4)$$

where ρ_{field} is obtained from the total density operator, ρ , by tracing over the atomic states. The variable α represents the complex amplitude of a coherent state. This





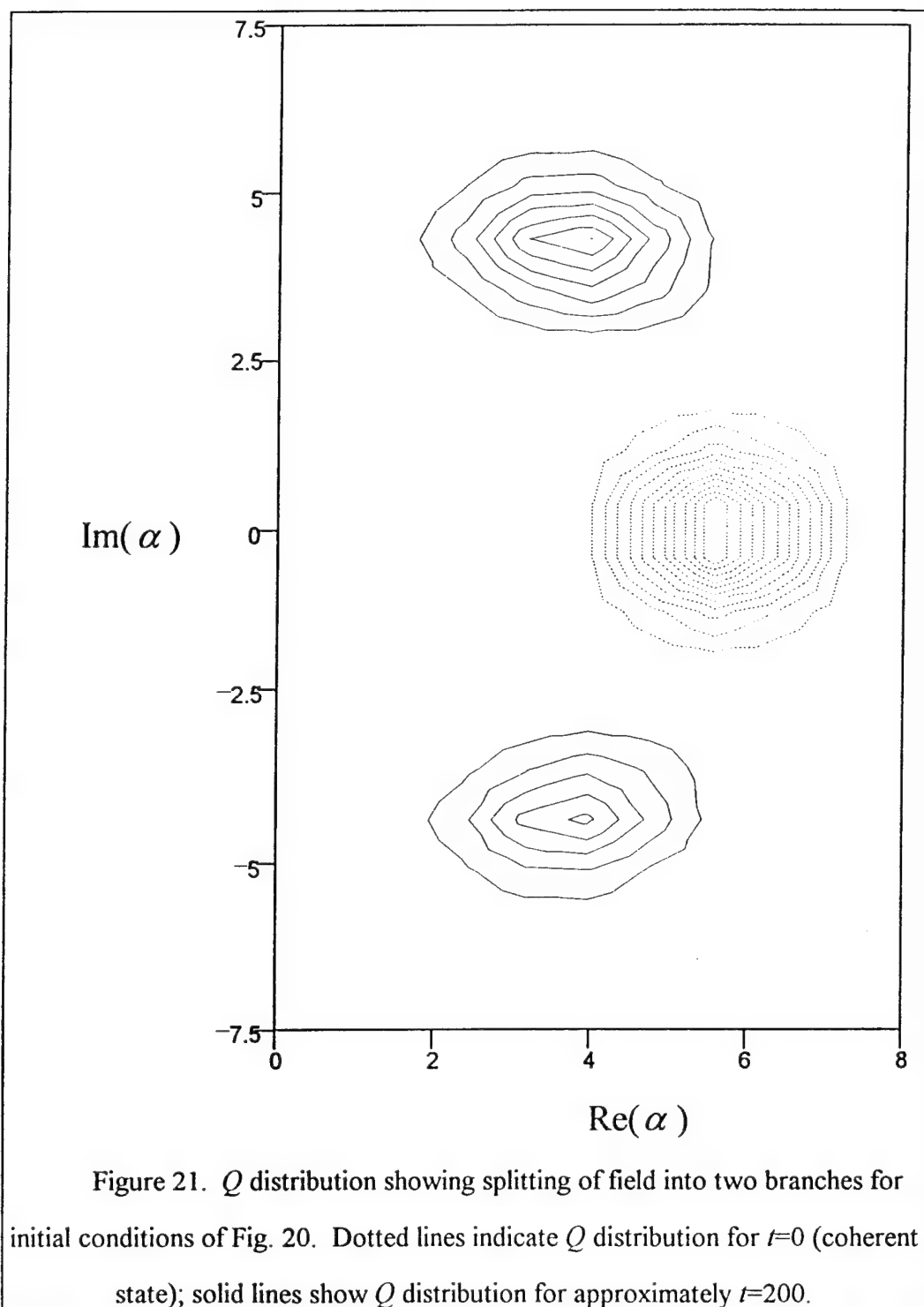
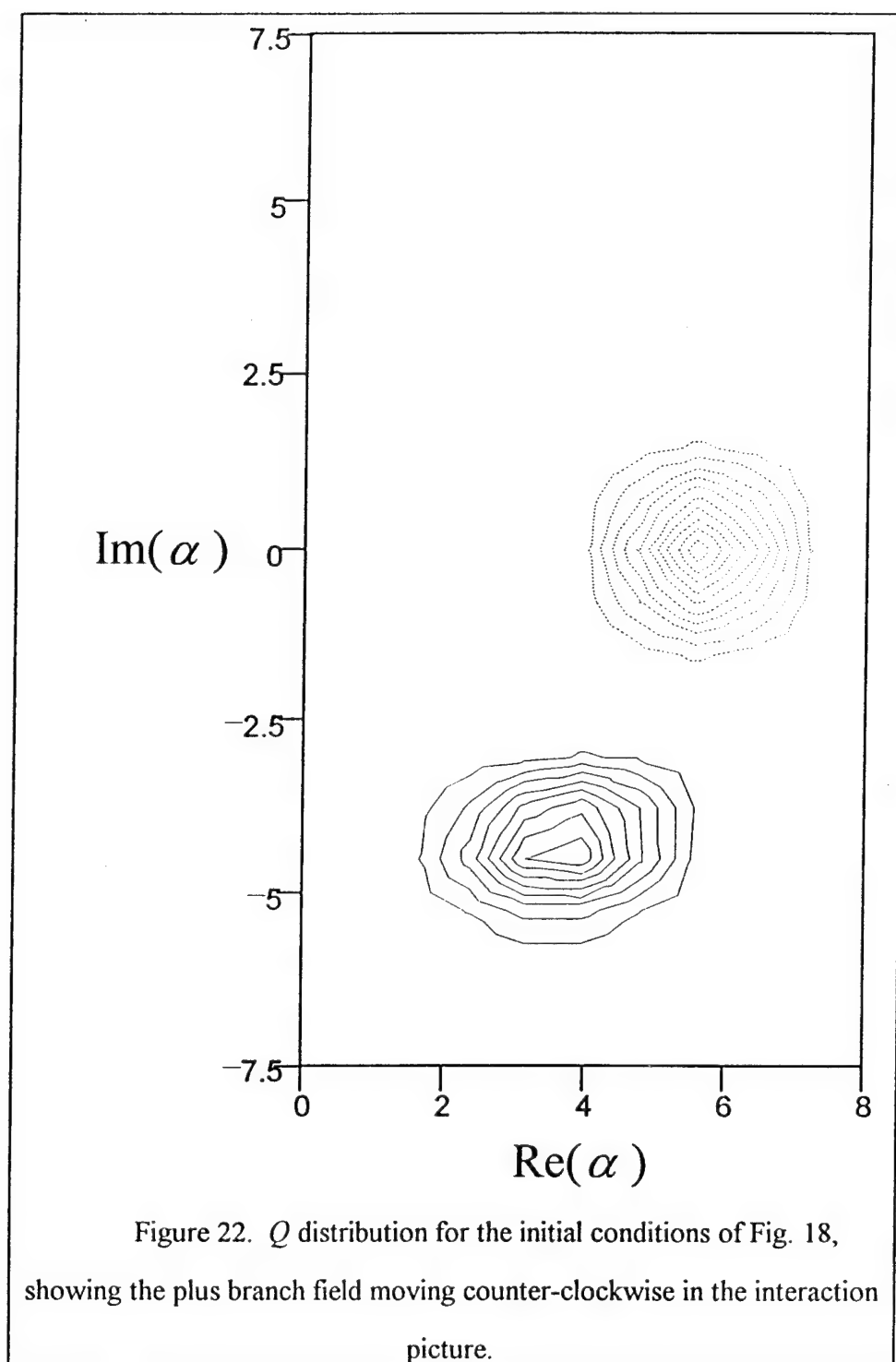
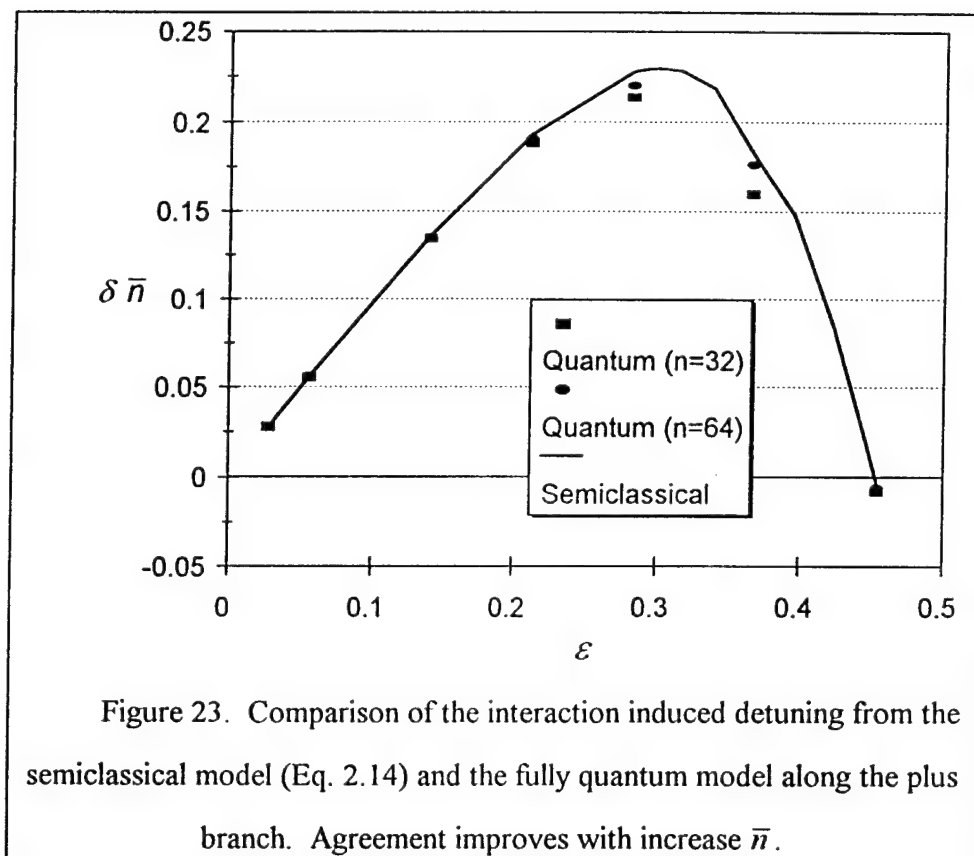


figure is in the interaction picture, rotating with angular frequency $-\omega$. Thus the plus branch portion of the field, which rotates with $\omega' - \omega > 0$ is the lower peak (rotating clockwise), while the minus branch portion of the field is the upper peak (rotating counter-clockwise). Referring to Fig. 7, one can see the state $|a\rangle$, which has $\theta=0$, is closer to the minus branch than the plus branch. As a result, the minus branch portion of the field has a greater weight, and so the peak is bigger (has more contours) in Fig. 21. This association is demonstrated in Fig. 22, where the atom starts on the plus branch and only one peak is observed, rotating clockwise in the interaction picture. We will discuss this further in Sec. 3.2.

The location of the peak of the Q distribution approximately gives the value of the complex field phasor discussed at the end of Sec. 2.2. Using Fig. 22, $\alpha \approx 3.76 - 4.32i$. This yields a detuning of $0.855/201.1 \approx 0.0043$ (please recall in numerical calculations, time has been scaled so that $\omega=1$). The value for the interaction induced detuning given by Eq. 2.14 is 0.00427, in complete agreement at this level of precision. Greater precision can be obtained by calculating the expectation values of the operators a_1 and a_2 , the real and imaginary parts of the boson annihilation operator, and using the same procedure for constructing the complex field phasor. This technique yields a value for the detuning of 0.00422, which is in remarkable agreement considering the differences in the models. In fact, this technique provides good agreement over a fairly broad range of values for ε . Letting the product of the detuning and the average photon number be given by $\delta\bar{n}$, Figure 23 plots $\delta\bar{n}$ versus ε . The solid line gives the value from Eq. 2.14, while the squares and circles give the values calculated from the quantum model for $\bar{n}=32$ and 64, respectively. This figure demonstrates the improved agreement which can be obtained by increasing \bar{n} . Incidentally, if this procedure was used to calculate the detuning in the quantum model





for a situation like that in Fig. 20, the value would be almost zero, since the contributions from the two peaks would nearly cancel each other.

Like the correspondence between the Autler-Townes model and the semiclassical model, the correspondence between the quasiclassical states and the semiclassical model improves with increasing \bar{n} . Using Eq. 2.4, the expansion of x and a_1 as complex exponentials, and Ref. 38 for the series expansion of the Autler-Townes A and B coefficients in ε , we find that

$$a_1^{(\omega=3\omega')} = \frac{O(\varepsilon^3)}{\sqrt{\bar{n}}}. \quad (3.5)$$

Therefore, the third and higher harmonics can be made negligible given sufficiently large \bar{n} . Thus, the agreement between the quantum solution along a particular branch and the Autler-Townes Floquet eigenstates (or the semiclassical solution) can be made as close as desired for fixed ε by increasing \bar{n} . On the other hand, by fixing \bar{n} , the agreement deteriorates with increasing ε .

3.2 Evolution of the Field and of Arbitrary Initial States

Up to this point, almost all the attention has been focused upon the evolution of the atom. Now we shall consider the evolution of the field for the quantum model. The semiclassical model gives expectation values for the field quadratures a_1 and a_2 along a single branch; however, we need more information about the quantum field state in order to calculate the evolution of linear combinations of the two branches. To find how the quantum field evolves, assume a factorized form $|\Psi_+(t)\rangle = |\psi_+(t)\rangle \otimes |\Phi_+(t)\rangle$ for the total wavefunction and insert it into the time-dependent Schrödinger Equation:

$$\frac{\partial}{\partial t} (|\psi_+(t)\rangle \otimes |\Phi_+(t)\rangle) = -\frac{i}{\hbar} H(|\psi_+(t)\rangle \otimes |\Phi_+(t)\rangle). \quad (3.6)$$

Now project out the portion which follows along the atomic quasiclassical trajectory

$$\begin{aligned}\langle \psi_+(t) | \frac{\partial}{\partial t} (| \psi_+(t) \rangle \otimes | \Phi_+(t) \rangle) \rangle &= \left(\langle \psi_+(t) | \frac{\partial}{\partial t} | \psi_+(t) \rangle \right) | \Phi_+(t) \rangle + \frac{\partial}{\partial t} | \Phi_+(t) \rangle \\ &= -\frac{i}{\hbar} \langle \psi_+(t) | H | \psi_+(t) \rangle | \Phi_+(t) \rangle\end{aligned}\quad (3.7)$$

On the RHS of the first line of Eq. 3.7, the derivative w.r.t. time of the atomic state appears. This derivative is given by the action of the Floquet Hamiltonian (including the interaction induced detuning)

$$\left(\langle \psi_+(t) | \frac{\partial}{\partial t} | \psi_+(t) \rangle \right) = -\frac{i}{\hbar} \langle \psi_+(t) | H_{AT} | \psi_+(t) \rangle. \quad (3.8)$$

Making this substitution in Eq. 3.7, we obtain an equation for the evolution of the field

$$\frac{\partial}{\partial t} | \Phi_+(t) \rangle = -\frac{i}{\hbar} \langle \psi_+(t) | (H - H_{AT}) | \psi_+(t) \rangle | \Phi_+(t) \rangle \quad (3.9)$$

and then substitute H and H_{AT} from Eq. 1.1 and Eq. 1.2 to get

$$\frac{\partial}{\partial t} | \Phi_+(t) \rangle = -i \left[\alpha \alpha^\dagger a + g x_+(t) (a + a^\dagger - 2\sqrt{n} \cos \omega' t) \right] | \Phi_+(t) \rangle. \quad (3.10)$$

In this manner the technique has come full circle: We started by assuming factorization and found the atomic evolution using the expectation values for the field in a coherent state $|\alpha\rangle$ with $\alpha = \sqrt{n} e^{-i\omega t}$. Then we used the expectation values for the atom and found the evolution of the field.

The full solution to Eq. 3.10 is a coherent state times a phase factor and is given in Ref. 38. Here we note only that to lowest order in ε/\bar{n} , the complex amplitude of the coherent state is

$$\alpha_+(t) = \sqrt{\bar{n}} e^{-i\omega' t} \left[1 + O\left(\frac{\varepsilon}{\bar{n}}\right) \right]. \quad (3.11)$$

Similar results are found for the minus branch by replacing the plus branch expectation values with those for the minus branch and using the value of ω' for the minus branch.

Similar analysis for quasiclassical states using the rotating wave approximation (RWA) has shown the field states do not remain coherent for very long times, but rather exhibit squeezing.^{10,45} In fact, inspection of Fig. 22 shows the state is no longer coherent, but has increased phase uncertainty. However, numerical calculations show the coherent state approximation to be adequate for short enough times (see below). As discussed at the beginning of this chapter, the existence of quasiclassical states does not depend on the precise form of the field, so long as the phase and amplitude remain fairly well defined.

Having an expression for the field evolution along each branch, we can now move on to the evolution of the field and atom for an arbitrary initial atomic state. Since the two branches at $t=0$ are orthogonal, any atomic state can be written as a linear superposition of the two branches. Using the same form as in Eq. 2.9, we can write

$$\begin{aligned} |\Psi(0)\rangle &= \left(\cos \frac{\gamma}{2} |\psi_+(0)\rangle + e^{i\phi} \sin \frac{\gamma}{2} |\psi_-(0)\rangle \right) \otimes |\alpha(0)\rangle \\ &\rightarrow \cos \frac{\gamma}{2} |\psi_+(t)\rangle |\Phi_+(t)\rangle + e^{i\phi} \sin \frac{\gamma}{2} |\psi_-(t)\rangle |\Phi_-(t)\rangle \end{aligned} \quad (3.12)$$

The detuning for each branch is opposite in sign, so the field states drift apart until they become approximately orthogonal. In terms of the Q distribution, the states are orthogonal when the two peaks are well separated, i.e., they do not overlap. The width of the distribution $Q(\alpha)$ for a coherent state $|\alpha'\rangle$ is independent of the complex amplitude α' , and is approximately equal to unity. However, from the origin, the angle subtended by the distribution (i.e., the phase uncertainty) falls as $1/|\alpha'| = 1/\sqrt{n}$.

Therefore, the two branches will be roughly separated at a time t_c , such that $|\omega' - \omega|t_c = 1/\sqrt{n}$. Use of Eq. 2.14 for the detuning yields

$$\alpha_c \equiv \frac{\sqrt{n}}{\epsilon|x_0|} = \frac{2}{g|x_0|}. \quad (3.13)$$

where x_0 is amplitude of the first term in the cosine expansion (2.12) of $x(t)$ along one of the branches. This time is the collapse time, referring to the collapse of the wavefunction mentioned at the beginning of Sect 3.1. It is called a collapse because in the RWA, after the collapse the Rabi oscillations in the inversion cease. However, the collapse is actually the collapse of the interference terms between the field states along each branch. For a fixed value of ε , which fixes the value of x_0 , the time to achieve collapse grows with \bar{n} . For the case shown in Fig. 18, Eq. 3.13 yields $\omega t_c = 41.2$, which agrees well with the time of the collapse shown in Fig. 20. Alternatively, for fixed g , the collapse time depends only indirectly upon \bar{n} (through x_0). This result is comparable to the result for the RWA, for which t_c is independent of \bar{n} . After the collapse occurs, the expectation values of most quantities are given by a weighted average along each branch separately (with weights $\cos^2 \gamma/2$ and $\sin^2 \gamma/2$ for the plus and minus branches, respectively).

Finally, the two field states will overlap as $|\omega' - \omega|t_R = \pi$. This overlap will result in a revival of interference, which will occur at

$$\omega t_R = \frac{\pi \bar{n}}{\varepsilon |x_0|} = \frac{2\pi\sqrt{\bar{n}}}{(g/\omega)|x_0|}. \quad (3.14)$$

This result agrees with the work done by Zaheer and Zubairy⁴⁶. For $g = 1/5\sqrt{10}$, $\bar{n} = 10$, $\varepsilon = 0.1$, they show in their Fig. 2 a revival which peaks near $2gt = 40$, or $\omega t = 316$. Equation 3.14 yields a value of $\omega t_R = 319$. However, this small value of ε is insufficient to distinguish these results from the RWA, for which the revival time is given by Eq. 3.14 with x_0 set equal to unity. The RWA yields for these parameters $\omega t_R = 314$. Using a larger value of $\varepsilon = 0.3$ and $\bar{n} = 36$, Fig. 24 shows a rather indistinct revival occurring in the vicinity of $\omega t = 500$. For these values, Eq. 3.14 yields a revival time of $\omega t_R = 491$, while the RWA yields $\omega t_R = 377$, in sharp contrast. In order to better determine when the revival occurs, Fig. 25 shows the contribution to the inversion from just the

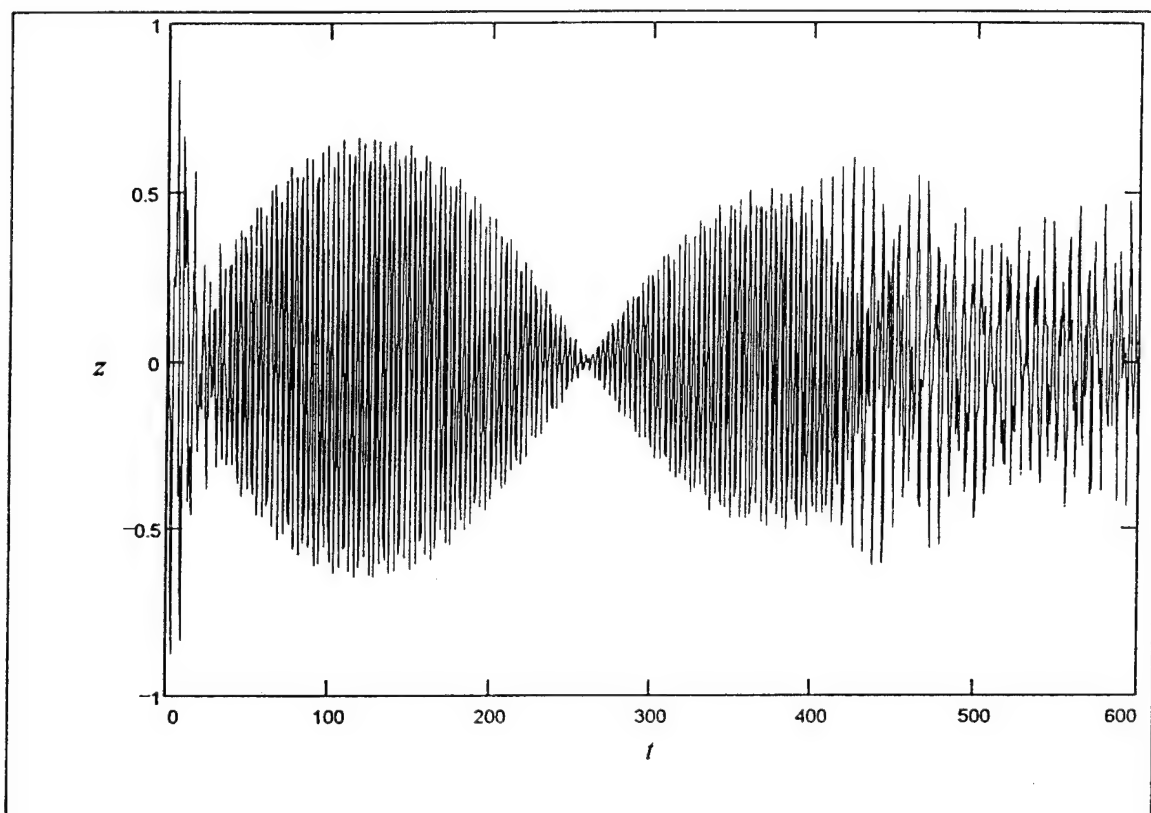


Figure 24. Inversion as a function of time for a state which starts as a linear combination of $|\psi_+(0)\rangle$ and $|\psi_-(0)\rangle$ with equal weights, with $\varepsilon=0.3$ and $\bar{n}=36$. A rather indistinct revival can be seen around $t=500$.

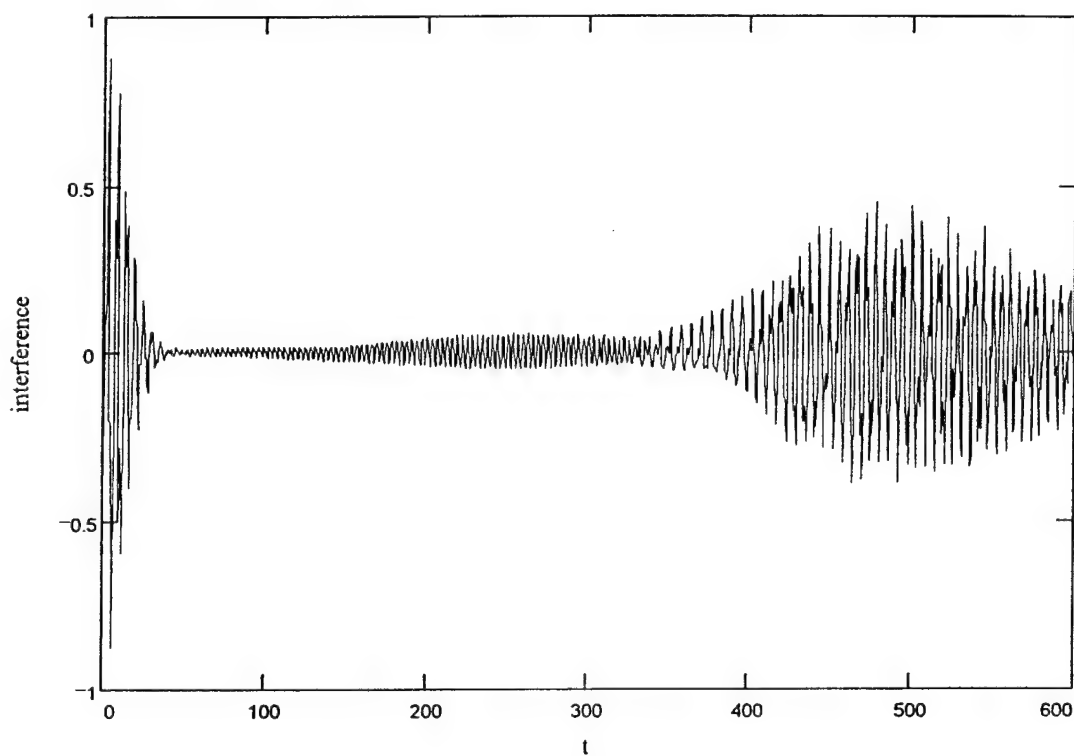
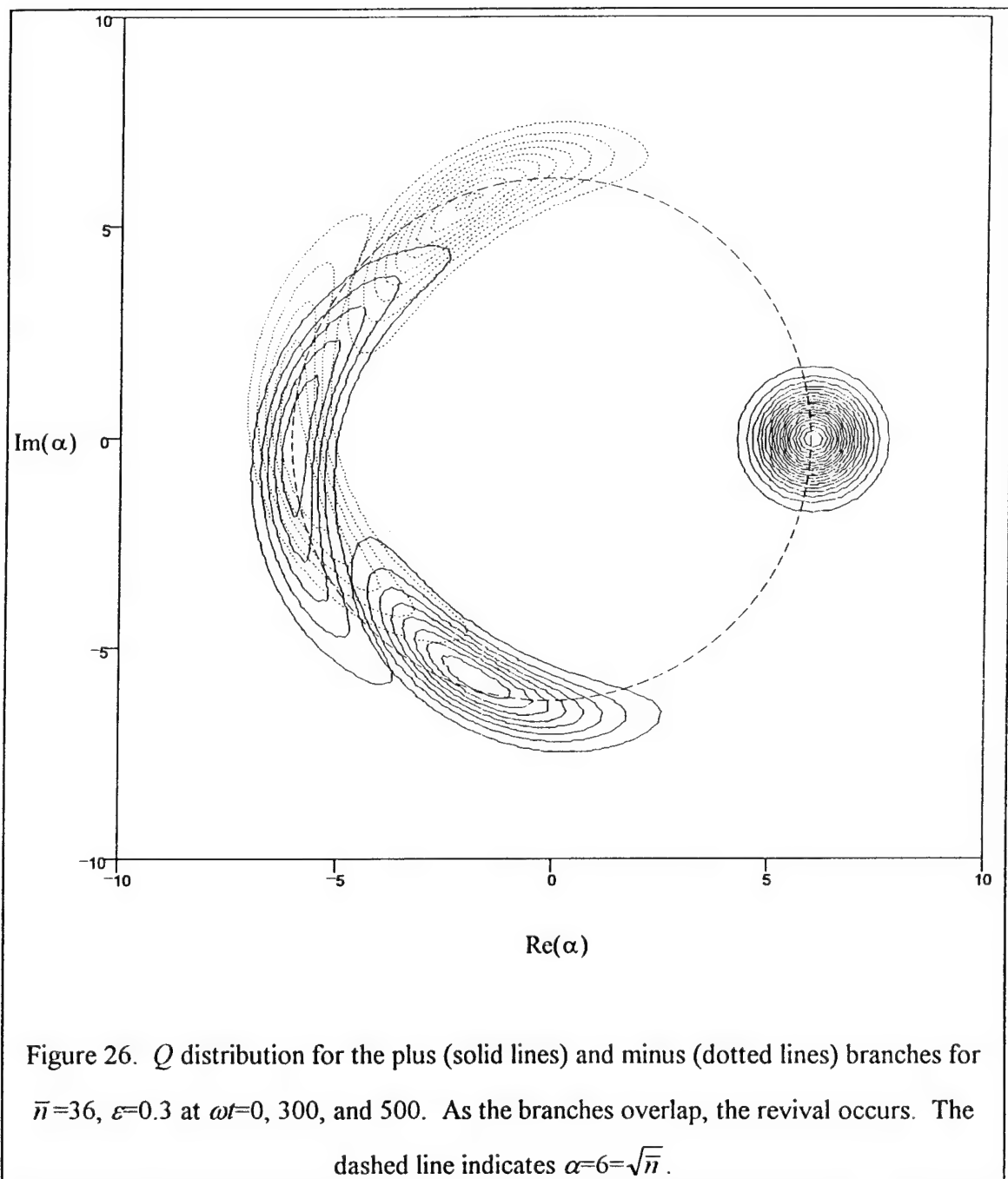


Figure 25. Interference terms contributing to atomic inversion (see text). The large oscillations near $t=500$ mark a revival.



interference terms. The interference contributions can be found by performing three separate numerical integrations of the quantum model. Let $\langle z_+ \rangle$ be the expectation value given by the evolution of $|\psi_+(t)\rangle$, $\langle z_- \rangle$ from $|\psi_-(t)\rangle$, and $\langle z \rangle$ from the linear combination of the two (as already shown in Fig. 24). The interference terms will then be equal to :

$$I = \frac{\langle z_+ \rangle + \langle z_- \rangle}{2} - \langle z \rangle. \quad (3.15)$$

This quantity is plotted in Fig. 25, and the revival of the interference between the two branches is clearly evident, becoming largest very close to $t=500$. Now it is apparent that the results coming from the Floquet eigenstates agree well with the full quantum model.

The indefinite revival demonstrates that the coherent state approximation is beginning to fail for this large time. If the field remained in a coherent state, the revival would last as short a time as the collapse, but Fig. 25 shows that it happens over a substantially longer time. Figure 26 shows how the Q distributions for the plus and minus branches individually evolve. There is little change in the radial profile, indicating the amplitude of the coherent state and its uncertainty do not change much. However, the distribution becomes very elongated, corresponding to an increased uncertainty in the phase. This is suggestive of the squeezing seen in the RWA.⁴⁵ Finally, Fig. 27 shows the evolution of the Q distribution for a linear combination of plus and minus branches. Comparison of Figs. 26 and 27 shows the Q distribution for the linear combination evolves very much like the sum of the Q distributions for the two branches, which further reinforces the picture of the quasiclassical states.

An attempt to improve the accuracy of the coherent state approximation at times near the revival time by increasing \bar{n} cannot be successful: the revival time increases linearly with \bar{n} for fixed ε , while the discrepancy with the quasiclassical states (given

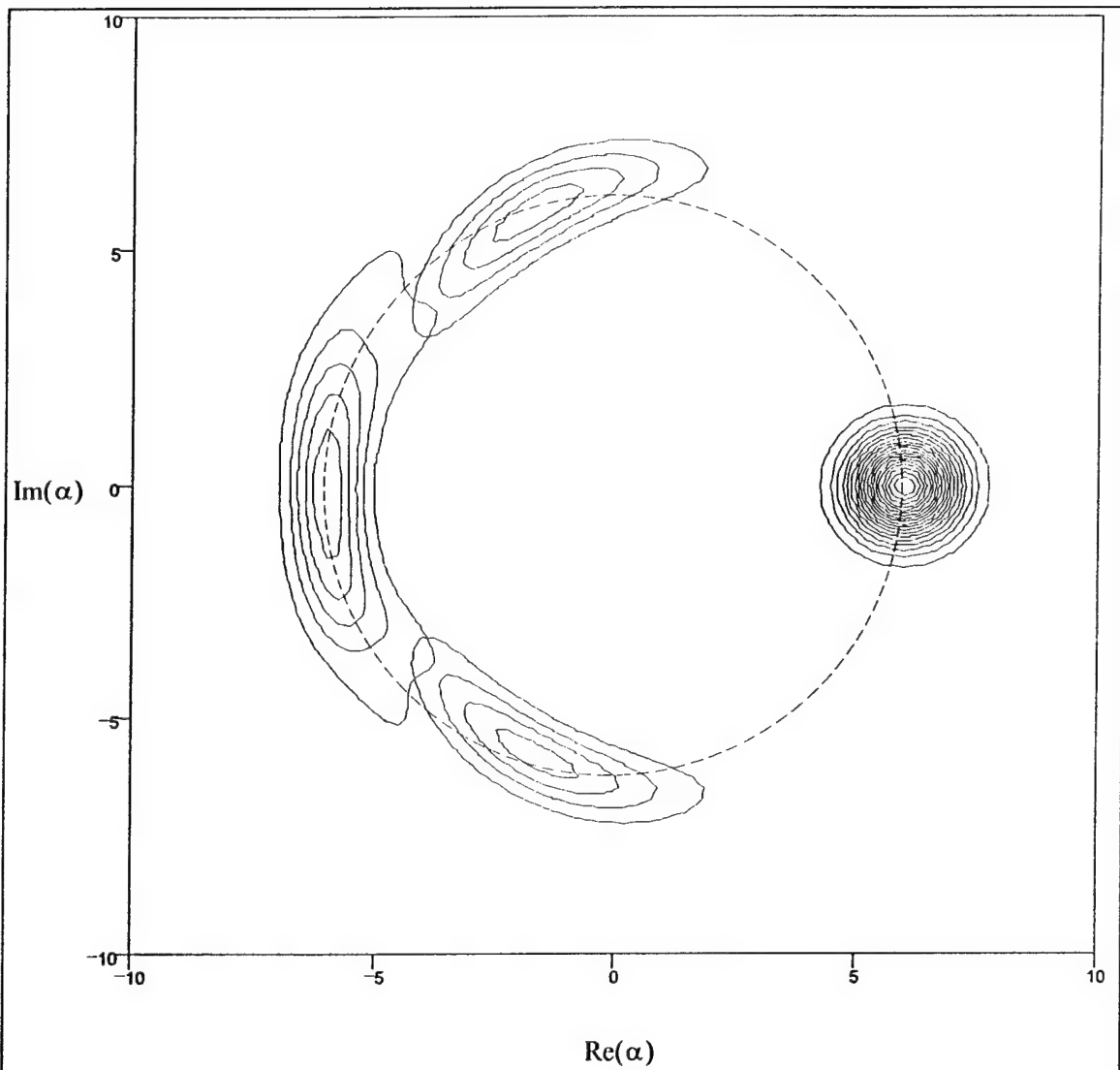


Figure 27. Q distribution for an equally weighted linear combination of plus and minus branches for the same parameters and times as Fig. 26.

by Eq. 3.5) decreases only as $1/\sqrt{n}$. Although the discrepancy given by Eq. 3.5 is not necessarily directly connected to the failure of the coherent state approximation, it gives an upper bound to the agreement which can be expected between the quasiclassical states and the full quantum model.

Having considered some of the limitations of the use of the quasiclassical states, now let us explore a concrete example of their use. For simplicity, consider the small ε limit, so that the series expansion of A 's, B 's, and probability amplitudes (all given in Ref. 38) can be truncated to first order in ε . A particularly useful state for consideration is the upper atomic energy eigenstate, $|a\rangle$. It has been widely used as an initial condition by various authors, and the factorization approximation used to develop the semiclassical model fails dramatically from this state, as already seen. Following Ref. 38, the state $|a\rangle$ is formed by the linear combination

$$|a\rangle = \frac{1}{\sqrt{2}} \left(1 - \frac{\varepsilon}{2}\right) |\psi_+(0)\rangle + \frac{1}{\sqrt{2}} \left(1 + \frac{\varepsilon}{2}\right) |\psi_-(0)\rangle. \quad (3.16)$$

Now use the probability amplitudes in Eq. 3.16, along with Eq. 1.3 for the plus and minus branches, to form

$$\begin{aligned} |\Psi(t)\rangle &= \frac{1}{\sqrt{2}} \left(1 - \frac{\varepsilon}{2}\right) |\psi_+(t)\rangle |\Phi_+(t)\rangle + \frac{1}{\sqrt{2}} \left(1 + \frac{\varepsilon}{2}\right) |\psi_-(t)\rangle |\Phi_-(t)\rangle \\ &= \frac{1}{2} \left\{ \left(1 - \varepsilon e^{i2\omega_+ t}\right) |a\rangle + \left[(1 - \varepsilon) e^{i\omega_+ t} + \varepsilon e^{-i\omega_+ t}\right] |b\rangle \right\} e^{-igt\sqrt{n} - i\omega_+ t/2} |\Phi_+(t)\rangle \\ &\quad + \frac{1}{2} \left\{ \left(e^{-i\omega_- t} + \varepsilon e^{i\omega_- t}\right) |a\rangle + \left[1 + \varepsilon - \varepsilon e^{-i2\omega_- t}\right] |b\rangle \right\} e^{igt\sqrt{n} + i\omega_- t/2} |\Phi_-(t)\rangle, \end{aligned} \quad (3.17)$$

with ω_{\pm} the detuned frequency for the appropriate branch, which is

$$\omega_{\pm} \equiv \omega \pm \frac{g}{2\sqrt{n}} = \omega \pm \frac{\varepsilon}{n}$$

to first order in ε . Although the form of $|\Phi_{\pm}(t)\rangle$ is somewhat complicated, for times smaller than the revival time and ε/n sufficiently small, it simplifies to the following product of coherent state and phase factor

$$|\Phi_{\pm}\rangle \cong e^{\pm i g t \sqrt{n}/2} \left| \sqrt{n} e^{\mp i \omega_{\pm} t} \right\rangle. \quad (3.18)$$

Typically plots of the inversion, $z(t)$, are shown in the literature. To obtain $z(t)$, take the expectation value of σ_z for the state $|\Psi(t)\rangle$. Making these substitutions and performing straightforward algebraic manipulation yields for the inversion when starting from the state $|a\rangle$

$$z(t) \equiv \left[\cos(2g\sqrt{\bar{n}}t) - 2\varepsilon \sin(2\omega t) \sin(2g\sqrt{\bar{n}}t) \right] e^{-g^2 t^2 / 2} + 2\varepsilon \sin(2\omega t) \sin\left(\frac{gt}{\sqrt{\bar{n}}}\right) \quad (3.19a)$$

or, using the scaled time with $\omega=1$,

$$z(t) \equiv \left[\cos(4\varepsilon t) - 2\varepsilon \sin(2t) \sin(4\varepsilon t) \right] e^{-2\varepsilon^2 t^2 / \bar{n}} + 2\varepsilon \sin(2t) \sin\left(\frac{2\varepsilon t}{\bar{n}}\right) \quad (3.19b)$$

The first form shows that as $\varepsilon \rightarrow 0$, the RWA result emerges: Rabi oscillations at frequency $2g\sqrt{\bar{n}}$ modulated by a Gaussian collapse envelope. The second form is useful to see how the various quantities scale with fixed ε as \bar{n} is varied. In either equation, the interference between the two branches is responsible for the terms in square brackets (which vanish after the collapse time). This result does not show any revivals because of the approximations made in obtaining Eq. 3.18. However, it does show the zero in the oscillations at one-half the revival time, which can be observed in Fig. 24. A comparison between the results of numerically integrating the full quantum model and Eq. 3.19b is shown in Fig. 28. The trajectories in this figure use the same parameters as in Fig. 18; $\varepsilon=0.141$, $g=0.05$, $\bar{n}=32$. Even for a value of ε this large, the agreement is quite good.

So far in this chapter we have seen how the Floquet eigenstates which come from the Autler-Townes model are connected to quasiclassical states which remain factorizable for long times. We then found that any state could be written as a linear

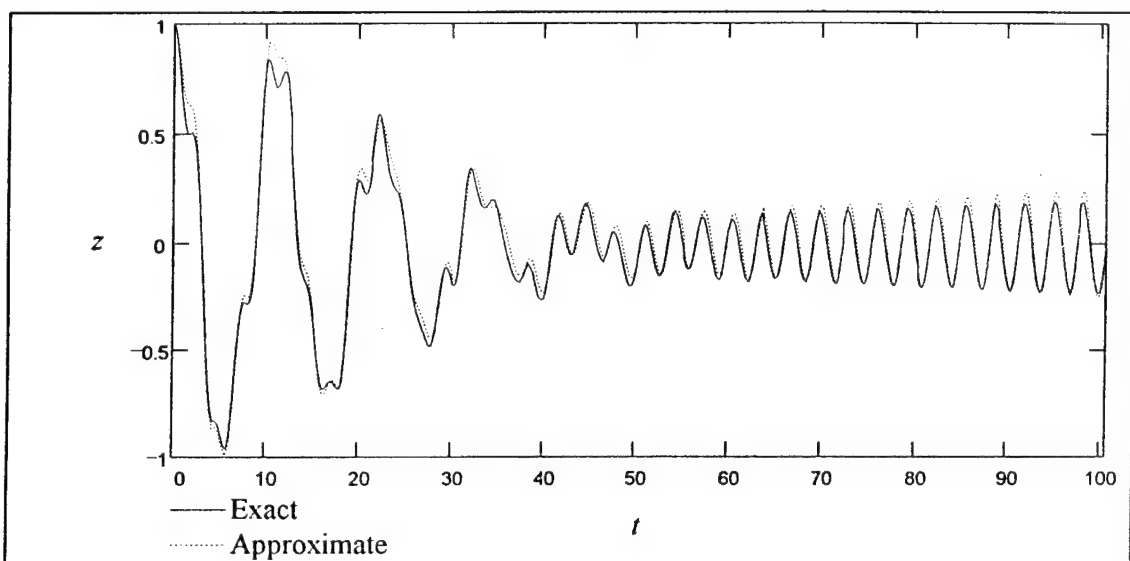


Figure 28. Comparison of population inversion vs. time for exact numerical results and approximation given by Eq. 3.19 for an atom initially in state $|a\rangle$ with parameters given in Fig. 2.18.

combination of the plus and minus branches and its evolution could then be calculated in a straightforward manner for times which approach the revival time. However, there is an additional manner in which these special states can be derived for the quantum system, without any reference to the semiclassical system.

3.3 Quasiclassical States From Eigenvectors of the Hamiltonian

The motivation for finding the quasiclassical states developed from a need to find states which closely matched the evolution of the semiclassical system. However, it is also possible to find such states using an approximate treatment of the eigenvectors of the Hamiltonian in Eq. 1.1. Graham and Höhnerbach published a solution for the eigenvectors to zeroth order and the eigenvalues correct to first order.²⁶ Here we present a similar, though somewhat different technique to obtain the eigenvalues and eigenvectors correct to first order.

The term to be treated perturbatively is the atomic energy. For field states which are built primarily from a limited range of field eigenstates $|n\rangle$, such as coherent states, $a \approx a^\dagger \approx \sqrt{n}$. If the coupling and the average photon number are not too small, such that $g\sqrt{n} > \frac{1}{2}\omega_0$ or $\varepsilon > \frac{1}{4}$, the interaction term will be larger than the atomic energy. Dropping the atomic energy term from Eq. 1.1 we obtain the unperturbed Hamiltonian

$$H_0 = \hbar\omega a^\dagger a + \hbar g \sigma_x (a + a^\dagger). \quad (3.20)$$

Defining the atomic states

$$|\pm x\rangle = \frac{1}{\sqrt{2}}(|a\rangle \pm |b\rangle) \quad (3.21)$$

which are the eigenstates of σ_x with eigenvalue ± 1 (and hence lie at $x=\pm 1$ on the Bloch sphere), we can write for the eigenstates of H_0

$$\begin{aligned} \left[\hbar\omega a^\dagger a + \hbar g \sigma_x (a + a^\dagger) \right] |\pm x\rangle |\Phi_{n\pm}\rangle &= \left[\hbar\omega a^\dagger a \pm \hbar g (a + a^\dagger) \right] |\pm x\rangle |\Phi_{n\pm}\rangle \\ &= E_{n\pm} |\pm x\rangle |\Phi_{n\pm}\rangle \end{aligned} \quad (3.22)$$

with $|\Phi_{n\pm}\rangle$ the field state, which is still to be determined. Now replace a and a^\dagger with new canonical annihilation and creation operators $a' = a \pm g/\omega$ and $a'^\dagger = a^\dagger \pm g/\omega$, with the sign chosen to match the sign of the atomic state. Upon substitution the eigenvalue equation becomes, (after projecting out the atomic part)

$$\left[\hbar\omega a'^\dagger a' - \hbar\omega \left(\frac{g}{\omega} \right)^2 \right] |\Phi_{n\pm}\rangle = E_{n\pm} |\Phi_{n\pm}\rangle. \quad (3.23)$$

Another way to write the new annihilation operator is $a'_\pm = D^\dagger(\pm g/\omega) a D(\pm g/\omega)$, where $D(\alpha)$ is the displacement operator which generates the coherent state $|\alpha\rangle$ when applied to the vacuum state. Using this definition, Eq. 3.23 can be written

$$\left[\hbar\omega D^\dagger\left(\pm \frac{g}{\omega}\right) a'_\pm a'_\pm D\left(\pm \frac{g}{\omega}\right) - \hbar\omega \left(\frac{g}{\omega} \right)^2 \right] |\Phi_{n\pm}\rangle = E_{n\pm} |\Phi_{n\pm}\rangle \quad (3.24)$$

Now the eigenstates can be determined by inspection. If $|n\rangle$ is a number state, then

$$|\Psi_{n\pm}\rangle = |\pm x\rangle \otimes D^\dagger\left(\pm \frac{g}{\omega}\right) |n\rangle \quad (3.25)$$

along with the corresponding eigenvalues

$$E_{n\pm} = n\hbar\omega - \hbar\omega \left(\frac{g}{\omega} \right)^2 \quad (3.26)$$

which are doubly degenerate, since they are independent of the sign of the state. First order degenerate perturbation theory requires that we calculate the matrix elements of the perturbation within each degenerate subspace. Diagonalization of the resulting matrix yields the zeroth order eigenvectors and the first order correction to the eigenvalues.⁴⁷ In this instance,

$$H'_n = \frac{\hbar\omega}{2} \begin{pmatrix} \langle +x|\sigma_z|+x\rangle & \langle +x|\sigma_z|-x\rangle \langle n|D\left(\frac{g}{\omega}\right)D^\dagger\left(-\frac{g}{\omega}\right)|n\rangle \\ \langle -x|\sigma_z|+x\rangle \langle n|D\left(-\frac{g}{\omega}\right)D^\dagger\left(\frac{g}{\omega}\right)|n\rangle & \langle -x|\sigma_z|-x\rangle \end{pmatrix} \quad (3.27)$$

Using Eq. 3.21, it is straightforward to evaluate the atomic state matrix elements. The diagonal elements are both zero, and the atomic part of the off-diagonal elements is equal to 1. The field part is more difficult, but de Oliveira, *et al.*, have reported thoroughly on the displaced number states.⁴⁸ The form of the displacement operator $D(\alpha)=\exp(\alpha a^\dagger-\alpha^* a)$ immediately shows that $D^\dagger(\alpha)=D(-\alpha)$. From Ref. 48, then, we obtain

$$\langle n|D^\dagger\left(\frac{2g}{\omega}\right)|n\rangle = e^{-2\left(\frac{g}{\omega}\right)^2} L_n\left(4\left(\frac{g}{\omega}\right)^2\right), \quad (3.28)$$

where L_n are the Laguerre polynomials. Since this quantity is real valued, the matrix elements are equal. The eigenvalues correct to first order are then

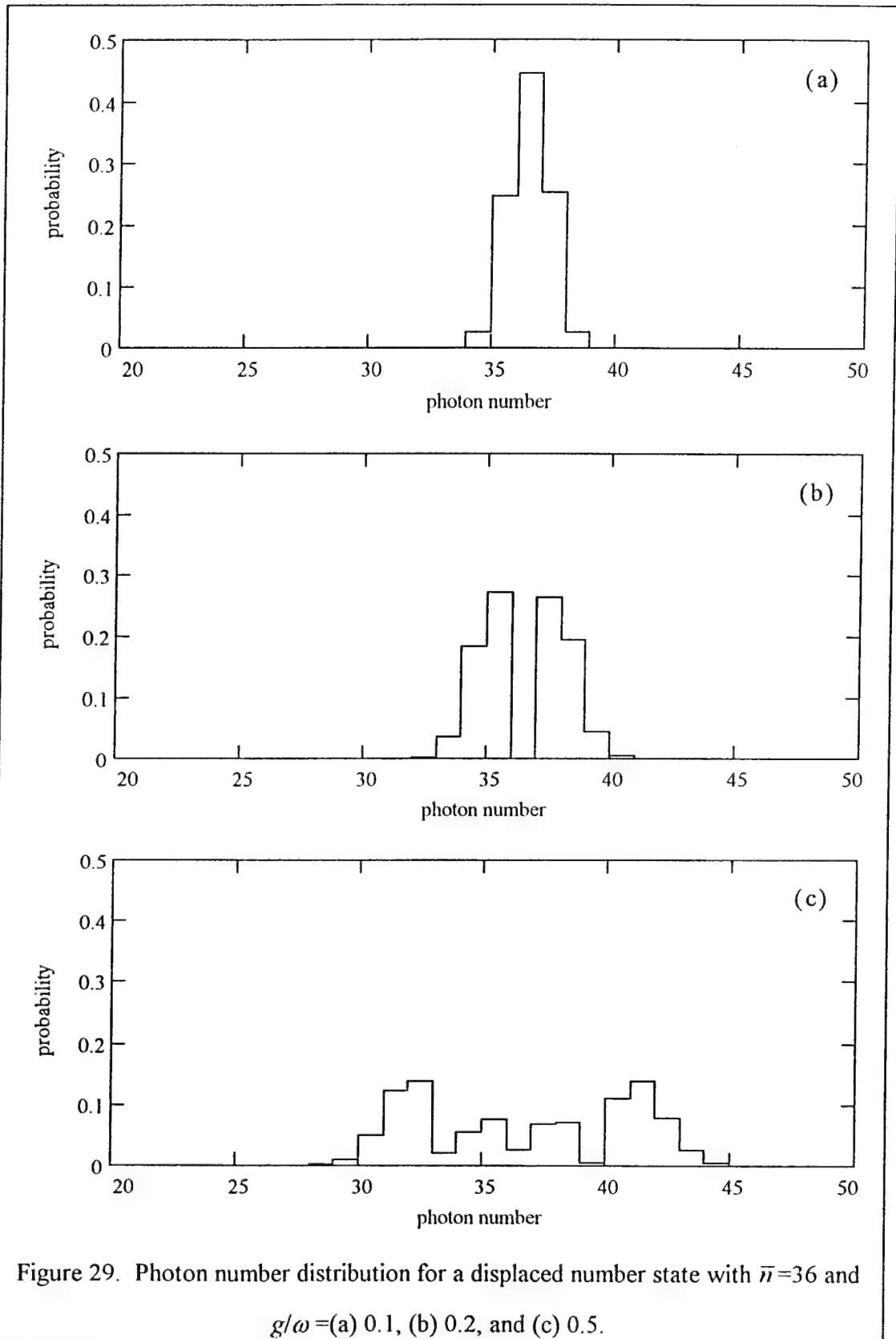
$$E_{n\pm} = \hbar\omega \left[n - \left(\frac{g}{\omega}\right)^2 \pm \frac{1}{2} e^{-2\left(\frac{g}{\omega}\right)^2} L_n\left(4\left(\frac{g}{\omega}\right)^2\right) \right] \quad (3.29)$$

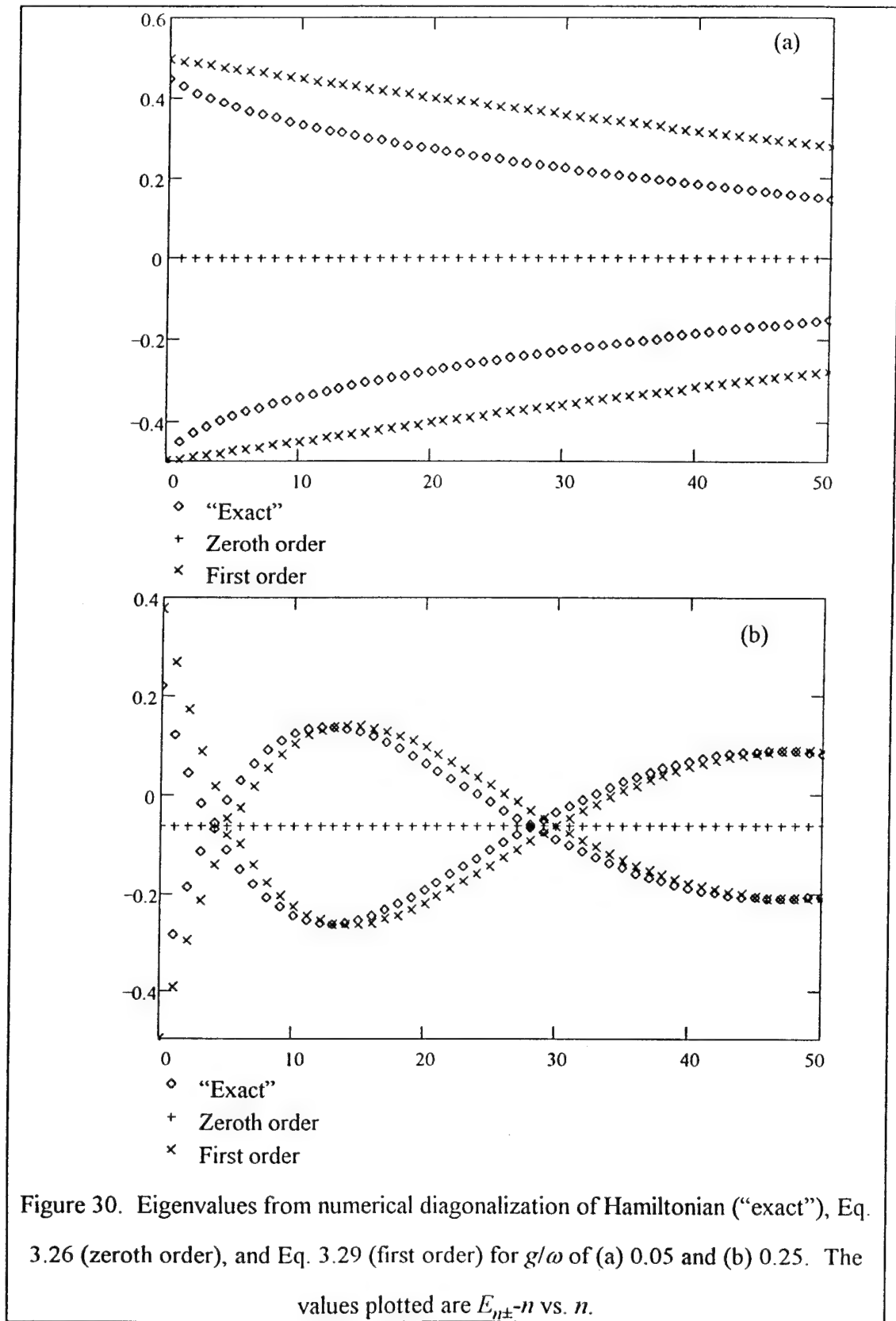
and the zeroth order eigenvectors are

$$|\Psi_{n\pm}^{(0)}\rangle = \frac{1}{\sqrt{2}} \left[| +x\rangle \otimes D^\dagger\left(\frac{g}{\omega}\right)|n\rangle \pm | -x\rangle \otimes D^\dagger\left(-\frac{g}{\omega}\right)|n\rangle \right]. \quad (3.30)$$

One may wonder what a displaced number state looks like. Reference 48 focuses on states with a large displacement and small photon number, while the opposite is needed here. Briefly, for large n and fairly small g/ω , the photon number probability distribution is narrow and centered near n . As g/ω increases, oscillations in the distribution develop and it becomes wider, as demonstrated in Fig. 29. Analytically, the average photon number is

$$\langle n \rangle = n + \left(\frac{g}{\omega}\right)^2 \quad (3.31)$$





and the uncertainty in the average photon number is

$$\langle (\Delta n)^2 \rangle = (2n+1) \left(\frac{g}{\omega} \right)^2. \quad (3.32)$$

Figure 30 compares the zeroth and first order eigenvalues to the results obtained by numerical diagonalization for two different values of g/ω , 0.05 and 0.25. To facilitate comparison, the values actually plotted are $E_{n\pm} - n$. As one would expect from the perturbative calculation, the agreement improves for larger n and g , as $\hbar\omega_0/2$ becomes less significant compared to the other terms in H . In addition, note how the eigenvalues naturally form two sets which are almost smooth functions of n . These two sets are the eigenvalues corresponding (in the appropriate limit) to the \pm signs in Eq. 3.29.

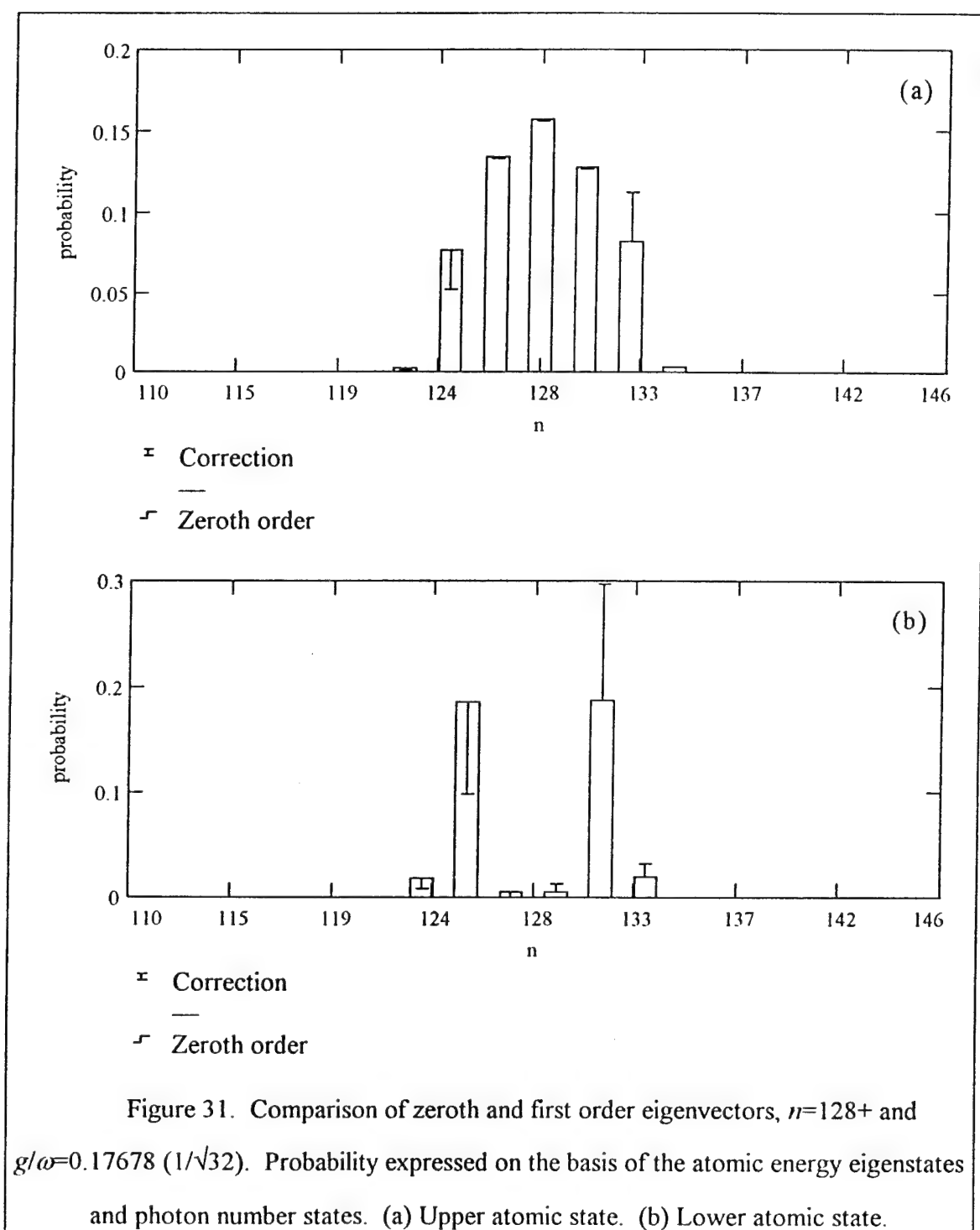
The standard result for first order correction to the eigenvectors is, in the notation used here,

$$|\Psi_{n\pm}^{(1)}\rangle = \sum_{\substack{m \neq n \\ r=\pm}} |\Psi_{mr}^{(0)}\rangle \frac{\langle \Psi_{mr}^{(0)} | H' | \Psi_{n\pm}^{(0)} \rangle}{E_n^{(0)} - E_m^{(0)}} \quad (3.33)$$

Using the properties of the displaced number states and a substantial amount of algebra, we obtain the first order correction

$$|\Psi_{n\pm}^{(1)}\rangle = \pm \frac{e^{-2g^2/\omega^2}}{4} \left\{ \sum_{\substack{m < n \\ r=\pm}} |\Psi_{mr}^{(0)}\rangle \sqrt{\frac{m!}{n!}} \left(\frac{2g}{\omega} \right)^{n-m} L_m^{(n-m)} \left(\frac{4g^2}{\omega^2} \right) (-1)^{n-m} \frac{1 \pm r(-1)^{n-m}}{n-m} \right. \\ \left. + \sum_{\substack{m > n \\ r=\pm}} |\Psi_{mr}^{(0)}\rangle \sqrt{\frac{n!}{m!}} \left(\frac{2g}{\omega} \right)^{m-n} L_n^{(m-n)} \left(\frac{4g^2}{\omega^2} \right) (-1)^{n-m} \frac{1 \pm r(-1)^{n-m}}{n-m} \right\} \quad (3.34)$$

The factorials keep the distribution narrow, and the amplitudes are somewhat symmetrical about the unperturbed state. To use these states in calculation, the zeroth order eigenstates should be expressed in terms of the atomic eigenstates and photon number states. Although not conceptually difficult, the calculation is cumbersome and the final outcome not particularly informative, so it will not be included. However, the



results are shown in Fig. 31, where the probabilities for the state $|\alpha, n\rangle$ and $|b, n\rangle$ (i.e., the atomic energy eigenstate and photon number state) are shown. The calculations for this figure are based on eigenstate $|\Psi_{128+}\rangle$, with $g/\omega=0.17678$.

Let us now return to the goal at hand, which was to find the approximately factorizable states using the eigenstates of H . Suppose we consider the outer product of an atomic state given by the polar angle θ in the Bloch sphere (let the azimuth angle be zero) and a coherent state with amplitude $\alpha = \sqrt{n}$, which shall be denoted $|\theta, \sqrt{n}\rangle$. In general, this state will be described by a distribution of eigenstates with both positive and negative parity. The parity operator of Ref. 26,

$$P = e^{i\pi\left(a^\dagger a + \frac{\sigma_z}{2} + \frac{1}{2}\right)} \quad (3.35)$$

is easily seen to have as eigenvectors the zeroth order eigenvectors of the unperturbed Hamiltonian (3.20). Furthermore, P commutes with the transformed Hamiltonian

$$H = \hbar\omega\left[a'^\dagger a' + \frac{1}{2}\sigma_z - (g/\omega)^2\right]. \quad (3.36)$$

The eigenvalues of like parity depend approximately linearly upon n over a restricted range of n (such as used to build a coherent state) as shown in Fig 30. The state $|\theta, \sqrt{n}\rangle$ is composed of a superposition of eigenstates, which will have time dependence

$$|\Psi(t)\rangle = \sum_{\substack{n \\ \pm}} C_{n\pm} e^{-iE_{n\pm}t/\hbar} |\Psi_{n\pm}\rangle. \quad (3.37)$$

This can be expressed as

$$|\Psi(t)\rangle = e^{iE_{n+}t/\hbar} \sum_n C_{n+} e^{-i(E_{n+} - E_{n+})t/\hbar} |\Psi_{n+}\rangle + e^{iE_{n-}t/\hbar} \sum_n C_{n-} e^{-i(E_{n-} - E_{n-})t/\hbar} |\Psi_{n-}\rangle. \quad (3.38)$$

Suppose the initial state has been chosen so that the C_{n-} coefficients are small and can be neglected. Now by expanding E_{n+} as a Taylor series about $n=\bar{n}$, to the extent that E_{n+} depends linearly on n , we can write

$$|\Psi(t)\rangle = e^{iE_{n+}t/\hbar} \left\{ \sum_n C_{n+} \exp \left[-\frac{i}{\hbar} \frac{\partial E_{n+}}{\partial t} \bigg|_{n=\bar{n}} (n-\bar{n})t \right] |\Psi_{n+}\rangle \right\} \quad (3.39)$$

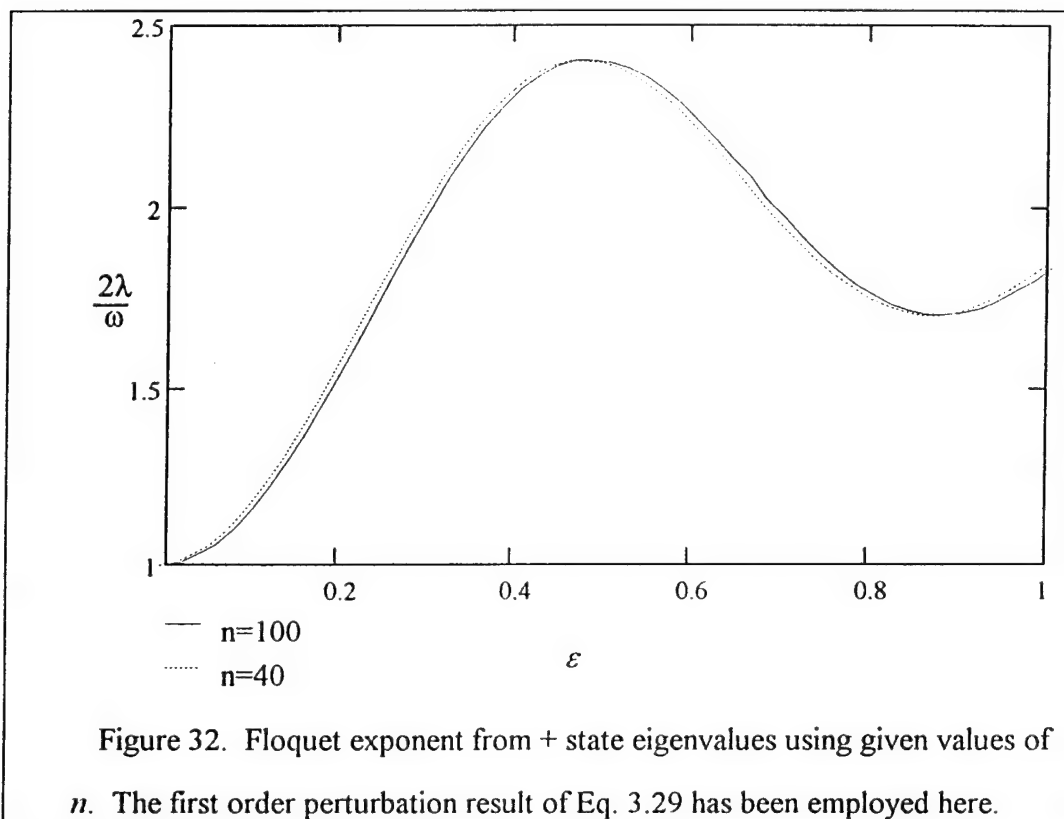
This result is similar in form to the Floquet state (3.2), with $\hbar\omega' = \frac{\partial E_{n+}}{\partial t} \bigg|_{n=\bar{n}}$. Of course, multiples of ω' can be shifted from the Floquet exponent to within the summation without effect in order to place the Floquet exponent in the desired range. It is important that the C_{n-} coefficients can be neglected, since in the corresponding summation for the minus states the Floquet exponent and ω' would be different. Compare Fig. 32, which shows the variation in $2\lambda_a/\omega$ using the eigenvalues obtained from the first order perturbation expression given by Eq. 3.29, to Fig. 5. In the quantum case there is a slight dependence upon n , but otherwise the agreement is quite good. Now consider the inner product between the previously mentioned state $|\theta, \sqrt{\bar{n}}\rangle$ and the eigenstate $|\Psi_{\bar{n}-}\rangle$:

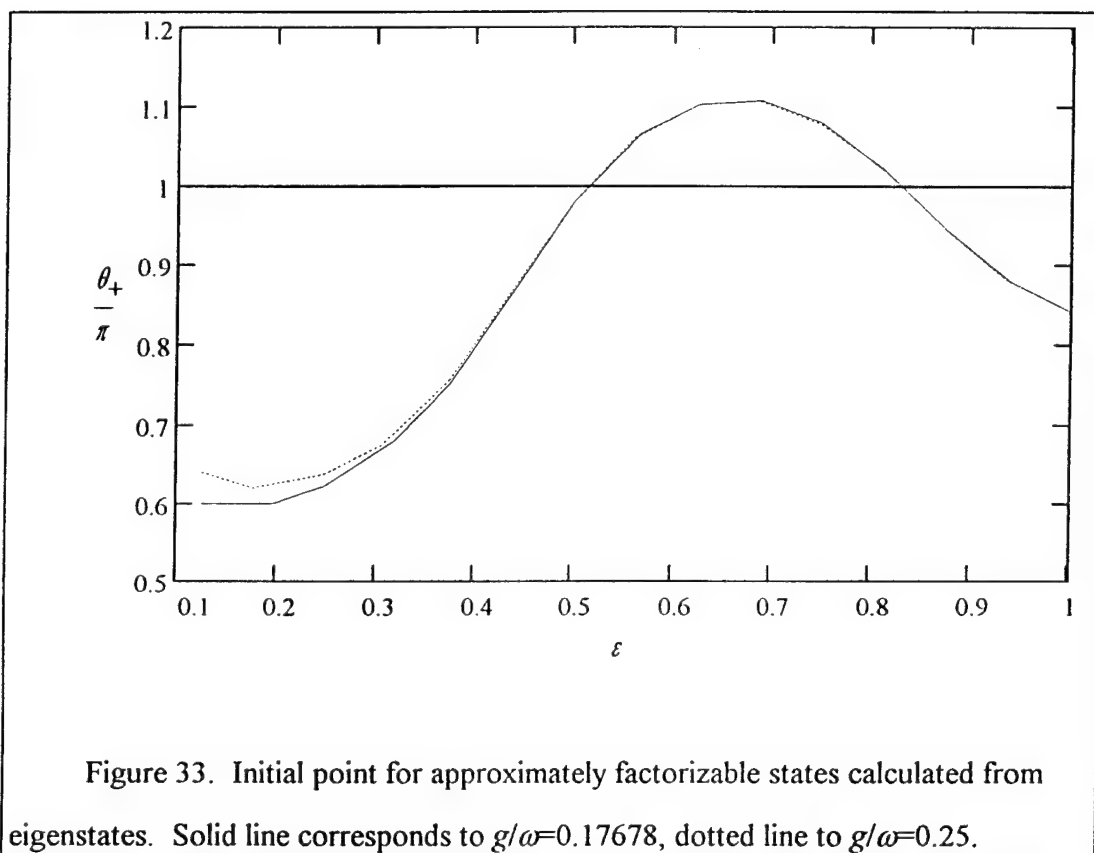
$$\Delta = \left| \langle \Psi_{\bar{n}-} | \theta, \sqrt{\bar{n}} \rangle \right|^2 \quad (3.40)$$

Finding the angle θ which minimizes Δ will produce a state which minimizes the presence of the minus branch (i.e., the C_{n-} 's) and therefore remains approximately factorizable. Figure 33 shows the best value of θ for various values of ε . Two sets of eigenvectors with different values of g/ω were used for the calculation, 0.17678 and 0.25. The agreement with Fig. 7 is striking, with the exception of small ε . With these values of g/ω , the small ε region requires such small values of \bar{n} as to make a quasiclassical approximation invalid. The figure shows the agreement improves with decreasing g/ω .

Of course, some presence of the "wrong" or undesired branch is unavoidable in building a coherent state. However, the choice of θ given above reduces it to a minimum.

We now have found two different techniques, the one just discussed and the use of Floquet eigenstates, which lead to the same quasiclassical states. These states can be combined in a manner which leads to accurate prediction of the full quantum model. Let us now use these results with the understanding of chaos in the semiclassical model gained in Chap. 2 and investigate the impact of semiclassical chaos on the quantum model.





CHAPTER 4

CHAOS AND THE QUANTUM MODEL

Finally we are prepared to discuss the relationship between semiclassical chaos and the behavior of the fully quantized system. Section 1.3 introduced some of the comparisons between semiclassical and quantum models done by other authors. In Sect 4.1 we will focus on a particular approach, examination of purity and uncertainty. This approach has been used extensively by the authors of Ref. 19-21 and we will show some of the pitfalls which may trap the unwary. In addition, some problematic results of Graham and Höhnerbach will be discussed. At last, this work will close with Sec. 4.2, in which the effects of using higher values of angular momentum in the atomic system are considered.

4.1 Impact of Semiclassical Chaos

Grigolini, *et al.* have published a series of papers¹⁹⁻²¹ on investigations of the spin-boson system, both with and without the RWA. Their approach has been to compare the results of the semiclassical model to the quantum model and attempt to find correlations between the onset of chaos and changes in dynamical quantities, much as we will do here. In studying the semiclassical model, they generally have not focused on individual trajectories, but performed averages over an initial distribution which satisfies the quantum uncertainty principle. For the quantum model, they determine the evolution using the Wigner pseudoprobability distribution and Liouvillian operators. They separate the Liouvillian into two parts, L_{cl} and L_{QGD} . L_{cl} yields the same results as the semiclassical model, Eq. 2.4. L_{QGD} (Quantization

Generating Diffusion) is the remainder of the quantum Liouville operator after removing L_{cl} . For comparisons, they take expectation values from the semiclassical distribution and from the corresponding quantum distribution. This is a rather novel approach and holds some promise for understanding the relationship between the two systems, but their work has a few shortcomings which cast doubt on their conclusions. They generally consider evolution of the system from the atom in the lower energy eigenstate, and do not fully account for the effects of the two quasiclassical states (although they do mention one effect, the splitting of the field along the plus and minus branches). Furthermore, they use the RWA results as a basis for comparison, and any departures from the RWA results they attribute to semiclassical chaos. They fail to recognize the importance of initial conditions in the evolution of the quantum system, as we shall see below.

An example will serve to demonstrate the type of problem which can arise if the presence and behavior of the two branches is not recognized. In Ref. 20 they suggest there exists a qualitative difference in the dynamics of the RWA and non-RWA quantum models. They claim this difference leads to a dramatic failure of the RWA while providing good agreement between the quantum and semiclassical non-RWA results. Figure 3 of Ref. 20 plots $z(t)$ for the non-RWA semiclassical model and an approximation they call the Wigner recipe, while in Fig. 4 they do the same for the RWA. Parameters as defined here are $g=0.0898$, $\omega=\omega_0$, $\bar{n}=300$, and $\varepsilon=0.778$, starting from the lower energy eigenstate $|b\rangle$, for a time of $\omega t=16\pi$. The Wigner recipe consists of averaging the results of the numerical integration of the semiclassical equations (2.4) over an initial Wigner distribution for a coherent state, and provides reasonably good agreement with the full quantum model for the calculations shown. In their Fig. 4, the RWA shows a collapse occurring about $t=8\pi$, while the non-RWA quantum calculation shows no collapse and matches the semiclassical model very well.

They attribute this difference to a failure in the RWA. It is more correct, however, to attribute it to comparing two different initial conditions. For the given values of the parameters, $|\psi_+(0)\rangle$ is almost coincident with $|b\rangle$, and so no collapse is expected and the semiclassical model should provide good agreement. However, in the RWA, the state $|b\rangle$ is formed by an equally weighted linear combination of the plus and minus branches, thus the collapse is expected. A more appropriate choice would be to compare the results along the plus branch in both instances, in which case the RWA would show no collapse and give good agreement with the semiclassical model. Alternatively, one could compare the same equally weighted linear combination of plus and minus branches in the non-RWA as used in RWA. The results of this calculation are shown in Fig. 34. It shows a collapse in time of about $t_c=60$, compared to $t_c=58.5$ given by Eq. 3.13. Thus, the main difference between the RWA and non-RWA is the length of t_c , a small difference which is well understood from the material in Chap. 3.

Now let us turn our attention to Ref. 21. In this article they develop the Liouvillian dynamics and separate the effects of classical and quantum components. In addition, they use the semiclassical equations of motion and calculate the Lyapunov exponents using the method of Ref. 37, as was done here. They identify a threshold for chaos in which the largest Lyapunov exponent increases to almost unity from about 0.1. They refer to this region of very large Lyapunov exponent as the chaotic region, ignoring the region with smaller Lyapunov exponents. This is not typical of the work in this field, where, for example, Ref. 15 identifies a region as chaotic for a Lyapunov exponent as small as 0.087. Likewise, the Hénon-Heiles system was considered chaotic by the authors of Ref. 37 with a Lyapunov exponent of approximately 0.08. The threshold Grigolini, *et al.* identified for highly chaotic behavior occurs at resonance with $g=0.5$ and $\bar{n}=5$. Because of the small photon number, their

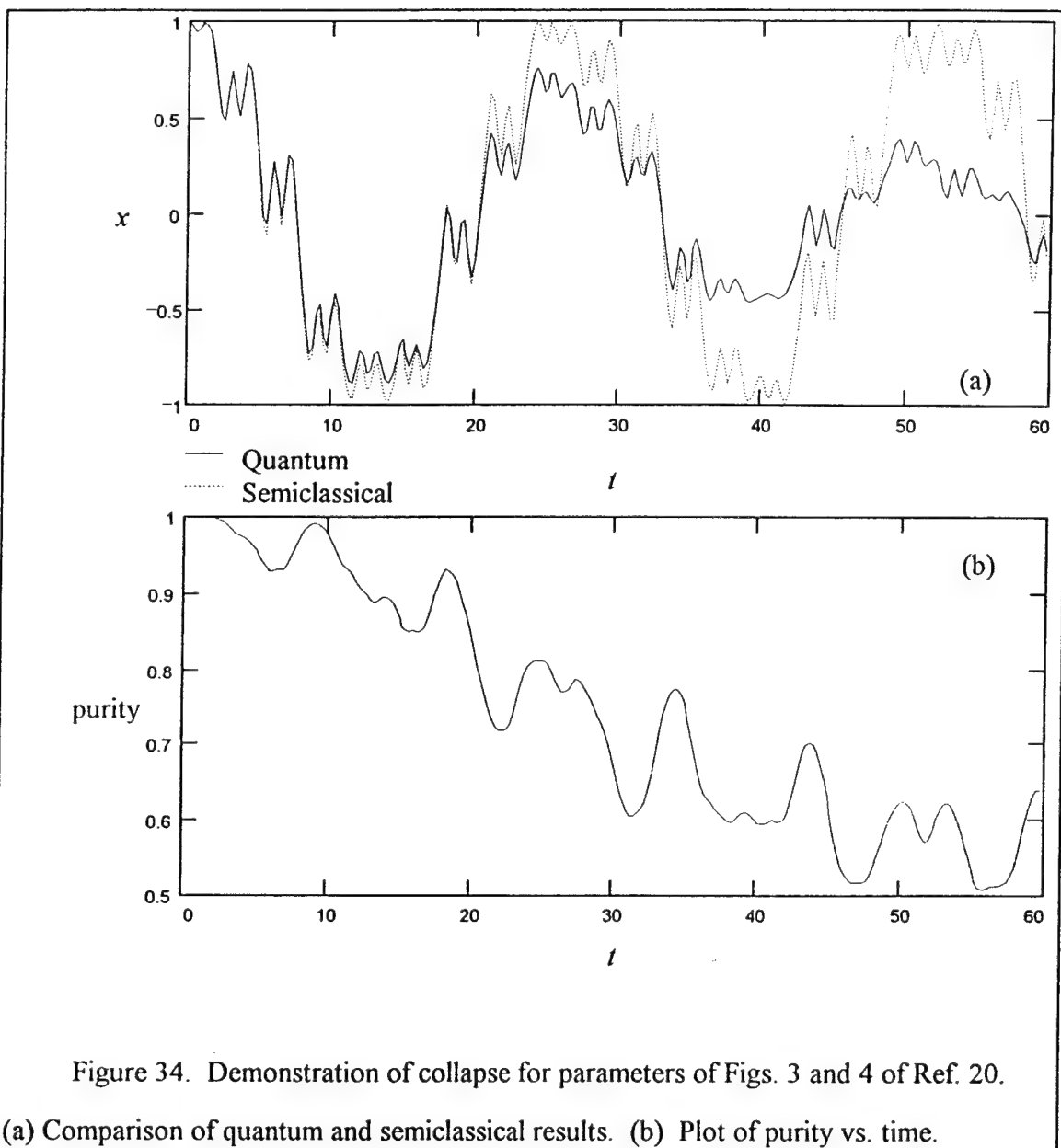


Figure 34. Demonstration of collapse for parameters of Figs. 3 and 4 of Ref. 20.

(a) Comparison of quantum and semiclassical results. (b) Plot of purity vs. time.

conclusions cannot be directly applied to this work, since such a small photon number precludes the quasiclassical approximation from applying. Nonetheless, we will continue and attempt to test the extension of their work into the parameter space applicable here.

As a test for the effect of semiclassical chaos on the quantum system, they use the entropy of the atom. Phoenix and Knight present a method for finding the entropy using ρ_{at} , the atomic reduced density operator.⁴⁹ Given the matrix elements ρ_{aa} , ρ_{ab} , and ρ_{bb} , the eigenvalues of ρ_{at} are

$$\alpha_{\pm} = \frac{1}{2} \left\{ 1 \pm \sqrt{(\rho_{aa} - \rho_{bb})^2 + 4|\rho_{ab}|^2} \right\} \quad (4.1)$$

and the entropy is

$$S(\rho_{at}) = -(\alpha_+ \ln \alpha_+ + \alpha_- \ln \alpha_-). \quad (4.2)$$

Using the expression for the purity

$$P = \rho_{aa}^2 + \rho_{bb}^2 + 2|\rho_{ab}|^2, \quad (4.3)$$

it is straightforward to relate the entropy to the purity:

$$S(P) = -\frac{1}{2} \left(1 + \sqrt{2P-1} \right) \ln \left[\frac{1}{2} \left(1 + \sqrt{2P-1} \right) \right] \\ - \frac{1}{2} \left(1 - \sqrt{2P-1} \right) \ln \left[\frac{1}{2} \left(1 - \sqrt{2P-1} \right) \right]. \quad (4.4)$$

In a non-chaotic region of the parameter space, far off-resonance, Grigolini, *et al.* show that the entropy reaches its maximum value ($\ln 2$) during the collapse region, and returns briefly to zero during revivals. They then claim that for the chaotic system the disappearance of the revivals in the quantum model is a result of the chaos in the semiclassical model. The absence of revivals is undeniable, but to identify semiclassical chaos as the cause is rather speculative, as we will show momentarily.

Let us turn now to Ref. 19, which reviews the material in the previous articles and extends it somewhat. Specifically, they add a discussion of the entropy growth

and irreversibility for an initial photon number (Fock) state and they relate the growth of field uncertainty to semiclassical chaos.

The entropy growth starting from a number state is included in order to compare with results from the RWA. The RWA is manifestly non-chaotic in the semiclassical model, having only two degrees of freedom. In spite of this fact, it shows an overall increase in the entropy with time if the field is initially in a coherent state.⁴⁹ The increase in entropy is attributed in Ref. 19 to the coherent state mimicking a heat bath with an infinite number of degrees of freedom.⁵⁰ The collapses result from the many different frequencies, one for each eigenstate $|\Phi_n\rangle$ of the oscillator. Furthermore, because the frequencies increase as \sqrt{n} , rather than integer n , the revivals are not perfect. To circumvent the irreversibility and consequent increase in entropy from starting with a coherent state, in Ref. 19 they calculate the entropy with the field starting in a number state. In the RWA, if the field begins in a number state the system evolves reversibly, while in the non-RWA it does not. In Ref. 19, Fig. 3 uses the atomic entropy to show the increasing irreversibility for five different values of g , with the field starting in a number state and the atom starting in the lower energy eigenstate. They claim this behavior supports their conclusion that quantum irreversibility is a signature of semiclassical chaos. However, the difference between the behavior in the RWA and non-RWA can better be attributed to differences in the eigenstates of the RWA and non-RWA Hamiltonians. The eigenstates of the RWA Hamiltonian can be written

$$|\Psi_{n\pm}^{RWA}\rangle = \frac{1}{\sqrt{2}}(|a\rangle|n\rangle \pm |b\rangle|n+1\rangle). \quad (4.5)$$

Thus the atom in the upper state with the field in a number state is just

$$|a\rangle|n\rangle = \frac{1}{\sqrt{2}}(|\Psi_{n+}^{RWA}\rangle + |\Psi_{n-}^{RWA}\rangle). \quad (4.6)$$

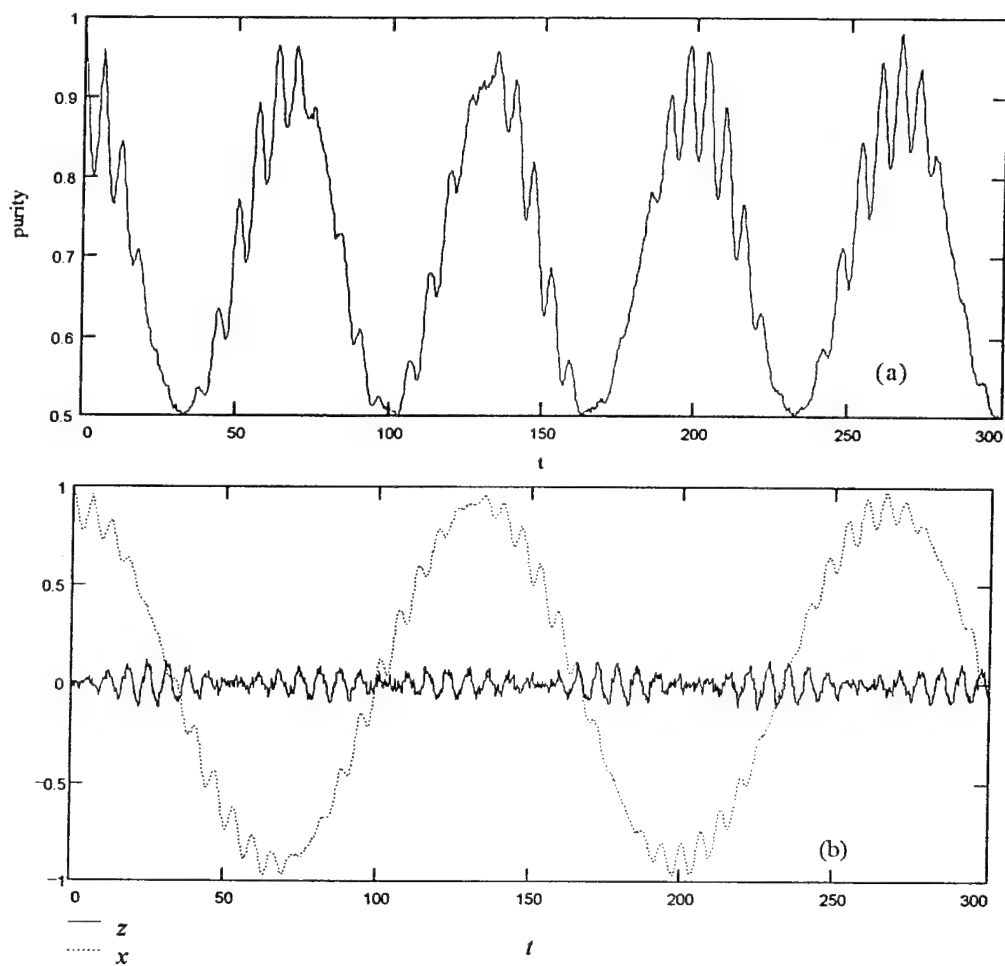


Figure 35. Reversible evolution in non-RWA for parameters of Ref. 19 with field in a displaced number state. (a) Purity vs. time. (b) Atomic expectation values $z(t)$ and $x(t)$.

As shown above in Sec. 3.3, the eigenstates of the non-RWA are approximately

$$|\Psi_{n\pm}^{non-RWA}\rangle \cong \frac{1}{\sqrt{2}} \left(| +x \rangle D^\dagger \left(\frac{g}{\omega} \right) | n \rangle \pm | -x \rangle D^\dagger \left(-\frac{g}{\omega} \right) | n \rangle \right). \quad (4.7)$$

The forms of these two sets of states are very similar. Thus, a more appropriate choice for the initial state in the non-RWA (in order to compare to the RWA) would be

$$|\Psi(0)\rangle = | +x \rangle D^\dagger \left(\frac{g}{\omega} \right) | n \rangle, \quad (4.8)$$

which has the evolution shown in Fig. 35. The calculation shown in that figure should be compared to Fig. 3e of Ref. 19, in which $g=0.898$, $\omega=\omega_0$ (resonance), $n=10$, and $\varepsilon=1.420$, and which shows highly irreversible evolution. In contrast, the evolution in Fig. 35 is, to a good approximation, clearly reversible, even when the semiclassical model is strongly chaotic and the approximation leading to Eq. 4.7 is not particularly good. This comparison again demonstrates the importance of choosing appropriate initial conditions when comparing the results from the RWA and non-RWA models.

Now we will examine the quantum uncertainty. In Ref. 19 the quantum uncertainty is defined as

$$U = \Delta a_1 \cdot \Delta a_2. \quad (4.9)$$

In Fig. 4 of that reference, $U(t)$ is shown for five values of $g=\{0.045, 0.090, 0.224, 0.449, 0.898\}$, starting with the field in a coherent state with $\bar{n}=10$ and the atom in the lower eigenstate. They state that these five values of g all correspond to increasing values of the Lyapunov exponent in the semiclassical model, and that figure shows that $U(t)$ increases more rapidly for larger (hence more chaotic) values of g . However, it is difficult to attribute the growth of the uncertainty to semiclassical chaos because the smaller values of g show growth as well as the larger values. For example, their Fig. 4c-e ($g=0.224, 0.449, 0.898$ respectively) yield the same general behavior: rapid

growth in $U(t)$ until it reaches a roughly asymptotic value, which is larger for larger values of g . Curves (c) and (d) exhibit the greatest similarity to each other, having roughly the same slope and asymptotic value. Semiclassically, however, they could not be more different. My calculations show that the Lyapunov exponent for the parameters of curve (c) is converging on zero and is clearly non-chaotic while the parameters of curve (d) give behavior which is clearly chaotic with a Lyapunov exponent of approximately 0.09. The differences in the evolution of these two parameter sets semiclassically and similarities quantum mechanically virtually eliminate semiclassical chaos as the cause of the uncertainty growth.

Grigolini, *et al.* are not alone in mis-attributing any differences observed between the RWA and non-RWA behavior to chaos. In Ref. 27 Graham and Höhnerbach do the same. They claim the disappearance of revivals is a mark of semiclassical chaos, as are changes in the power spectrum of the field. Figure 3 of Ref. 27 shows the occupation probability of the upper state vs. time for a quantum trajectory starting from the state $|a\rangle$ with $g/\omega=0.01$ and $\bar{n}=100$. (The occupation probability of the upper state is simply $(1+z)/2$.) The trajectory shows definite revivals and collapses, similar to Fig. 25. They contrast that to the behavior shown in their Fig. 4, for which $g/\omega=0.075$ and all else is the same. Their Fig. 4 shows no clear revivals, which they claim is the result of semiclassical chaos based on their analytic approximations. Their approximation is based upon studying a quantity, K , formed from a combination of spin and field variables which is conserved in the RWA but not conserved in the non-RWA. Using the counter-rotating terms they calculate an expression for \dot{K} , which they evaluate using results from the RWA. This process leads to a prediction that the entire phase space will be chaotic for the parameters used in their Fig. 4. Unfortunately, these parameters ($g/\omega=0.075$, $\epsilon=0.375$, $\bar{n}=100$) yield trajectories which, according to my calculations, are completely regular, whether

starting from $|a\rangle$ or either of the quasiclassical states. Furthermore, the absence of revivals is not surprising because the given value of ε means the initial state $|a\rangle$ is composed mostly of the minus branch.

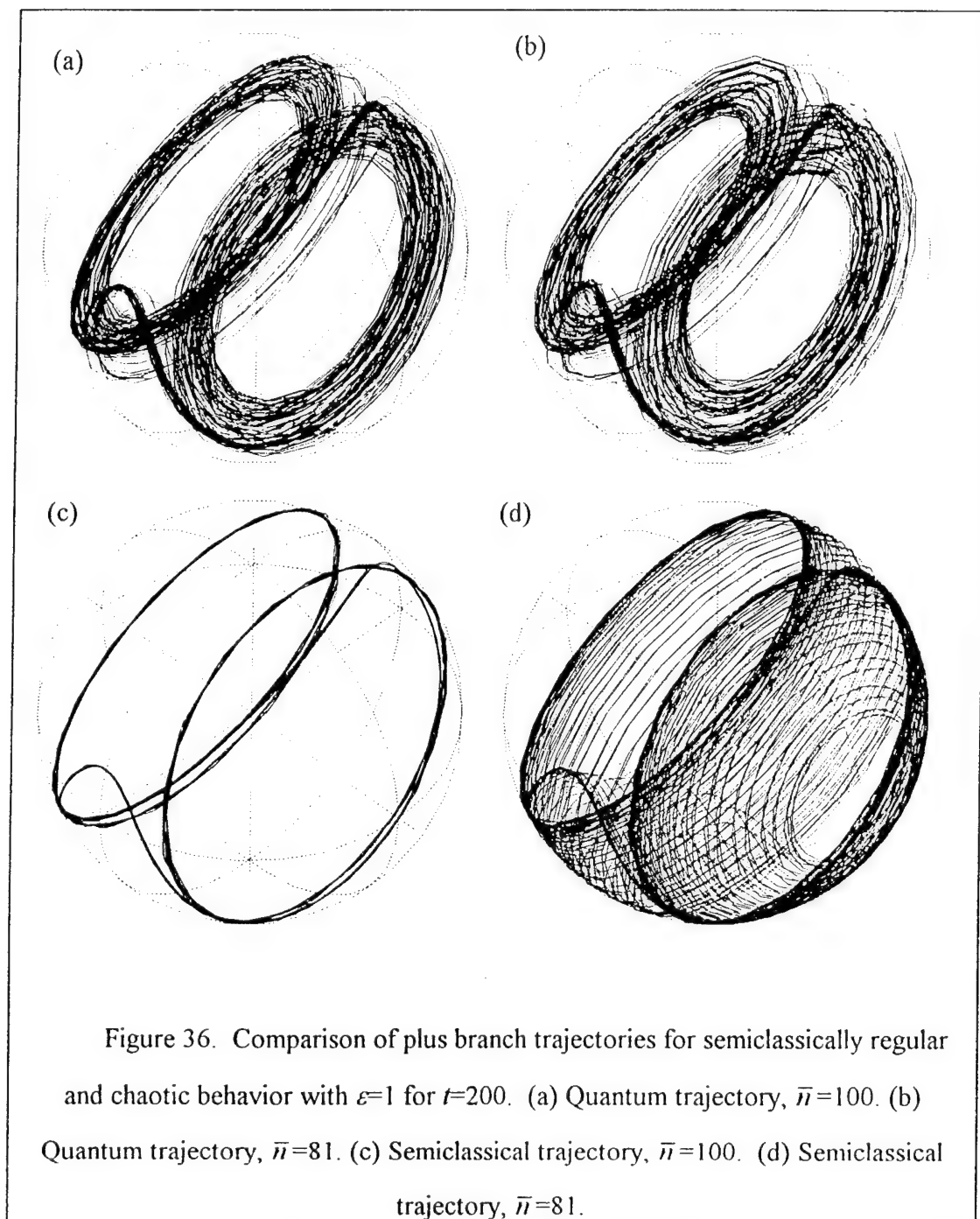
They find an analytical result for the power spectrum in the RWA which predicts two peaks symmetrically displaced from nominal field frequency ω by $\pm g/2\sqrt{\bar{n}}$. These two peaks are, of course, the field corresponding to the plus and minus branches. They then claim the asymmetry due to the dominance of one peak is a signature of semiclassical chaos. Their Fig. 6 is used to support this claim, where they plot the power spectrum for $g/\omega=0.1$, $\varepsilon=0.4$, and $\bar{n}=64$. This plot shows two peaks, the lower frequency peak larger than the other by approximately a factor of $2.9/0.35=8$, each centered at frequencies $\omega \approx 1 \pm 0.002$. Using the Autler Townes model we find the upper atomic state is composed of $|a\rangle \approx 0.30|\psi_+\rangle + 0.95|\psi_-\rangle$. The ratio of the squares of these components yields approximately 9, in reasonable agreement to the ratio of the sizes of the two peaks. Equation 2.14 gives an interaction induced detuning of 0.002ω , again in agreement with their result. And finally, like the previous example from their paper, the semiclassical model is not, based on my calculations, chaotic for this set of parameters. In summary, they have compared their results of quantum calculations using the RWA and non-RWA, attributing differences in these results to the presence of chaos in the semiclassical model. The differences can be better explained as the result of differences in the quasiclassical states between the RWA and non-RWA models.

What then can be said about the correlations between semiclassical chaos and quantum mechanical evolution? The conclusion of the present work is: for the spin $1/2$ system, little or nothing. Recall the marked transition to chaos in the semiclassical model for the plus branch near $\bar{n}=90$ with $\varepsilon=1$. Figure 36 compares the evolution in the Bloch sphere for $\bar{n}=100$ and $\bar{n}=81$. Semiclassically, there is an extensive

difference between the trajectories. The chaotic trajectory covers about two-thirds of the surface of the sphere, while the regular trajectory remains confined to the neighborhood of the Autler-Townes Floquet eigenstate, as discussed in Sec. 2.3. The relevance of the quasiclassical states is apparent, since the quantum trajectories bear a remarkable resemblance to the regular semiclassical trajectory. In addition, the two quantum mechanical trajectories are virtually indistinguishable from each other. Moreover, the similarity between the two trajectories does not stop at the Bloch sphere evolution. Figures 37-39 compare the purity, spectra, and uncertainty product for the two quantum trajectories.

In Fig. 37, one main difference in the purity for the two quantum trajectories can be readily observed. For the trace for $\bar{n}=81$, a few oscillations are visible at the very beginning and again near $t=550$. These correspond to a partial collapse and revival due to the unavoidable presence of some portion of the minus branch field, as discussed in Sec. 3.3. The partial collapse and revival are also visible in the trace for $\bar{n}=100$, but around $t=675$. The ratio of these two times, according to Eq. 3.14, should be equal to the ratio of \bar{n} for each trajectory. In fact, the ratio is approximately 0.814, in agreement with the predicted value of 0.81. However, there are no other significant differences between the trajectories to indicate the semiclassical system has undergone a transition to chaos.

A similar comparison can be made from Fig. 38. The spectra from the quantum trajectories are shown together in Fig. 38a. The major features of each spectrum are identical. The differences in the two spectra at the base of some of the peaks are artifacts of the Fourier transform resulting from the difference in the interaction induced detuning for the two trajectories. On the other hand, Fig. 38b contrasts the two spectra for the semiclassical system. For $\bar{n}=100$ two small peaks can be seen near the odd values of ω , while for $\bar{n}=81$ these are regions of noise. Likewise, the base of



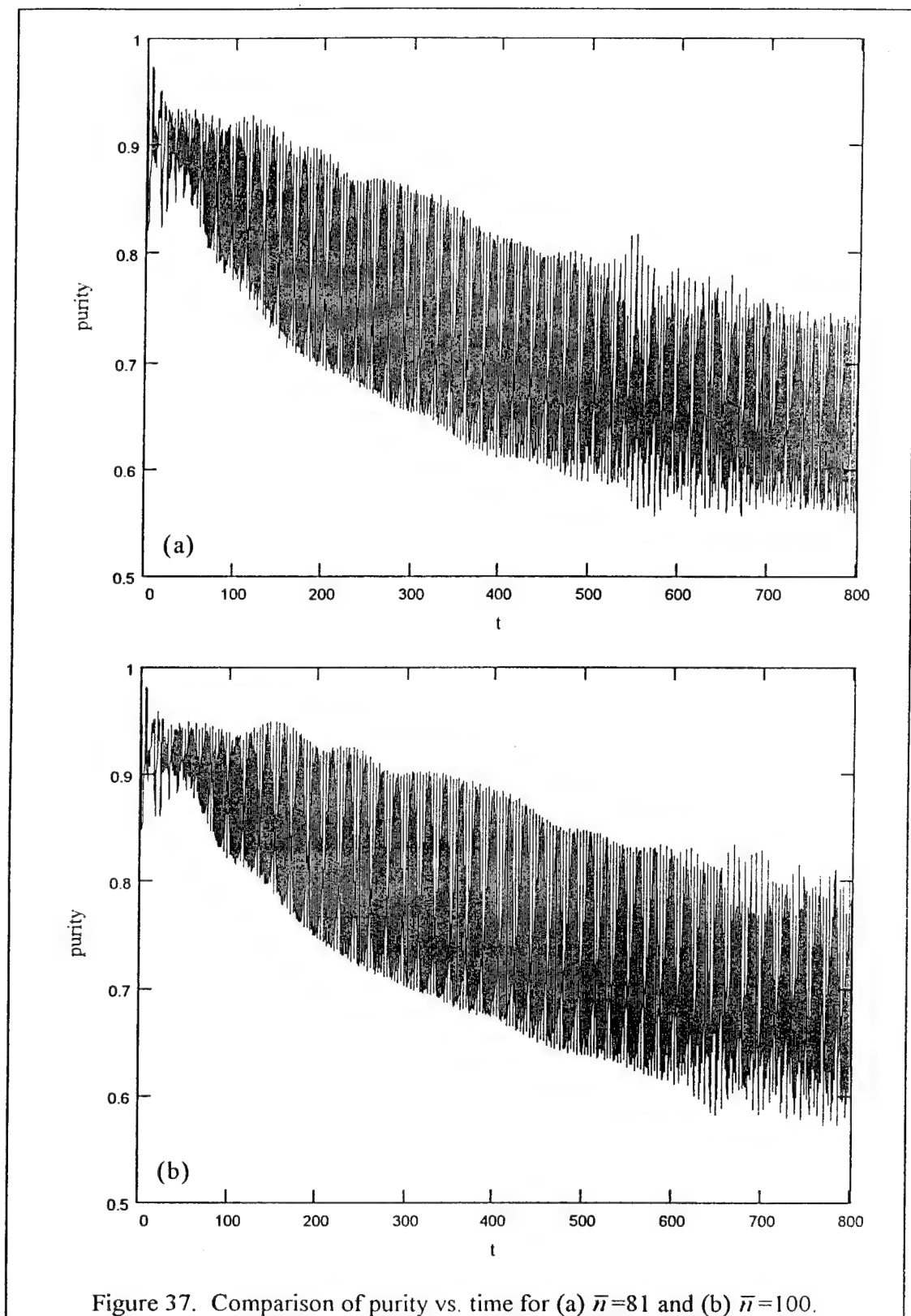
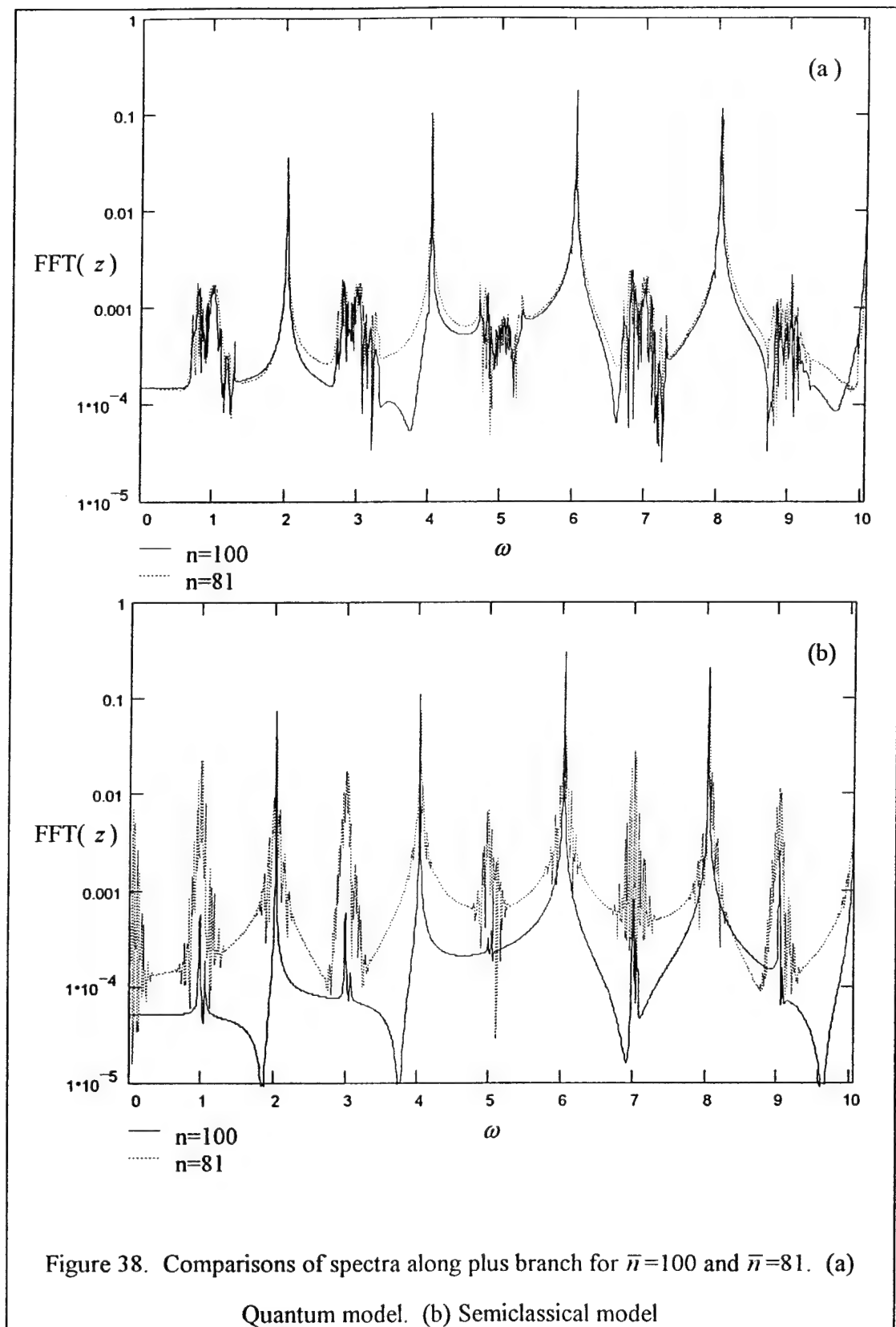
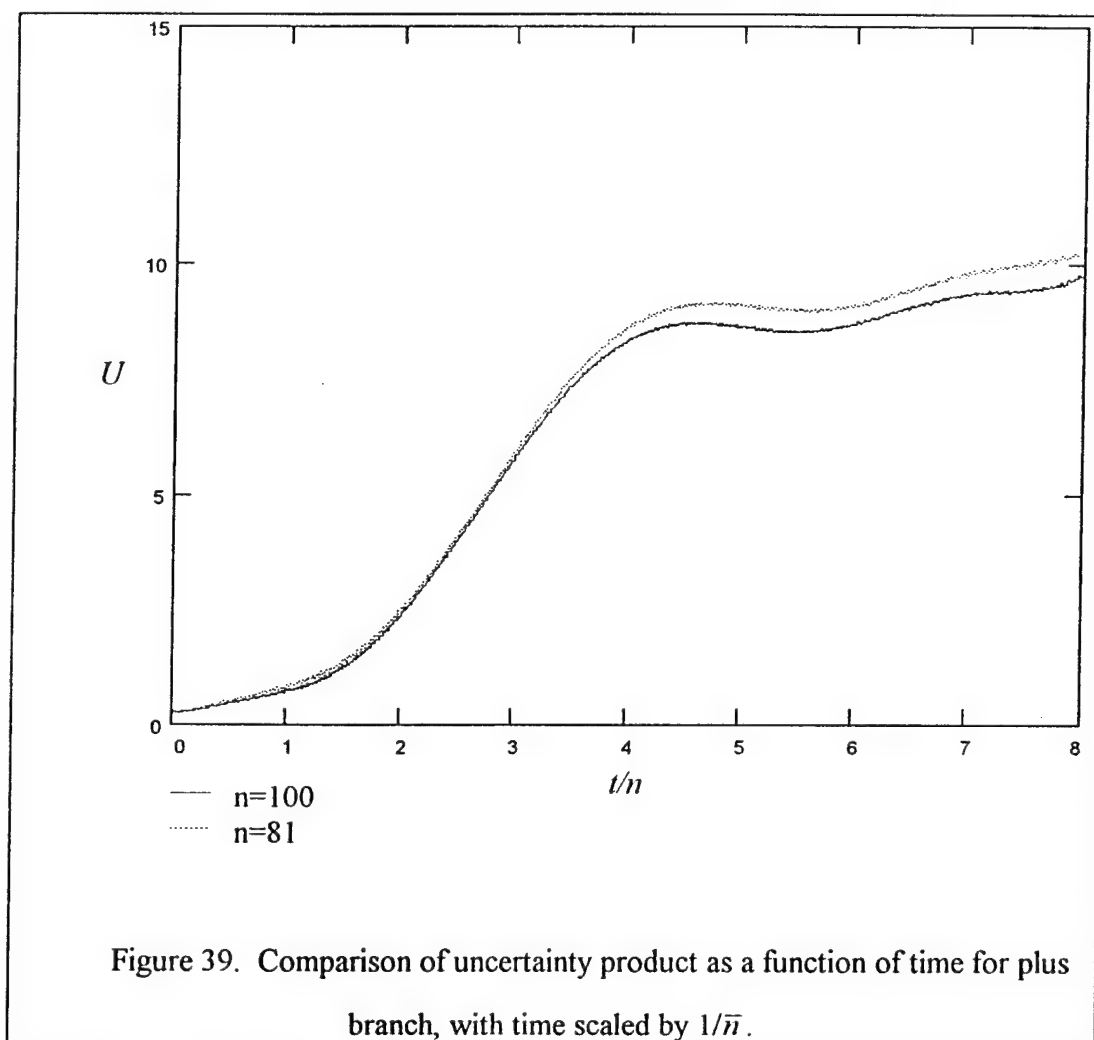


Figure 37. Comparison of purity vs. time for (a) $\bar{n}=81$ and (b) $\bar{n}=100$.



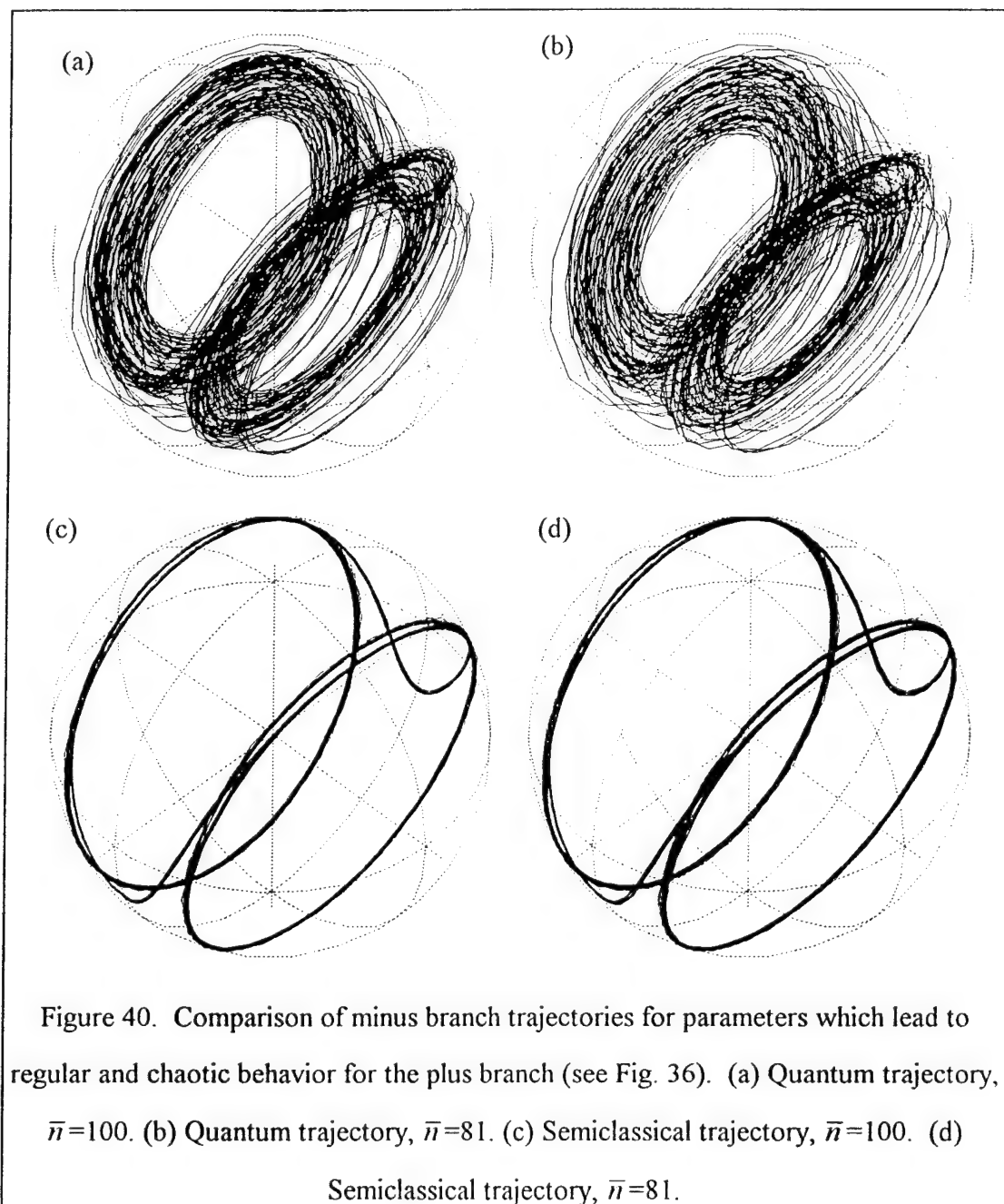


each even value of ω is a region of noise for the chaotic trajectory. The two small peaks in the $\bar{n}=100$ spectrum result from the Autler-Townes model not giving the precise starting point needed for a periodic trajectory in the semiclassical model. By trial and error, though, one can “zero in” on the optimum starting point and make the pair as small as desired. However, trial and error, even to 8 decimal place accuracy, does not get rid of the noise in the chaotic spectrum or provide a stable trajectory.

Finally, Fig. 39 shows the evolution of the quantum uncertainty, U , given by Eq. 4.9. In this figure, U is plotted against a scaled time, t/\bar{n} , in order to suppress the difference in the two trajectories due to the interaction induced detuning. Without the scaling the uncertainty for $\bar{n}=81$ grows somewhat faster than for $\bar{n}=100$. However, the scaling demonstrates that the faster growth is not due to chaos, but to the interaction induced detuning as the field phase uncertainty grows (see Fig. 26). The two trajectories do not significantly differ until about one half of the revival time, when the coherent state approximation begins to fail. Even then, the difference in the two trajectories is small.

To further illustrate the absence of a link between semiclassical chaos and the behavior of the quantum model, consider now the evolution along the minus branch. The next series of figures, Figs. 40-43, starts along the minus branch, which does not display chaos for $\bar{n}>30$. The main differences between these trajectories and those of the previous set of figures are in the semiclassical trajectory for $\bar{n}=81$. Figure 40d shows that the orbit for $\bar{n}=81$ remains stable, while Fig 42b shows that the spectra for $\bar{n}=81$ and $\bar{n}=100$ are virtually identical. The quantum model trajectories differ only slightly along the plus and minus branches. The minus branch trajectories are less pure than their plus branch counterparts, as shown in Fig. 41. In addition, the revivals are even more obscured for the minus branch. These observations run directly counter to the contentions of Grigolini and Graham, since the minus branch is not chaotic.

Likewise, Fig. 43 shows that the uncertainty product for the minus branch trajectories is higher than the uncertainty product for the plus branch trajectories. Although it is notable that the uncertainty products are closer in value for the two minus branch trajectories, the larger value for the minus branch shows there is no correlation with the chaotic behavior of the semiclassical model. These examples demonstrate the absence of a direct correlation between semiclassical chaos and the behavior—whether measured by purity, entropy, spectrum, or uncertainty—of the quantum model.



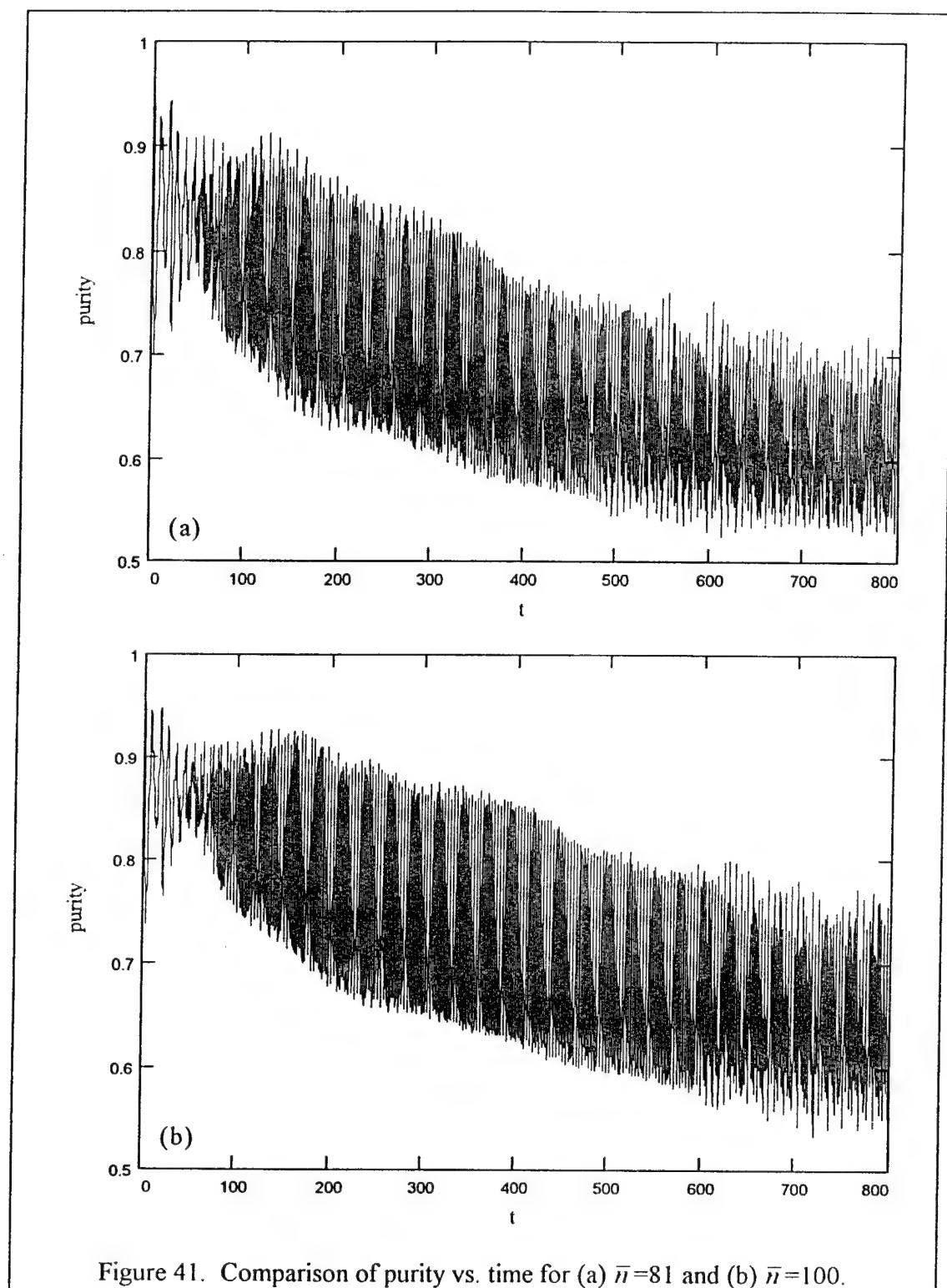
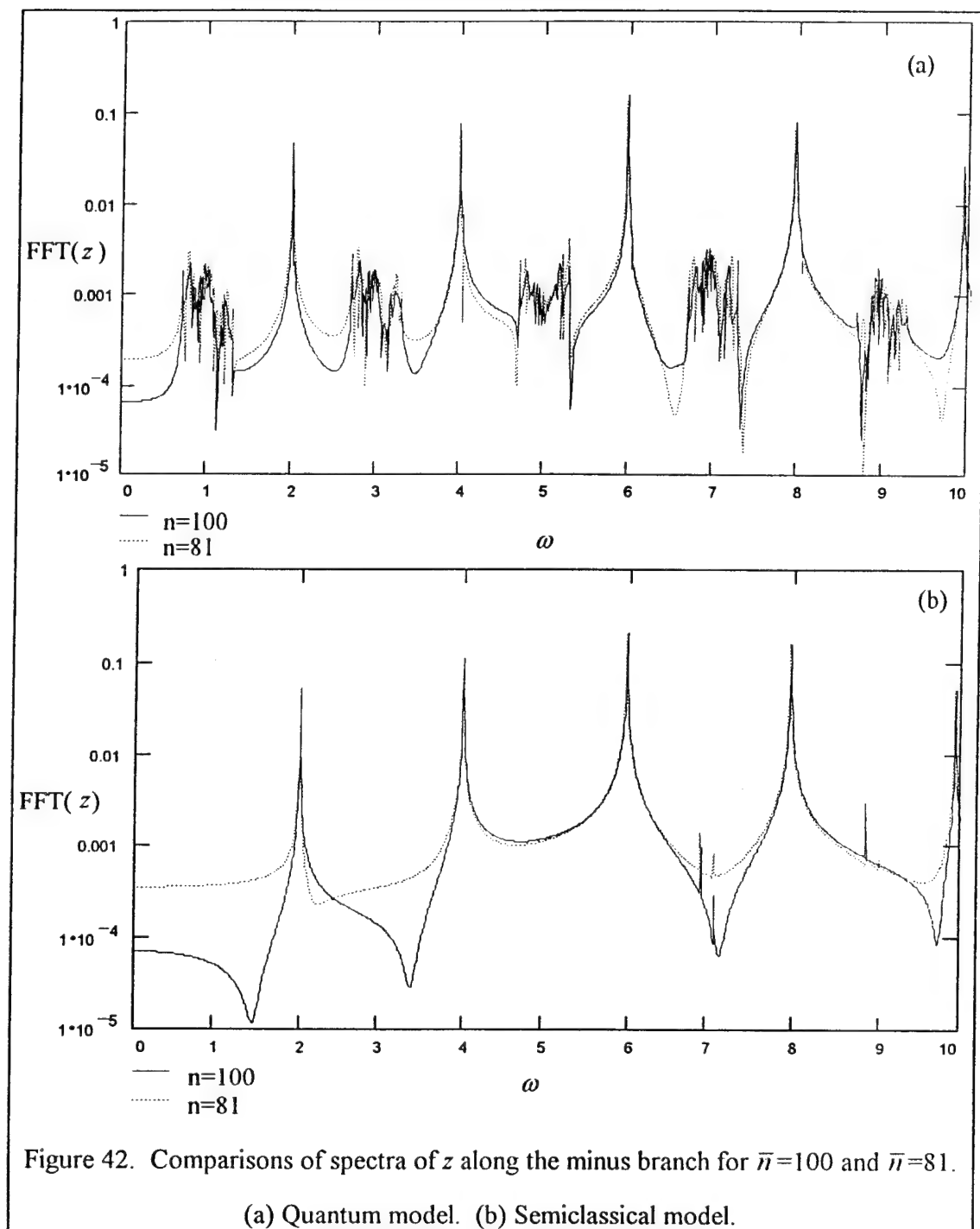
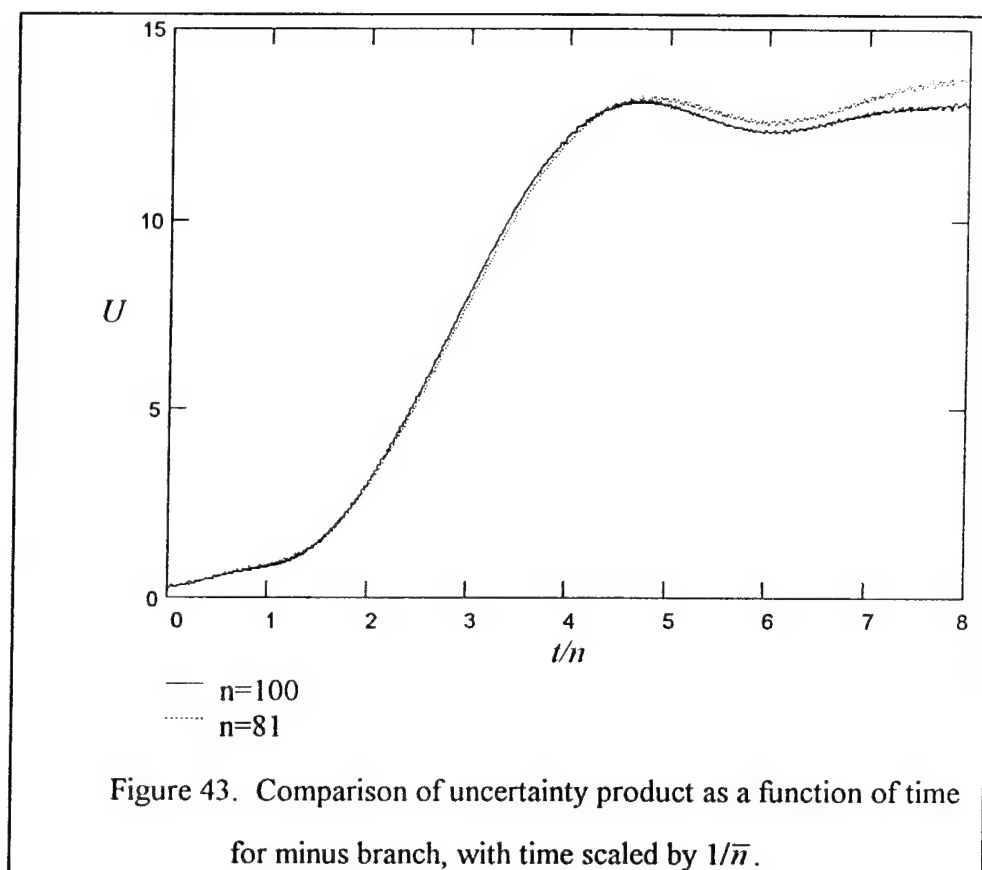


Figure 41. Comparison of purity vs. time for (a) $\bar{n}=81$ and (b) $\bar{n}=100$.





4.2 Higher values of Angular Momentum

The difficulty in establishing a correspondence between the onset of chaos in the semiclassical problem and a signature in the quantum problem seems to be related to the highly non-classical nature of a two level atom. The field is as classical as possible in a coherent state, which has the minimum possible uncertainty. However, the spin state can be made more classical by moving to higher values of angular momentum quantum number, j . Increasing j corresponds to an interaction between the field and a larger number of atoms, N , where $N=2j$. Graham and Höhnerbach showed the distribution of eigenvalues becomes typical of a chaotic system for larger values of j .^{25,27} Moving to higher values of j might make the quasiclassical states evolve more closely to the semiclassical states in the chaotic regime.

Numerically, calculating trajectories for higher values of j is much more challenging: The larger number of atomic states to calculate is compounded by the scaling given immediately following Eq. 2.8:

$$\begin{aligned} g &\rightarrow g/\sqrt{2j} & x &= \langle J_x \rangle / j \\ a_1 &\rightarrow a_1 \sqrt{2j} & y &= \langle J_y \rangle / j \\ a_2 &\rightarrow a_2 \sqrt{2j} & z &= \langle J_z \rangle / j \\ \bar{n} &\rightarrow \bar{n} 2j \end{aligned} \tag{4.10}$$

principally, that \bar{n} increases linearly with j . Increasing from $j=1/2$ to $j=3/2$ results in a roughly fivefold increase in computations at each time step. Furthermore, increasing \bar{n} results in higher frequencies which must be integrated using smaller time steps. For the first example given below, increasing from $j=1/2$ to $j=3/2$ resulted in an increase in computation time by a factor of forty. For this reason, this investigation was halted at $j=3/2$, even though higher values of j might prove to be interesting.

The Hamiltonian (1.1) for the higher j states becomes

$$H = \hbar\omega_0 J_z + \hbar\omega\alpha^\dagger a + \hbar g(J_+ + J_-)(a + a^\dagger), \quad (4.11)$$

where, for $j=3/2$, J_z , J_+ , and J_- are given by:

$$J_z = \hbar \begin{pmatrix} \frac{3}{2} & 0 & 0 & 0 \\ 0 & \frac{1}{2} & 0 & 0 \\ 0 & 0 & -\frac{1}{2} & 0 \\ 0 & 0 & 0 & -\frac{3}{2} \end{pmatrix} \quad (4.12a)$$

$$J_+ = \hbar \begin{pmatrix} 0 & \sqrt{3} & 0 & 0 \\ 0 & 0 & 2 & 0 \\ 0 & 0 & 0 & \sqrt{3} \\ 0 & 0 & 0 & 0 \end{pmatrix} \quad (4.12b)$$

$$J_- = \hbar \begin{pmatrix} 0 & 0 & 0 & 0 \\ \sqrt{3} & 0 & 0 & 0 \\ 0 & 2 & 0 & 0 \\ 0 & 0 & \sqrt{3} & 0 \end{pmatrix}. \quad (4.12c)$$

Obviously, the eigenstates of J_z are the basis states for describing the state of the three atoms. While the state of the $j=1/2$ system can be completely specified by two parameters, such as polar angles θ and ϕ (up to an unimportant overall phase), this is not the case for $j=3/2$. Instead, the equivalent initial condition is specified as an eigenstate of the operator $\vec{J} \cdot \hat{n}$, where \hat{n} is a unit vector specified by polar angles θ and ϕ . Using the standard angular momentum relationships $J_x = (J_+ + J_-)/2$ and $J_y = (J_+ - J_-)/2i$, (quite) a bit of algebra yields the starting points for the plus and minus branches

$$|\psi_+\rangle = \begin{pmatrix} e^{-2i\phi} \cos^3 \frac{\theta}{2} \\ \sqrt{3} e^{-i\phi} \sin \frac{\theta}{2} \cos^2 \frac{\theta}{2} \\ \sqrt{3} \sin^2 \frac{\theta}{2} \cos \frac{\theta}{2} \\ e^{i\phi} \sin^3 \frac{\theta}{2} \end{pmatrix}, \quad |\psi_-\rangle = \begin{pmatrix} e^{-2i\phi} \sin^3 \frac{\theta}{2} \\ -\sqrt{3} e^{-i\phi} \sin^2 \frac{\theta}{2} \cos \frac{\theta}{2} \\ \sqrt{3} \sin \frac{\theta}{2} \cos^2 \frac{\theta}{2} \\ -e^{i\phi} \cos^3 \frac{\theta}{2} \end{pmatrix} \quad (4.13)$$

These are the eigenstates of $\vec{J} \cdot \hat{n}$ with eigenvalue $\pm 3/2$, and become the special plus and minus branch starting points with $\theta = \theta_+$.

There are no tremendous differences in the evolution of the quasiclassical states for these values of j , although some interesting effects do begin to arise. Figure 44 shows the Bloch sphere evolution for the small ε case shown in Fig. 18, but for a shorter time ($t=126$). The parameters used in the $j=3/2$ model are $\varepsilon=0.141$, $\bar{n}=96$, and $g=0.02887$ ($0.05/\sqrt{3}$), which correspond to $\varepsilon=0.141$, $\bar{n}=32$, and $g=0.05$ for $j=1/2$. The only significant difference is that the deviations from the Autler-Townes model (which are just small amplitude Rabi oscillations) at the beginning of the trajectory are smaller. In this way the larger j model does match the semiclassical model more closely than the $j=1/2$ model. Since both of these sets of parameters scale to the same parameters for the semiclassical model, we expect the detuning will be the same for both values of j , which is indeed the case, based on the complex phasor method of finding the detuning.

As ε is increased, the differences between the $j=1/2$ and the $j=3/2$ models become somewhat more pronounced, and the $j=3/2$ model begins to show characteristics which are reminiscent of the semiclassical model. Let us examine these characteristics using a set of trajectories for the $j=3/2$ model which have parameters corresponding to those already seen, $\varepsilon=1$ and $\bar{n}=81$ or $\bar{n}=100$. For the $j=3/2$ model the corresponding values are $\varepsilon=1$ and $\bar{n}=243$ or $\bar{n}=300$. The differences between the $j=1/2$ and the $j=3/2$ models are first observable in Fig. 45, in which we can see the trajectories begin to spiral inward as the system loses purity more quickly than for the $j=1/2$ model (refer to Fig. 36 and Fig. 40), especially in regard to the plus branch. The difference between the plus and minus branches, which was almost indiscernible for $j=1/2$, is now quite distinct.

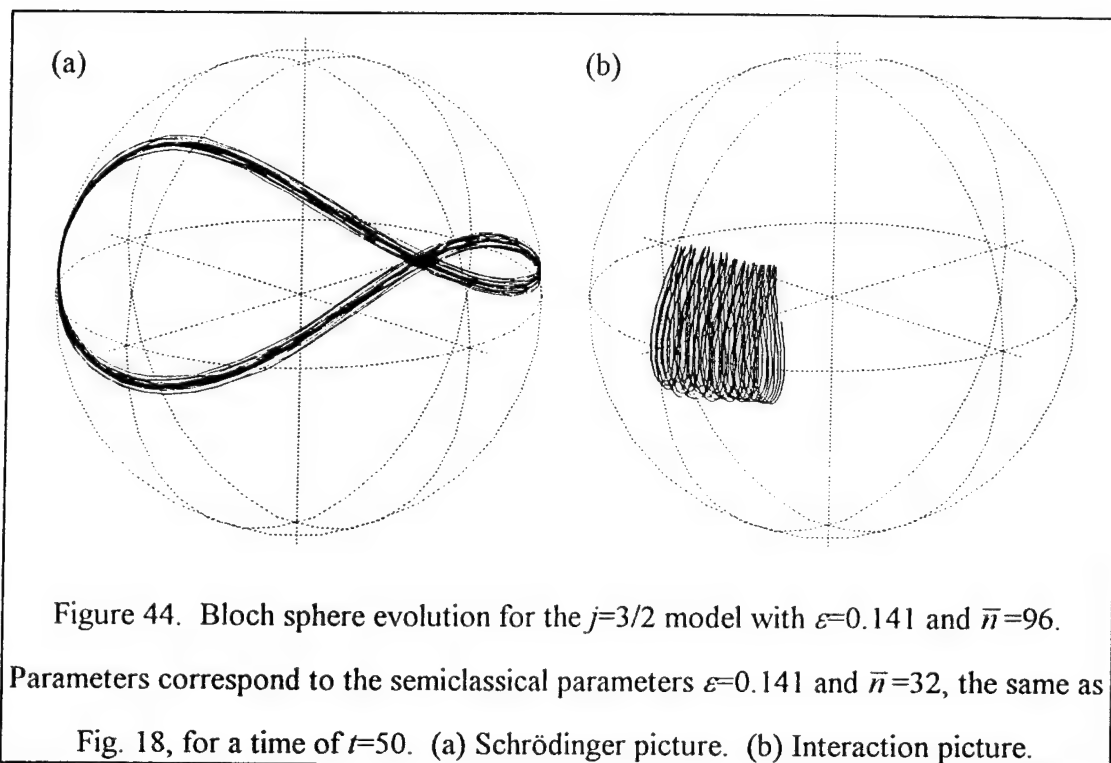
Another difference, although subtle, is demonstrated by Fig. 46. This figure shows the Bloch sphere from a different orientation, looking along the $+y$ axis. In three of the plots (a), (c), and (d), the trajectories are roughly symmetrical about $x=0$.

However, in (b) the trajectory is shifted slightly in the $+x$ direction. This particular plot corresponds to the chaotic semiclassical trajectory shown in Fig. 36d, which clearly shows a strong shift toward $+x$. Figure 47 contrasts $x(t)$ for the plus branch in the $j=3/2$ and $j=1/2$ models. Both trajectories correspond to $\varepsilon=1.0$ and $\bar{n}=81$ in the semiclassical model. In addition to the faster oscillations with $\omega=(2n+1)\omega'$, $x(t)$ for the $j=1/2$ model exhibits normal, slower Rabi oscillations under a Gaussian collapse envelope. These are similar to the oscillations observed in the Autler-Townes model given by Eq. 2.9 for $\gamma \neq 0$. Of course, in the Autler-Townes model the oscillations do not collapse. However, the oscillations for the $j=3/2$ model are different. Figure 47 shows the maximum value of x reached on each fast oscillation changes very little, while the minimum value of x increases considerably. This behavior results in the shift toward $+x$, not unlike the shift seen in the semiclassical model, and is perhaps a signature of the transition to chaos.

The purity also shows a possible signature of the semiclassical chaos, as shown in Fig. 48. While for $j=1/2$ the purity of the (non-chaotic) minus branch was lower than the purity for the (chaotic) plus branch, for $j=3/2$ the purity of the plus branch is lower. It is not unexpected that the purity along a particular branch will be slightly lower for smaller \bar{n} , as observed for the minus branch. However, the purity for the plus branch is substantially less for the smaller \bar{n} trajectory, again suggesting the lower purity could conceivably be a signature of semiclassical chaos.

Finally, the uncertainty product for the $j=3/2$ model yields results similar to those for the purity: The uncertainty product is significantly larger for the plus branch than for the minus branch, a reverse of the $j=1/2$ result. However, Fig. 49 shows the uncertainty product is almost independent of \bar{n} along a particular branch when plotted against the scaled time.

Clearly more work can be done in this area. The results here are intriguing because they suggest the possibility the signatures of chaos put forward by Grigolini, *et al.* may be applicable for higher values of j . However, these results do not support a definitive statement for either case. Additional work must be done by extending the integration time, examining the transition to chaos at other points in the parameter space, studying the eigenvalue structure, and, finally, repeating the process for higher values of j . Although the resources were not available to undertake these additional investigations in support of the present effort, the initial investigation has opened the possibility for further work in this field.



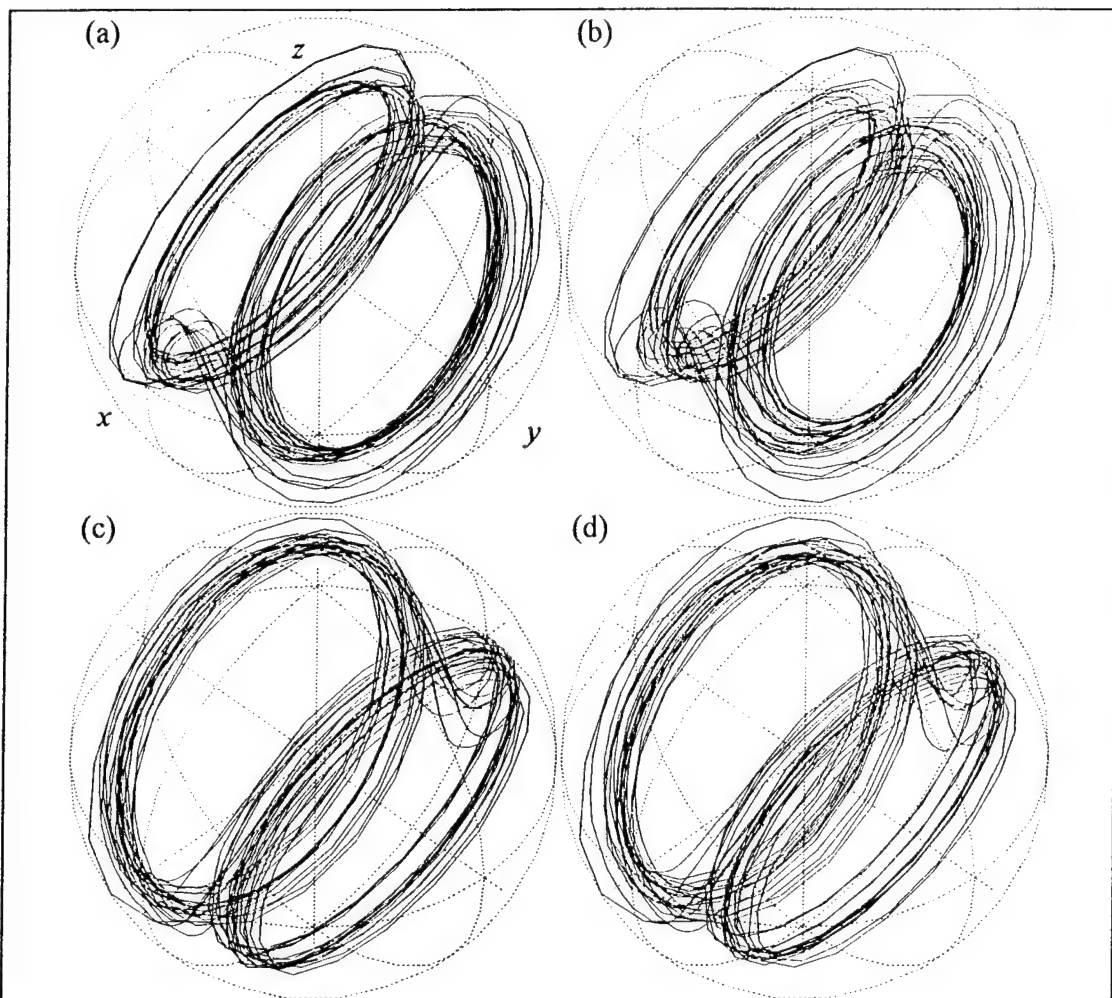


Figure 45. Bloch sphere evolution for $j=3/2$ model with $\varepsilon=1.0$ up to $t=50$. Parameters correspond to semiclassical model with $\varepsilon=1.0$ and $\bar{n}=100$ and $\bar{n}=81$. (a) Plus branch, $\bar{n}=300$, (b) plus branch, $\bar{n}=243$, (c) minus branch, $\bar{n}=300$, (d) minus branch, $\bar{n}=243$.

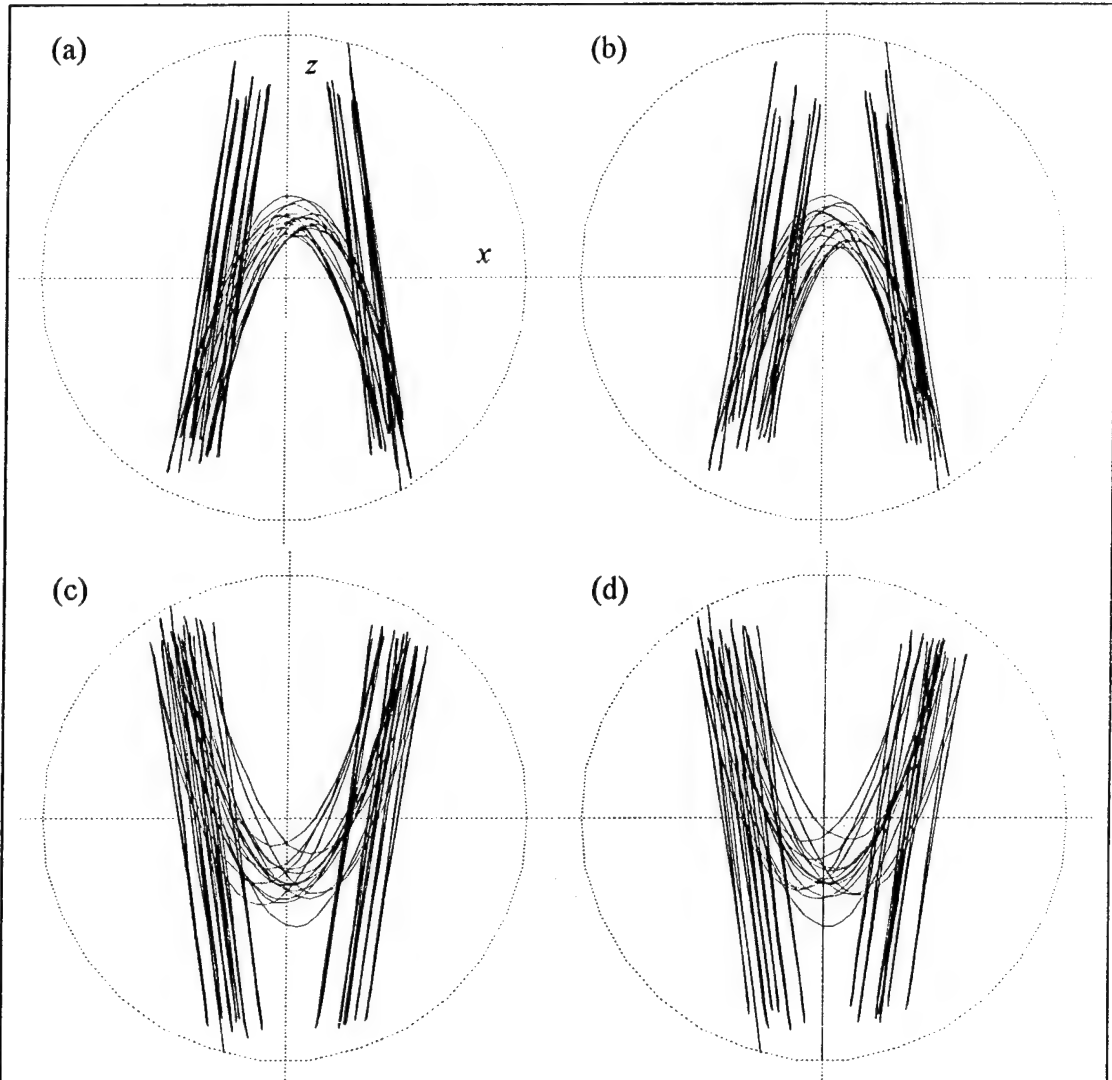


Figure 46. Bloch sphere evolution for $j=3/2$ model with $\varepsilon=1.0$. (a) Plus branch, $\bar{n}=300$, (b) plus branch, $\bar{n}=243$, (c) minus branch, $\bar{n}=300$, (d) minus branch, $\bar{n}=243$. This view shows the trajectory for (b) is skewed toward the $+x$ axis, while the others are symmetric about $x=0$.

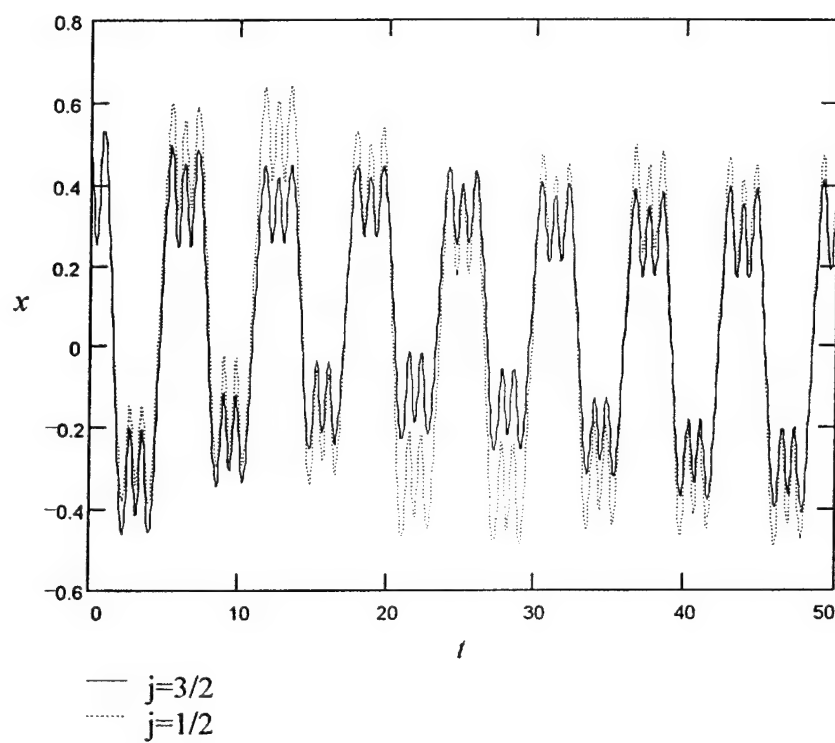


Figure 47. Comparison of $x(t)$ along the plus branch for $j=1/2$ and $j=3/2$ with parameters corresponding to semiclassical parameters $\varepsilon=1.0$, $\bar{n}=81$. The $j=1/2$ model exhibits normal Rabi oscillations, while the $j=3/2$ model is skewed toward $x=+1$.

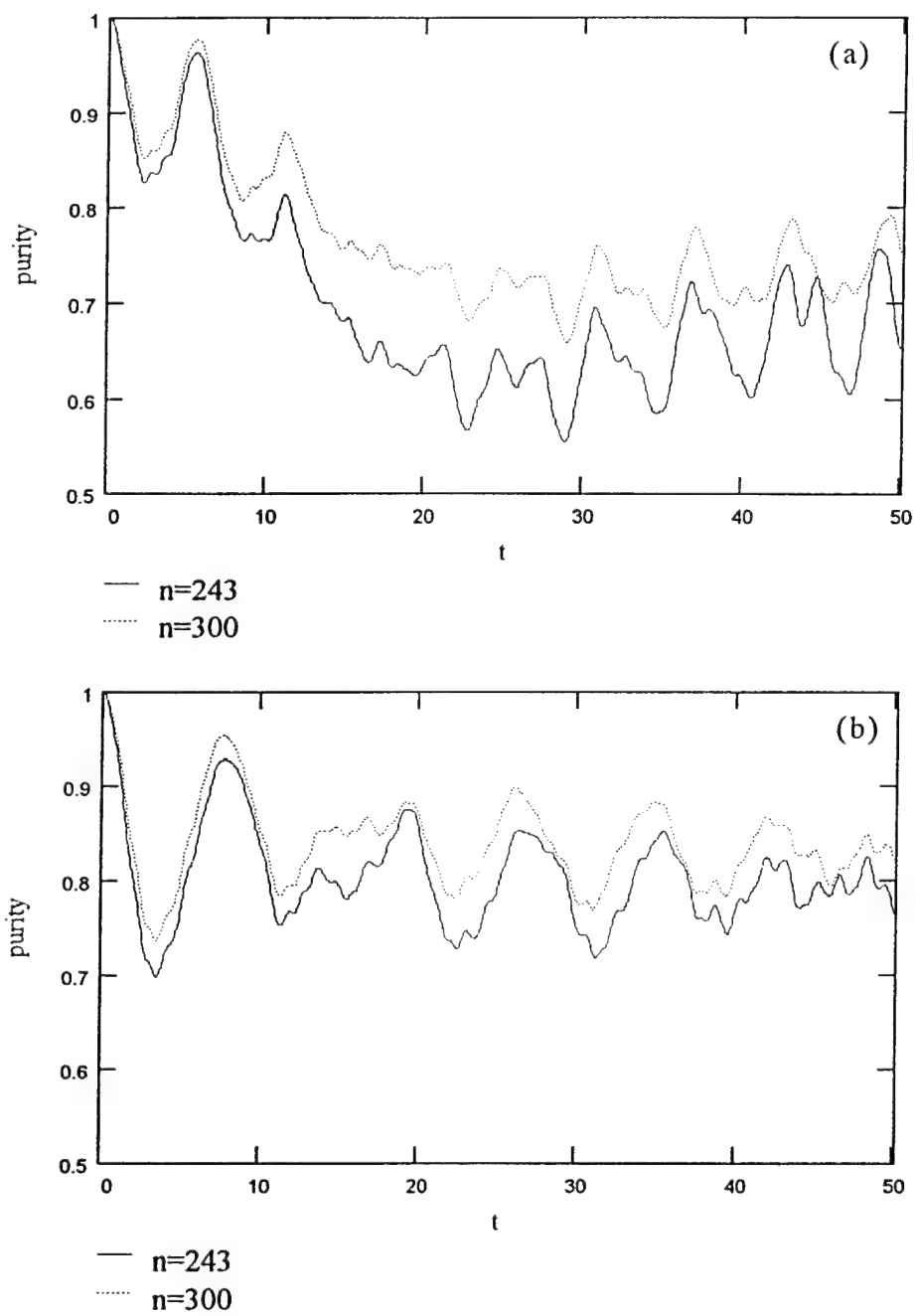
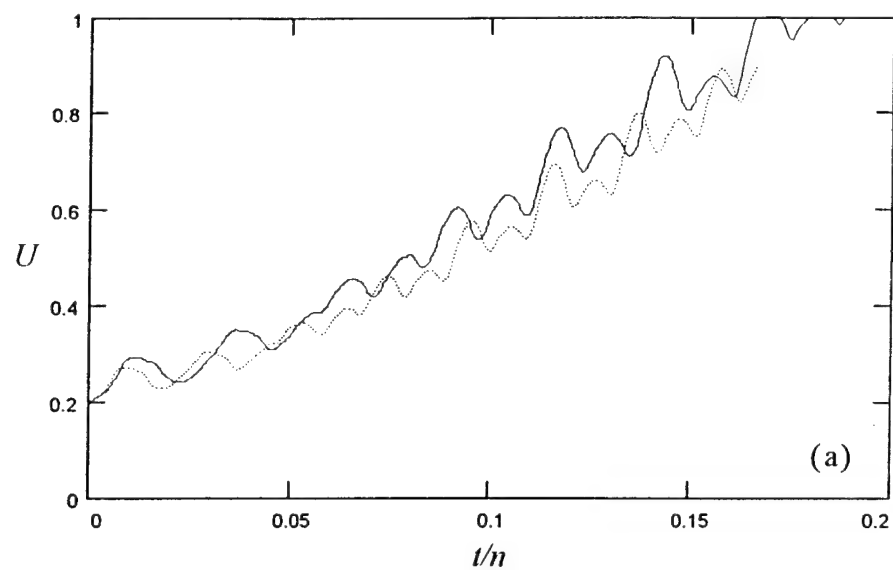
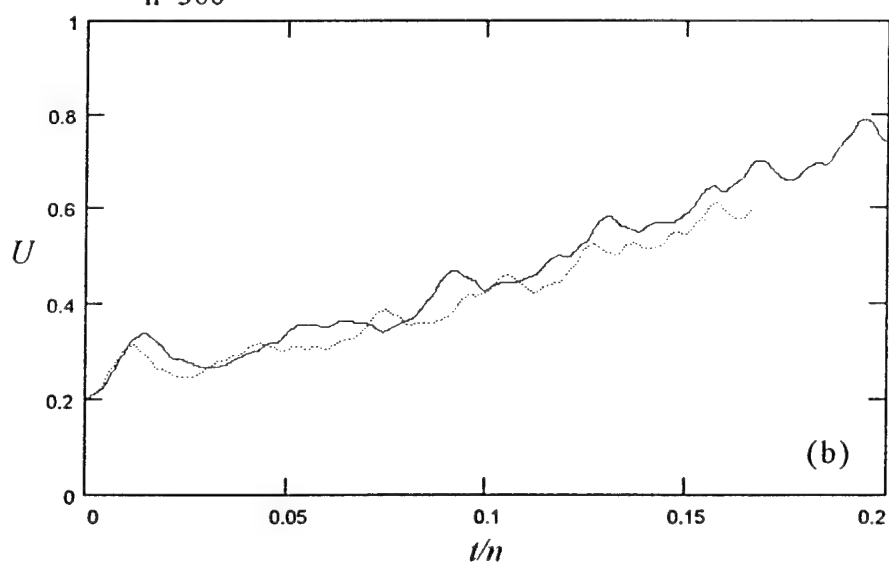


Figure 48. Purity vs. time along the plus and minus branches for $\varepsilon=1.0$ with $j=3/2$ (a) Plus branch, which semiclassically becomes chaotic. (b) Minus branch, which remains non-chaotic.



— $n=243$
 $n=300$



— $n=243$
 $n=300$

Figure 49. Comparison of uncertainty product along the plus and minus branches for the $j=3/2$ model, using the same parameters as in Fig. 48. (a) Plus branch (b) minus branch.

4.3 Conclusion

This work began with a review of the recent and not-so-recent efforts to investigate the behavior of the spin-boson system. Much work has been done using various approximations with the field treated both classically and quantum mechanically. With a semiclassical field the system had been shown to exhibit chaotic behavior in the realm of large numbers of atoms and an initially weak field. We then studied some of the tests for chaos and found another region of chaos: single atoms and intense fields. A special set of states which evolved quantum mechanically and semiclassically in close agreement were identified and studied. In spite of their similarity, one of these trajectories became unstable before the other. The reason was identified as a merging of harmonics in the spectra which resulted in the trajectories becoming unstable. Meanwhile, the quantum trajectories did not change their behavior. Thus we have seen clearly an example in which the semiclassical system undergoes a transition from regular to chaotic behavior, while the quantum system is qualitatively unchanged. This example strongly supports the contention that the changes observed in the purity (or entropy) and the quantum uncertainty are unrelated to the presence of chaos in the semiclassical model. By carefully comparing the semiclassical and quantum models using the quasiclassical states, we have found there is no essential difference in the quantum evolution between the manifestly non-chaotic RWA and the non-RWA models, so long as the quasiclassical approximation holds. The quasiclassical approximation holds until ε/\bar{n} (or $g/\sqrt{\bar{n}}$) becomes too large or \bar{n} becomes too small. Most importantly, the key in comparing the RWA to the non-RWA is in comparing similar states—whether comparing evolution along a particular branch or along a linear combination of branches.

Finally, an intriguing area has been opened, that of the dynamics of the system for larger values of angular momentum quantum number, j . The one example examined here, $j=3/2$, indicated the possibility that certain signatures of chaos may be present. The quasiclassical trajectories for this value of j were not more factorizable in the region near chaos. However, it did show share some characteristics with the semiclassical model, and, as in all fields of research, more work remains to be done.

BIBLIOGRAPHY

- ¹E. T. Jaynes and F. W. Cummings, Proc. IEEE **51**, 89 (1963).
- ²C. Cohen-Tannoudji, J. Dupont-Roc, and G. Grynberg, *Atom-Photon Interactions* (Wiley, New York, 1992).
- ³Herbert B. Shore and Leonard M. Sander Phys. Rev. B **7** 4537 (1973).
- ⁴D. Feinberg and J. Ranninger, Physica D **14**, 29 (1984).
- ⁵J. I. Cirac, A. S. Parkins, R. Blatt, and P. Zoller, Phys. Rev. Lett. **70**, 556 (1993).
- ⁶C. A. Blockley, D. F. Walls, and H. Risken, Europhys. Lett. **17**, 509 (1992).
- ⁷Dmitrii E. Makarov, Phys. Rev. E **48**, R4164 (1993) and references cited therein.
- ⁸P. I. Belobrov, G. M. Zaslavskii, and G. Kh. Tartakovskii, Sov. Phys. JETP **44**, 945 (1976).
- ⁹S. H. Autler and C. H. Townes, Phys. Rev. **100**, 703 (1955).
- ¹⁰J. Gea-Banacloche, Phys. Rev. A **44**, 5913 (1991).
- ¹¹J. Gea-Banacloche, Opt. Commun. **88**, 531 (1992).
- ¹²J. Gea-Banacloche, Phys. Rev. A **46** 7307 (1992).
- ¹³Jon H. Shirley, Phys. Rev **138**, B979 (1965).
- ¹⁴M. Tavis and F. W. Cummings, Phys. Rev. **170**, 379 (1968).
- ¹⁵P. W. Milonni, J. R. Ackerhalt, and H. W. Galbraith, Phys. Rev. Lett. **50**, 966 (1983).
- ¹⁶Ronald F. Fox and John Eidson, Phys. Rev. A **34**, 482 (1986).
- ¹⁷David K. Campbell, Los Alamos Science, *Special Issue* (1987).
- ¹⁸Adam Kujawski and Martin Munz, Phys. Rev. A **35**, 5274 (1987).
- ¹⁹Luca Bonci, Roberto Roncaglia, Bruce J. West, and Paolo Grigolini, Phys. Rev. A. **45**, 8490 (1992).
- ²⁰Luca Bonci and Paolo Grigolini, Phys. Rev. A **46**, 4445 (1992).

- ²¹ Roberto Roncaglia, Luca Bonci, Paolo Grigolini, and Bruce J. West, *J. Stat. Phys.* **68**, 321 (1992).
- ²² L. E. Reichl, *The Transition to Chaos in Conservative Classical Systems: Quantum Manifestations*, Chapter 7, Springer-Verlag (New York, 1992).
- ²³ Marek Kuś, *Phys. Rev. Lett.* **54**, 1343 (1985).
- ²⁴ L. C. Percival, *J. Phys. B* **6**, L229 (1973).
- ²⁵ R. Graham and M. Höhnerbach, *Phys. Rev. Lett.* **57**, 1378 (1986).
- ²⁶ R. Graham and M. Höhnerbach, *Z. Phys. B* **57**, 233 (1984).
- ²⁷ R. Graham and M. Höhnerbach, in *Quantum Measurement and Chaos*, ed. E. R. Pike and S. Sarkar, Plenum (New York, 1987).
- ²⁸ M. B. Cibils, Y. Cuche, W. F. Wreszinski, J.-P. Amiet and H. Beck, *J. Phys. A* **23**, 545 (1990).
- ²⁹ M. B. Cibils, Y. Cuche, V. Marvulle, W. F. Wreszinski, J.-P. Amiet and H. Beck, *J. Phys. A* **24**, 1661 (1991).
- ³⁰ M. B. Cibils, Y. Cuche, P. Leboeuf, and W. F. Wreszinski, *Phys. Rev. A* **46**, 4560 (1992).
- ³¹ H. Chen, Y.-M. Zhang, and X. Wu, *Phys. Rev. B* **40**, 11326 (1989).
- ³² Joachim Stolze and Lothar Müller, *Phys. Rev. B* **42**, 6704 (1990).
- ³³ Lothar Müller, Joachim Stolze, Hajo Leschke, and Peter Nagel, *Phys. Rev. A* **44**, 1022 (1991).
- ³⁴ W.-H. Steeb, C. M. Villet, A. Kunick, *Phys. Rev. A* **32**, 1232 (1985).
- ³⁵ Manfred Schmutz, *J. Phys. A* **19**, 3565 (1986).
- ³⁶ F. Großmann and P. Hänggi, *Europhys. Lett.* **18**, 571 (1992).
- ³⁷ Giancarlo Benettin, Luigi Galgani, Jean-Marie Strelcyn, *Phys. Rev. A* **14**, 2338 (1976).
- ³⁸ G. A. Finney and J. Gea-Banacloche, *Phys. Rev. A* **50**, 2040 (1994).

- ³⁹ Murray Sargent III, Marlan O. Scully, Willis E. Lamb, Jr., *Laser Physics*, Ch. 7, (Addison-Wesley, Reading, MA, 1974).
- ⁴⁰ J. H. Eberly, N. B. Narozhny, and J. J. Sánchez-Mondragón, *Phys. Rev. Lett.* **44**, 1323 (1980).
- ⁴¹ N. B. Narozhny, J. J. Sánchez-Mondragón, and J. H. Eberly, *Phys. Rev. A* **23**, 236 (1981).
- ⁴² Julio Gea-Banacloche, *Phys. Rev. Lett.* **65**, 3385 (1990).
- ⁴³ J. Eiselt and H. Risken, *Opt. Commun.* **72**, 351 (1989).
- ⁴⁴ J. Eiselt and H. Risken, *Phys. Rev. A* **43**, 346 (1991).
- ⁴⁵ C. W. Woods and J. Gea-Banacloche, *J. Mod. Opt.* **40**, 2361 (1993).
- ⁴⁶ K. Zaheer and M. S. Zubairy, *Phys. Rev. A* **37**, 1628 (1988).
- ⁴⁷ J. J. Sakurai, *Modern Quantum Mechanics*, Chapter 5, Addison-Wesley (New York, 1994).
- ⁴⁸ F. A. M. de Oliveira, M. S. Kim, P. L. Knight, and V. Buzek, *Phys. Rev. A* **41**, 2645 (1990).
- ⁴⁹ S. J. D. Phoenix and P. L. Knight, *Ann. Phys.* **186**, 381 (1988).
- ⁵⁰ L. Bonci, R. Roncaglia, B. J. West, and P. Grigolini, *Phys. Rev. Lett.* **67**, 2593 (1991).

APPENDIX A

Matrices used in Perturbation Calculation

In Sec. 2.3 a calculation to find the frequencies which appear in the semiclassical model was presented. However, the matrices were sufficiently large to be impractical for inclusion in the main text. Therefore they have been relegated to this appendix. Equation 2.20 is a sum of matrix equations, but because some of the matrix elements contain complex exponentials, the terms in the sum are not independent. Therefore, the summation needs to be rewritten into a single matrix equation which can be numerically and perturbatively solved. The basis vectors can be broken into five parts corresponding to $\delta\alpha_1$, $\delta\alpha_2$, δx , δy , and δz . Each of these five parts has an infinite number of elements corresponding to the coefficients of the complex exponential $e^{i(\nu+n\mu)t}$. An arbitrary vector \mathbf{x} may be written as shown to the right. Furthermore, suppose we designate the subvectors of \mathbf{x} corresponding to the different expectation values as \mathbf{x}_{a_1} , \mathbf{x}_x , \mathbf{x}_z , etc. Likewise, we can designate submatrices of the matrices \mathbf{A} and \mathbf{B} as $\mathbf{A}_{x,x}$, $\mathbf{B}_{a_1,z}$, etc., using the standard *row, column* index convention. Now we can determine specifically the various non-zero parts of \mathbf{A} . The simplest parts are those identified

$$\mathbf{x} = \begin{pmatrix} \vdots \\ \delta\alpha_{1,-n} \\ \vdots \\ \delta\alpha_{1,-1} \\ \delta\alpha_{1,0} \\ \delta\alpha_{1,1} \\ \vdots \\ \delta\alpha_{1,n} \\ \hline \vdots \\ \delta\alpha_{2,-n} \\ \vdots \\ \delta\alpha_{2,-1} \\ \delta\alpha_{2,0} \\ \delta\alpha_{2,1} \\ \vdots \\ \delta\alpha_{2,n} \\ \hline \vdots \\ \delta x_{-n} \\ \vdots \\ \delta x_{-1} \\ \delta x_0 \\ \delta x_1 \\ \vdots \\ \delta x_n \\ \hline \vdots \\ \delta y_{-n} \\ \vdots \\ \delta y_{-1} \\ \delta y_0 \\ \delta y_1 \\ \vdots \\ \delta y_n \\ \hline \vdots \\ \delta z_{-n} \\ \vdots \\ \delta z_{-1} \\ \delta z_0 \\ \delta z_1 \\ \vdots \\ \delta z_n \\ \vdots \end{pmatrix} \quad (\text{A.1})$$

by ± 1 in Eq. 2.20, $\mathbf{A}_{a_1,a_2} = -\mathbf{A}_{a_2,a_1} = -\mathbf{A}_{x,a_1} = \mathbf{A}_{a_1,x}$. These submatrices are merely the identity matrix, with ± 1 along the main diagonal of the submatrix. The next simplest to determine are the submatrices along the main diagonal of \mathbf{A} . These all have the form

$$\mathbf{A}_{a_1,a_1} = \begin{pmatrix} \ddots & 0 & 0 & 0 & 0 & 0 & 0 & 0 & 0 \\ 0 & n\mu & 0 & 0 & 0 & 0 & 0 & 0 & 0 \\ 0 & 0 & \ddots & 0 & 0 & 0 & 0 & 0 & 0 \\ 0 & 0 & 0 & \mu & 0 & 0 & 0 & 0 & 0 \\ 0 & 0 & 0 & 0 & 0 & 0 & 0 & 0 & 0 \\ 0 & 0 & 0 & 0 & 0 & -\mu & 0 & 0 & 0 \\ 0 & 0 & 0 & 0 & 0 & 0 & \ddots & 0 & 0 \\ 0 & 0 & 0 & 0 & 0 & 0 & 0 & -n\mu & 0 \\ 0 & 0 & 0 & 0 & 0 & 0 & 0 & 0 & \ddots \end{pmatrix} \quad (\text{A.2})$$

$$= \mathbf{A}_{a_1,a_{11}} = \mathbf{A}_{x,x} = \mathbf{A}_{y,y} = \mathbf{A}_{z,z}$$

Now comes the cosine expansion. Because of the two exponentials forming the cosine function, the index of each element multiplied by this term will be raised or lowered by 1, thus

$$\mathbf{A}_{y,z} = \begin{pmatrix} 0 & \ddots & 0 & 0 & 0 & 0 & 0 & 0 & 0 \\ \ddots & 0 & -4\varepsilon & 0 & 0 & 0 & 0 & 0 & 0 \\ 0 & -4\varepsilon & 0 & -4\varepsilon & 0 & 0 & 0 & 0 & 0 \\ 0 & 0 & -4\varepsilon & 0 & -4\varepsilon & 0 & 0 & 0 & 0 \\ 0 & 0 & 0 & -4\varepsilon & 0 & -4\varepsilon & 0 & 0 & 0 \\ 0 & 0 & 0 & 0 & -4\varepsilon & 0 & -4\varepsilon & 0 & 0 \\ 0 & 0 & 0 & 0 & 0 & -4\varepsilon & 0 & -4\varepsilon & 0 \\ 0 & 0 & 0 & 0 & 0 & 0 & -4\varepsilon & 0 & \ddots \\ 0 & 0 & 0 & 0 & 0 & 0 & 0 & \ddots & 0 \end{pmatrix} \quad (\text{A.3})$$

$$= -\mathbf{A}_{z,y}$$

The first part of the matrix \mathbf{B} is also straightforward. The submatrix $\mathbf{B}_{a_2,x}$ is the identity matrix multiplied by the constant $-\beta$. To obtain the next part we will return to the equation from which the matrices are extracted, considering only the y portion,

$$(\mathbf{B}\mathbf{x})_y = -z^{AT}(t) \sum_{n=-\infty}^{\infty} \delta a_{1,n} e^{i(v+n\mu)t} \quad (\text{A.4})$$

Now expanding z^{AT} as a sum of complex exponentials

$$\begin{aligned} (\mathbf{B}\mathbf{x})_y &= - \sum_{n,m=-\infty}^{\infty} z_m^{AT} \delta a_{1,n} e^{i[v+(n+m)\mu]t} \\ &= - \sum_{n,m=-\infty}^{\infty} z_{m-n}^{AT} \delta a_{1,n} e^{i[v+m\mu]t} \end{aligned} \quad (\text{A.5})$$

From this expression it is evident that the matrix element $\mathbf{B}_{y,m,a_1,n} = -z_{m-n}^{AT}$, or

$$\mathbf{B}_{a_1,y} = - \begin{pmatrix} \ddots & \ddots & & & \ddots & \ddots \\ \ddots & z_0 & z_{-1} & & & z_{n-m} \\ & z_1 & z_0 & z_{-1} & \ddots & \ddots \\ & & z_1 & z_0 & z_{-1} & \\ \ddots & & \ddots & z_1 & z_0 & z_{-1} \\ & z_{m-n} & & & z_1 & z_0 \\ \ddots & & \ddots & & & \ddots & \ddots \end{pmatrix} \quad (\text{A.6})$$

Likewise, $\mathbf{B}_{a_1,z}$ will have the same form, except with y^{AT} in place of z .

In practice, the submatrices were each truncated at 31 rows to calculate the unperturbed eigenvectors, for a total of 155 elements in each eigenvector and 24,025 elements in each matrix.

APPENDIX B

A Note on Numerical Methods

A large portion of this research has been done numerically, and so a note on the methods employed is in order. Several types of calculations were accomplished numerically: algebraic calculation, integration, and eigensystem solution. Most of the computations were performed using a personal computer (40 MHz 80386SX with 80387 coprocessor and 8 MB memory), although some were performed on the University of Arkansas mainframe (Sun SparcCenter 2000 with eight 40 MHz microprocessors and 256 MB memory).

Algebraic calculations were generally accomplished using Mathcad. This includes evaluations of the Floquet exponent, λ_q , the A 's and B 's, etc. Analysis of the numerical integrations (plots of time series, FFTs, Poincaré sections, etc.) was also done in Mathcad. Most plots in the main text are Mathcad output. In addition, some of the symbolic manipulation capabilities of Mathcad were used during analytical work.

The numerical integration was accomplished using a fourth-order Runge-Kutta routine with adaptive step size control. The algorithm and much of the code was taken from the book *Numerical Recipes in Pascal* (Press, Flannery, Teukolsky, and Vetterling, Cambridge University Press, 1989). The adaptive step size control is implemented by taking a single step in time, then repeating the calculation in two steps, each using one half the original step size. If the difference in the result is sufficiently small, then the result is saved and a new step size is computed based on the difference. If the difference is too large, a new step size is computed and the process repeated. The accuracy parameter (eps in the reference given above) was set at 10^{-8} .

to achieve a balance of execution speed and accuracy. The program on the PC was implemented using Turbo Pascal for Windows. Semiclassical calculations required about 2 minutes for $t=200$ in the examples used in Chapter 4. Quantum $j=1/2$ calculations required about 2 hours for the corresponding trajectories. All the numerical integration for the $j=3/2$ model was done on the mainframe. The same integration routine was used. Using the parameters of the first example in Sect. 4.2, for $t=4\pi$, the $j=1/2$ case required about 2 minutes of real time to complete, while the $j=3/2$ case required about 80 minutes of real-time. CPU time was approximately one half of those amounts. The later examples for the $j=3/2$ case required 15-16 hours of CPU time to integrate up to $t=50$. The normalization of the wavefunction and the total energy were computed to check the accuracy of the integration, and both were typically conserved to 1 part in 10^6 – 10^7 .

The eigensystems were solved using a combination of programming and Mathcad. A simple program from *Numerical Recipes in Pascal* was employed to calculate the eigenvalues of (I.1), which is tridiagonal if separated into its even and odd parity parts. All other eigenvalues and all eigenvectors were computed using the built-in eigenvalue and eigenvector functions of Mathcad. The calculation of eigenvalues typically required a few minutes to complete on the PC, while the calculation of a full set of eigenvectors could take several hours.